Improvement of Supersonic Aerodynamic Performance using Shock Wave Interactions

Dissertation

Submitted in
Partial Fulfillment for the Degree of
Doctor of Engineering

Department of Aerospace Engineering
Nagoya University

Jae-Hyung KIM

March 2011

Dissertation Committee

Sasoh Akihiro
Professor

Yoshiaki Nakamura
Professor

Yasuhiko Sakai
Professor

Takeharu Sakai
Associate Professor

Abstract

In the aspect of the supersonic aerodynamic performance, shock wave formation leads inevitably to serious problems preventing the development of high-performance supersonic vehicle. A representative problem is sonic boom which is an impulsive noise induced by a supersonic aircraft. Wave drag force induced by shock wave is another serious problem against improvement of the aerodynamic performance.

This study investigates the sonic boom mitigation by interaction with turbulent flowfield. The pressure modulation of a weak shock wave induced by an Nd:YAG laser pulse when passing across a turbulent slit jet is experimentally investigated. With the slit jet the peak overpressure becomes smaller by an average of 12 %, with a standard deviation being 27 %. Clear relationships are obtained between the overpressure history and the experimentally-observed shock front deformation, which is visualized as differential schlieren images. The peak overpressure is increased when the originally spherical blast wave front is locally flattened, whereas it is decreased when a hump in the shock wave front is formed.

This study also considers further technology to reduce a wave drag force. Wave drag reduction over a 20-mm-dia., flat-nosed cylinder in a Mach 1.94 flow is done by depositing laser pulse energies at repetition frequencies up to 80 kHz and average input power of 400 W at a maximum. A time-averaged drag reduction of up to 21 % and power gain, which is the amount of a saved propulsion power divided by an input laser power, of the order of 10 are obtained. Interactions between the laser-induced, low-density region and the bow shock wave are diagnosed with framing Schlieren visualization and stagnation pressure measurement. Baroclinic interaction between the laser-induced low density region and the bow shock wave over the cylinder yields a vortex ring which generates counter flow along the center axis. The static pressure in the shock layer is decreased while the vortex ring stays there. With increasing the energy deposition frequency, the number of vortex rings staying in the shock layer increases so that the thickness of the bow shock wave on the center axis is increased; the static pressure is decreased resulting in the drag deduction. Although such pulse-to-pulse interactions are significant, in particular above 10 kHz, for a constant pulse energy the time-averaged drag reduction almost linearly increases with the repetition frequency. The power gain depends only

on the pulse energy and has a maximum at around 8 mJ. Relationship between the time-averaged drag reduction performance and unsteady flows induced by the energy depositions in the shock layer are discussed.

Behavior of vortex rings, which are repetitively generated by depositing laser pulse energies ahead of a bow shock wave with a constant circulation, is explored. Interaction patterns become different with laser frequency. With increasing the pulse repetition frequency mutual interactions among the vortex rings become stronger; alternate pitching motions at f=10 to 20 kHz and 'slip-through' motions at f=30 kHz appear. Beyond that, a quasi-steady-state acting spike which decreases the stagnation pressure is built up.

Finally, drag reduction performance over truncated cone model is estimated. Truncated cone model is proposed to trade-off between the magnitude of drag reduction and power gain. In the experiments, nose-to-base diameter ratio (d_f/d) is varied from 0.0 to 1.0 with flat-faced truncated cone model. From the visualization results and stagnation pressure histories, it is concluded that effective residence time of the vortices plays an important role in drag reduction performance of truncated cone model. In order to improve the drag reduction performance, concave-faced truncated cone models are also examined and more effective drag reduction performance is obtained.

Contents

List of Table

List of Figures

Chapter 1. Introduction

1-1. Issues Related to Shock Waves in Supersonic Aircraft

Even before the development of the Concorde as the first supersonic civil transportation, several problems on supersonic aerodynamic performance exist. In particular, we essentially encounter with the shock wave in front and rear of a supersonic aircraft. The shock wave generation causes two serious problems, sonic boom and large drag force. From an environmental problem, it is needed to minimize the sonic boom generated when the aircraft flies at supersonic speeds. In a view point of saving the propulsion energy, the lift-to-drag ratio in supersonic aircraft should be improved. In order to solve these problems for the development of a next generation supersonic transportation(SST) with excellent economic and environmental characteristics, advanced technologies are necessary.

The annoyance of a sonic boom can be avoided until the aircraft is at high altitude over water before reaching supersonic speeds. However, it precludes supersonic flight over populated areas. Therefore, it is essentially required much efforts to reduce the sonic boom intensity and to investigate the exposure effects on human, animal and structures. Another issue is the lift to drag ratio (*L/D* ratio) of a supersonic aircraft. The ratio of lift to drag indicates directly an aerodynamic efficiency. Under cruise conditions, a lift force and a drag force are equal to an aircraft weight and a thrust force, respectively. At supersonic speeds, it is well known that the aircraft has a less efficiency than at subsonic speeds. For this reason, considerable research has been performed to improve the *L/D* ratio of supersonic aircraft. For instance, at about Mach 2, the *L/D* ratio is cut worse than the half (e.g., the Concorde vehicle managed a ratio of 7.14, whereas the subsonic Boeing 747 has an *L/D* ratio of 17). [Loftin, L. K. Jr., (2006)] Because an aircraft must provide enough propulsion to overcome its own drag, a reduction of its *L/D* ratio at supersonic speeds requires additional thrust to maintain its airspeed and altitude. Therefore, to improve the *L/D* ratio, wave drag reduction using advanced technique is required at supersonic flight speed in particular.

In this thesis, two issues related to shock wave, sonic boom and wave drag reduction, will be treated to improve the feasibility of the next generation supersonic transportation.

1-2. Sonic boom from SST

In recent years, the impulse noise arising from an aircraft has been receiving much attention because of its annoyance and harmful effects on human health.[Rice, C. G. (1996); Plotkin, K. J., et al. (2008); Salikuddin, M., et al., (1988); Howe, D. C., et al., (2006)] For subsonic flight speeds the pressure disturbances are rather smooth variations. They decrease at roughly the inverse square of the distance from the aircraft. At supersonic flight speeds, the pressure disturbances are concentrated in waves. The pressure disturbances in these waves decrease roughly with the reciprocal of the distance from the aircraft. Because of this lower intensity decrease with distance as comparing with subsonic aircraft, the pressure disturbances made by supersonic aircraft are experienced at longer distances from the aircraft. Furthermore, the sharp variations in pressure make the disturbances audible as the sonic boom. However, it is not sufficient to fully understand the mechanism of the origin and propagation of noise in order that prediction methods and control strategies are developed.

The impulse noise from supersonic aircraft is called sonic boom. Considerable research efforts have been and are being spent to understand the effects of exposure to sonic booms. [Onyeonwu, R. O. (1975); Salikuddin, M., et al. (1988); Haglund, G. T., et al. (1972)] Research into the effects of sonic boom upon human beings was greatly stimulated by the prospect of the introduction of civil supersonic transport aircraft operations. Problems associated with sonic boom had largely been discussed toward development of the Concorde at that time being a representative of the first generation SST(Supersonic Transport). It is known that the magnitude of sonic boom peak overpressure dependent on Mach number, altitude, length and shape of the flight body. The magnitude is most affected by the weight of the flight body and decreases as the length of the flight body becomes longer. [May, D. D., et al (1971); Rice, C. G., et al. (1996)]

Much effort has been devoted to understand sonic boom phenomenon and evaluate its intensity. And a great advance has been made from both theoretical and experimental aspects. [Leaterwood, J. D. et al. (1994); Rylander, R. (1972); Zepler, E. E., et al. (1965)] However,

techniques for reduction of sonic boom are yet to be established and thus Concorde can not fly overland at supersonic speeds. Recently, much attention is being concentrated on the development of the next generation SST, and problem of the sonic boom reduction has been re-visited. [Ivanteeva, L. G., et al. (2002); Lipkens, B. (2002); Lee, Y. S., et al. (1995)]

1-2-1 Pressure profile induced by supersonic body

At supersonic flight speeds, compression waves generated by an aircraft coalesce into an oblique wave like a Mach wave which approximately makes an angle arccosec *M* to the direction of the flight, where *M* is the aircraft Mach number. Waves from forward facing elements of the aircraft-fuselage nose, wing leading edge, cockpit canopy, etc. – are usually regions of compression with positive overpressure. The waves from rearward facing elements of the aircraft-rear fuselage, wing trailing edge, etc.- are usually regions of expansion with negative overpressure.

Figure 1-1 shows the general generation and propagation of sonic boom. From an aircraft a complex waveform pattern is radiated. Owing to the non-linearity of compressible fluid dynamics, the propagation pattern is not straightforward. The decay and spreading of the sonic boom signature is non-linearly changed with increasing distance from the supersonic aircraft. Compression waves steepen to form a shock wave in the signature, and expansion waves smears and become less steep and linearly decaying segments. Intermediate pressure perturbations in the signature, which are produced by particular features of the body shape such as a change in surface curvature, not only decrease in amplitude but also migrate within the wave. They overtake and merge with other perturbations before they eventually coalesce to form simpler patterns, and the signature of sonic boom can be sensed on the ground as an N-shape wave when the sonic boom propagates through the homogeneous atmosphere.

A typical N-shape wave is schematically shown in Fig. 1-2. In N-shape wave form, generally the important parameters determining the pressure wave form of sonic boom are peak overpressure, duration time, and rise time. The peak overpressure is usually used to assess the

allowance of sonic boom, but it cannot be enough to find psychological effects on human beings. [McCurdy, D. A. (1994); Rice, C. G., et al. (1968)]

1-2-2 Effect of turbulent flow on sonic boom

An environment of sonic boom propagation commonly does not have homogeneous atmosphere conditions. Eventually, atmospheric conditions will cause considerable variations in waveform shape from that of the typical N-shape wave. Up to date many efforts have been tried to investigate the distortion of sonic boom interacted with turbulent flow field. [Crow, S. C. (1969); Plotkin, K. J., et al. (1972); Maglieri, D. J., et al. (1969); Maglieri, D. J. (1967); Chernyshev, S. L., et al., (2008); Castner, R. S., (2008)] From these results, it is well known that atmospheric condition with turbulence can cause a substantial distortion of the waveform, and reported the variations of peak overpressure and rise time of sonic boom signatures.

Figure 1-3 illustrate the classification often used to specify the sonic boom distortion caused by the interaction with turbulent flow. Gionfriddo was devised a scheme of 7 categories. Reported here is Gionfriddo's scheme. Sonic boom that are called normal (a) show little deviation in their shape from the classical N wave signature. These waves usually occur only when the atmosphere is quiet. Peaked or spiked booms (b) exhibit a distinctive, narrow spike, almost always at the tail shock as well as at the bow shock. Rouned booms (c) are those for which the pressure rises more slowly to its peak, that is, the bow and tail shocks are smooth, not abrupt. U-shaped waveform(d) implies that the sonic boom has passed through a caustic. The waveform resembles the derivative of an N wave, i.e., each frequency component has experienced a 90 degree phase shift. The double-peaked wave(e) still resembles an N wave with few irregularities in the expansion part, but two peaks of similar magnitude occur at the bow shock location and usually also at the tail shock. Multi-peaked waveforms (f) are similar but have three or more distinctive spikes at the bow and tail shock. The presence of many spikes of nearly equal amplitude gives the bow shock a flat-top appearance. Finally, sonic boom signatures that do not fit in any of the previous classes are classified messy(g). Notice that all classes have the common property that the distortion at the tail shock is very similar to that at the bow chock.

The implication is that the bow and tail shocks pass through the same pattern of random inhomogeneity.

Lipken, et al. (1997) had conducted the experiment to investigate the turbulence effects on the sonic boom signatures. They used an electric spark to create the shock wave and turbulent flow is generated by rectangular shape nozzle. As shown in Fig. 1-4, when the spherical shock wave interacts with turbulent flow, the peak overpressure of shock wave is significantly modulated. It was noted that peak overpressure levels are sometimes increased or decreased due to the turbulence. From their results, the mean peak overpressure becomes weaker with turbulence, while those standards deviations are remarkably increased. Therefore, it was shown that turbulence causes an enormous increase in variability of the peak pressure in sonic boom propagation.

1-2-3 Scope of this study on sonic boom

In the past, much attention was paid experimentally to prediction of the distortion of the sonic boom, since actual measurement of sonic boom has some problems such as expensive cost and difficulty of measurement.[Maglieri, D. J., et al., (1992); Lee, R. A., et al., (1991)] Also, details explanation on distortion of sonic boom is practically impossible because of measurement suffering in turbulent flow field. In model experiments on sonic boom distortion, ballistic range[Bauer, A. B., et al. (1970)], electrical spark [Ribner, H. S., et al. (1973)] and shock tube [Tubb, P. E. (1975)] had been used to produce the N-wave. These results presented that the turbulence causes large distortions of the shock fronts and an increase in rise time. Also, Bass et al.(1987) tried to obtain the correlation between rise time and atmospheric turbulence. However, it was mentioned only phenomenological estimation on the sonic boom distortion in relevant works.

Sonic boom distortion and exposure effects are very important research issue as well as the efforts on the sonic boom reduction such as a designing the aircraft body. If turbulence effects on the sonic boom signature are sufficiently known, it can be expected how to control the flowfiled near the aircraft for reduction of the sonic boom strength. As a result of this motivation,

this study describes the turbulence effect on the sonic boom. The shock wave is induced by Nd:YAG laser, and turbulent flow is generated by using a turbulence generator with longitudinal slit exit. Measurement of velocity distribution and visualization give help to find a behavior of shock wave distortion passed through the turbulence.

1-3. Drag Force

In this section, drag force will be highlighted to save the propulsion power of the aircraft. Drag reduction is one of the main objectives of the aircraft manufacturing. This directly concerns aerodynamic performance.

1-3-1. Components of drag force

Aerodynamic drag is commonly classified into tangential and normal pressure drag as shown in Fig. 1-5. Tangential drag force is characterized by skin friction drag, and determined almost entirely by the state of the boundary layer. In general, tangential drag is treated approximately as zero-lift drag, because friction drag is not sensitive in the change of angle of attack(AOA), namely lift condition being satisfied with attached flow condition. The effects of compressibility and heat transfer should be accounted for at supersonic speeds. The mean adiabatic skin-friction coefficient decreases by about 30%, regardless of Reynolds number, changing from incompressible speeds to Mach 2. In general, the tangential drag is strongly required to improve the lift-to-drag ratio of an SST, but is difficult because boundary layer transition due to crossflow instability near the leading edge. [Arnal, D. (1993)] This tangential drag does not vary greatly between subsonic and supersonic speeds. Turbulent flow control is generally considered for skin friction drag reduction.

Turbulent friction drag can be reduced by control the wetted area, reduction of roughness, and mass injection etc. [Bushnell, D. M. (1985)] Of these methods, represented method to control the turbulent friction drag is using a riblet [Walsh, M. J. (1980)] and large-eddy breakup devices [Hefner, J. N., et al. (1980)] In general, the friction drag reduction is strongly required to improve the lift-to-drag ratio of the SST, but is difficult because the boundary layer transition due to cross-flow instability is unavoidable.

Normal pressure drag can be classified into two types. The first one is form drag caused by viscous effects. When the air flows over the aircraft, flow separation is occurred and creates turbulent flow near the vehicle body. This opposes forward motion and is a component of the total drag. The supersonic form drag, or drag due to adding the boundary layer displacement thickness to the physical areas to obtain the effect of the boundary layer on the wave drag, is conventionally ignored.

Regardless of viscous effects, normal pressure drag has zero-lift drag term and lift-dependent drag term. The lift-dependent drag is called "wave drag due to lift". Furthermore, lift-dependent drag includes a component called induced drag at subsonic speed. This induced drag is also called wake drag or vortex drag, and occurs in airplanes due to lifting body redirecting air to cause lift. Wake drag increases as the angle of attack increases.

Finally, zero-lift drag is considered into aerodynamic drag force at supersonic speed. Shock waves are produced by deflections of the flow by airframe volumes, such as the cross-sectional area distribution and the thickness distribution of the body. This zero-lift drag corresponds to volume of aircraft body and is called "volume-dependent wave drag". In supersonic flow, this wave drag reduction is great issue because the total drag force is significantly increased with wave drag generation at more than transonic speed.

1-3-2. Wave drag in supersonic aircraft

Supersonic aircraft drag components are dramatically different from the subsonic cruise drag components. The large, obvious difference is the wave drag, a component that does not have a counterpart in subsonic flow. The lift-dependent and skin-friction drag components are analogous to their subsonic flow counterparts.

The wave drag produced by standing pressure waves that are not possible in subsonic flow has been traditionally decomposed into two components: a zero lift wave drag and a wave drag due to lift. In supersonic flight, the wave drag is the result of shockwaves present on the body, typically oblique shockwaves formed at the leading and trailing edges of the body. In

highly supersonic flows, or in bodies with turning angles sufficiently large, detached shockwaves, or bow waves will instead form. Additionally, local areas of transonic flow behind the initial shockwave may occur at lower supersonic speeds, and can lead to the development of additional, smaller shockwaves present on the surfaces of other lifting bodies, similar to those found in transonic flows.

1-3-3. Methods for wave drag reduction

In order to reduce the wave drag force, various configurations have been studied in supersonic and hypersonic flow conditions. All the proposed techniques had concentrated on reduction the shock strength in front of the body. In this section, supersonic wave drag reduction methods reported up to date will be introduced briefly. Methods are divided into 2 groups, mechanical and fluidic methods.

Mechanical methods

Spikes ahead of the blunt-nose with different spike-tip shapes are employed to mitigate the shock strength. [Hutt, C. R., et al. (1989); Guy, Y., et al. (2001); Jones, E. P., et al. (2000); Yamauchi, M., et al. (1993); Tanner, M. (1975)] Pressure drag on the body can drop up to 50% or more as a result of the generation of an additional conical oblique shock wave by the tip because it causes a substantial weakening of the normal bow shock wave in front of the blunt body nose. However, the choice of spike adds an extra weight to the aircraft. During maneuver such as pitching and yawing momentum, there is an additional side-force and friction drag acting on the body. And also, it is necessary to cooling system for thermal load in spike. [Bivolaru, D., et al. (2002)]

Fluidic methods

Injection method of counter-jet flow ahead of the nose was investigated by many researchers, and was reported that the bow shock strength is reduced, leading to reduced pressure at the nose. [Ballar, V., et al. (2006); Meyer, R., et al.(2010); Shang, J., et al.(2001)] Figure 1- 6

shows the schematic diagram of Ballar's experimental model. As seen in Fig. 1-6(a), the flowfield around the test model in the hypersonic flow with an opposing supersonic jet emanating from the stagnation point of the model. They obtained that the drag force measured using an accelerometer based force balance system was reduced up to about 45% with opposing supersonic jet. However, this is an active method, which requires an extra energy source and extra weight to the body. It is important to note that this kind of jet opposing the incoming flow might results in the establishment of vibration of shock wave. For certain range of frequency, the vibration of shock wave cause severe unsteadiness to the wave-dominated flow field around the body leading to undesirable unsteady problems.

Breathing blunt nose(BBN) was proposed to reduce the wave drag force by Imamura et al.(see Fig. 1- 7) [Imamura, O., et al. (2008); Vashishtha, A. et al. (2009)] In this technique, flow is allowed to pass through a small hole in the nose of a blunt-nosed body and made to come out through the base. Because of the relief offered by the breathing, the strength of the bow shock is reduced as the flow passes through the hole at the nose. As shown in Fig. 1- 7, the high-pressure flow is injected into the suction zone at the base. The high-pressure flow discharged at the base reduces the suction, which results in the increase of base pressure. Due to these processes, a significant reduction in the drag on the body is accomplished. The additional advantage of the breathing mechanism is that the heat generated at the body surface due to skin friction is convected away by the air which flows over the inner surface. In accordance with their results, 10% drag reduction was achieved with this method at Mach 7 hypersonic flow. However, this scheme has a design problem in actual application.

Recently, the most attractive scheme to reduce the wave drag force is weakly energy deposition which is produced by laser, micro wave or electric spark. In the past few decades, laser application technique was suggested to improve and control the aerodynamics performance. The intensive heating gas generated by laser beam focusing is useful to control the supersonic flow field. As shown in Fig. 1- 8, when the laser energy is deposited into the air, residual laser-heated gas interacts with bow shock wave in front of supersonic flight. Thereafter, laser-heated gas is transmitted to shock wave, and vortex is generated by well known baroclinic effects [Sasoh, A. et al. (2006); Ogino, Y., et. al., (2009)], and counter flow is generated with several vortex rings. This energy deposition technique has received much attention recently in the field

of next generation technique for supersonic aircraft, and related investigations have been much conducted.

Baroclinc effects can be explained from the vorticity equation. Beginning with the Euler equation and taking the curl, one obtains the equation of motion for the curl of the fluid velocity. The vorticity equation is defined by,

$$\frac{D\vec{\omega}}{Dt} = (\vec{\omega}\cdot\vec{\nabla})\vec{V} - \vec{\omega}(\vec{\nabla}\cdot\vec{V}) + \frac{1}{\rho^2}\nabla\rho\times\nabla p \qquad (1\text{-}1)$$

,where $\vec{V}$ is the velocity and $\vec{\omega}$ is the vorticity, p and ρ are pressure and density, respectively. In Eq. (1-1), the baroclinic contribution is the vector

$$\frac{1}{\rho^2}\nabla\rho\times\nabla p \qquad (1\text{-}2)$$

This vector is of interest both in compressible fluids. It is also of interest in the creation of vorticity by the passage of shocks through inhomogenous media, such as in the Richtmeyer-Meshkov instability.

In the first experiment for wave drag reduction using energy depositions, CO_2 laser pulses with repetition frequency of up to 100 kHz was used at Mach=2 argon flow. [Tret'yakov et al.] Figure 1 - 9 shows their experimental results; (a) visualization result without energy deposition, (b) visualization results with 100kHz laser pulses energy depositions, and (c) drag reduction. In Fig. 1 - 9 (c), it was achieved a significant drag reduction of up to 45 % of the baseline drag. However, the efficiency of energy deposition was obtained smaller than unity.

Adelgren et al. (2005) had conducted a single laser pulse energy deposition over a sphere in a supersonic flow with Mach number of 3.45. An energy was deposited using an Nd:YAG laser pulse (wave length; 532nm, pulse duration; 10 ns, pulse energy; 12 to 300mJ). They clearly visualized the interaction mechanisms between a laser-heated gas, see Fig. 1 - 10, and a shock wave and local pressure histories were measured using a piezo-resistive pressure transducer that was recess mounted in the sphere model. However, they conducted only single-pulse shot – an acting spike was not formed. In the similar manner, Sakai et al. (2008) conducted an experiment in an in-draft wind tunnel with Mach number of 3.0, and measured the stagnation pressure

history using a flush-mounted piezoelectric pressure transducer, which was reproduced in their own numerical simulation.

An alternate way of creating a low density gas in front of a bow shock is to use a powerful microwave source. Beaulieu et al. (1998) were performed the experimental study. A localized microwave discharge was generated upstream of a model in Mach 1.4 flow. A parabolic reflector was employed to focus the microwaves from the source which was located outside the wind tunnel. The schlieren method was employed to observe the shock wave and the influence of the energy addition in the flow. In the work carried by Exton et al. (2001), the generation of a plasma discharge in the near flow field ahead of a supersonic model was achieved by the microwave source. The micro wave pulses were square wave shaped with maximum duration of 3.5 μs. It was found that for a thin plasma, there is no noticeable difference in the shock stand-off distance or shape whether the plasma is present or not.

Recently, Sasoh et al. (2010) successfully measured the time-averaged drag reduction modulated with repetitive laser pulse energy depositions up to 10kHz. (see Fig. 1-11) They used a load cell controlled by back pressure to estimate the drag reduction performance, and obtained drag reduction of 3% with energy deposition efficiency of 10. They also showed significant visualization results on the evolution of flow field affected by repetitive laser-heated gases. However, since laser pulses were irradiated from head of model, refraction problem of laser beam was occurred. Therefore, the disturbed shock layer degrades the effective laser power transmission performance at a high repetition frequency of around 10 kHz.

1-3-4. Scope of this study on wave drag reduction due to energy deposition

Since the energy deposition scheme had received much attention to reduce the wave drag of supersonic aircraft, many research groups conducted an experimental and numerical study to verify the possibility of energy deposition for wave drag reduction. However, most experimental studies treated one or a couple of laser pulse. [Schulein, E., et al., (2009); Lashkov, V. A., et al. (2007); Kolesnichenko, Y. F., et al. (2007); Zaidi, S. H., et al. (2004)] Although they well

described the interaction phenomenon between heated source due to the energy deposition and shock layer, and shock mitigation, drag reduction performance due to repetitive energy depositions is significantly different compared to one of single energy deposition because of pulse-to-pulse interaction effect. Therefore, drag reduction performance with repetitive energy depositions should be explored to expect the better drag reduction performance.

In spite of many efforts on energy depositions for drag reduction, understanding of detailed mechanisms of high-repetitive laser pulse energy depositions to the shock layer is still poor primarily because any experimental work has not yet succeeded to diagnose the real flow fields induced by highly-repetitive energy depositions. In this thesis, drag reduction performance is investigated experimentally with high-repetitive laser pulses. To estimate the drag reduction performance, drag force is measured by using force balance system. Stagnation pressure history and schlieren images are obtained. The Interaction behavior among the vortex rings which forms a virtual spike ahead of a cylinder model is characterized. And the drag reduction performance over a truncated cone model which is proposed to trade-off between the magnitude of drag force reduced and power gain due to energy depositions is also investigated.

1-4. Purpose of This Thesis

The purpose of this thesis is to improve supersonic aerodynamic performance related to sonic boom and wave drag through shock wave interactions. Details of each chapter are as follow.

Chapter 2 is contributed to the sonic boom issue in supersonic transport (SST). In particular, to demonstrate the effects of turbulent flow on sonic boom, this study concentrates on the shock wave-slit jet interaction phenomenon. So far, it was known that the turbulence leads to the sonic boom attenuation on statistically. However, the details mechanism of overpressure modulation due to the turbulence was not yet reported. The main objective of this chapter is to verify the mechanism in shock wave modulation and to present the interrelation of the peak overpressure and the shapes of shock wave distorted by the turbulence. Laser induced shock/blast wave propagates around and interact with turbulent flow caused by slit jet. Due to the interaction between shock and slit jet, it is found that turbulence causes the shock strength variation. On statistical results, strength of distorted shock wave becomes weaker while its standard deviation is significantly increased. And also, shock wave moderated and its strength is interrelated with shape of distorted shock wave.

In chapter 3, another issue, wave drag reduction, in SST is mentioned. In this chapter, energy depositions scheme is applied to improve the wave drag performance. Even though many experimental results had been presented the possibility of energy deposition scheme with single pulse, researches on the drag reduction performance with repetitive energy depositions are quite limited. However, single-pulse performance evaluation might not reflect sufficiently characteristics of repetitive pulse operation, because the drag performance and associated flow are influenced by preceding pulses. In this chapter, high-repetitive laser pulses up to 50kHz are irradiated in front of the flat-faced cylinder model to improve the wave drag reduction performance. First of all, time-dependent stagnation pressure owing to laser induced heated gas is presented. Here, variation in stagnation pressure is clearly explained with visualization results.

For the constant laser pulse energy, the drag reduction performance almost linearly increases with increasing repetitive laser frequency. Also, in order to optimize the drag reduction performance, it is presented how to combine the pulse energy and laser frequency under the same input power conditions.

Interaction characteristics among the vortex rings are introduced in chapter 4. When the laser energy is deposited in front of the supersonic flight body with high-repetitive laser frequency, laser-heated gases interact with bow shock layer and several vortices with finite vorticity are generated as a result of baroclinc effect. In this chapter, mutual interactions among the vortex rings having three-dimensional nature, which lead to building-up an acting spike in the shock layer, are observed using high-speed framing schlieren images and stagnation pressure measurement with various laser pulse repetition frequencies of up to 60 kHz. It is presented transitions of the interaction mode among vortex rings with repetition laser frequency.

Chapter 5 describes the drag reduction performance over a truncated cone model. In chapter 3, the drag performance on a flat-faced cylinder model was treated. In this chapter, to improve the drag reduction performance and to examine the actual application of energy deposition scheme, experimental results on the truncated cone model are presented. With a flat-faced truncated cone model, the drag reduction is not sufficiently obtained because of a large base line drag. Therefore, to enhance the drag reduction, a concave-faced truncated cone is proposed, and results are discussed.

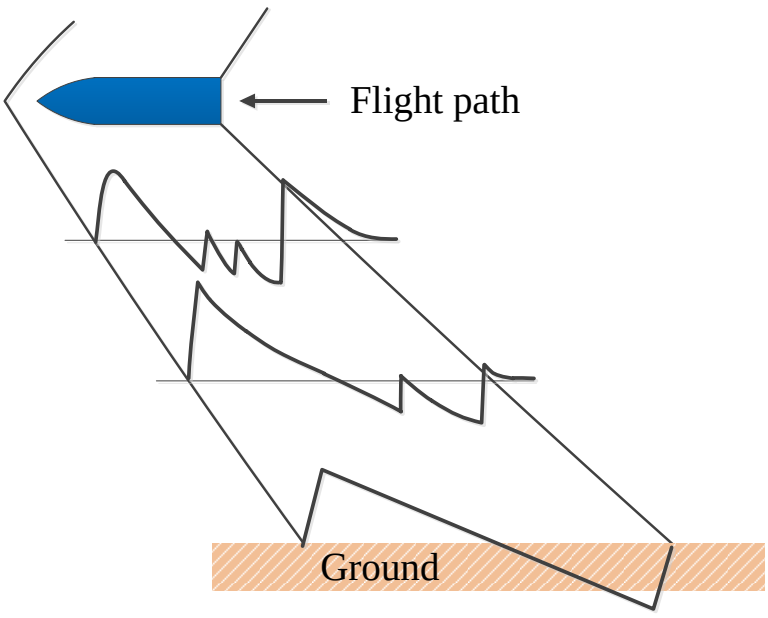

Figure 1 - 1 Evolution of the sonic boom signature

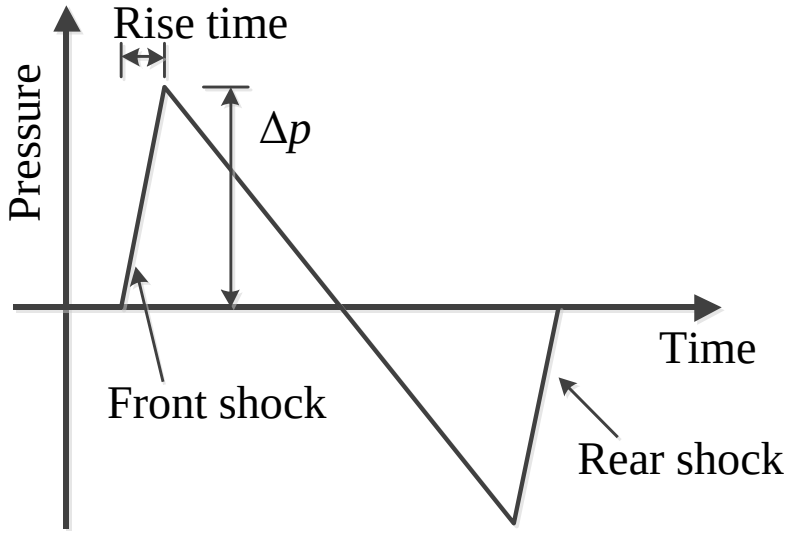

Figure 1 - 2 Conventional N-shape wave

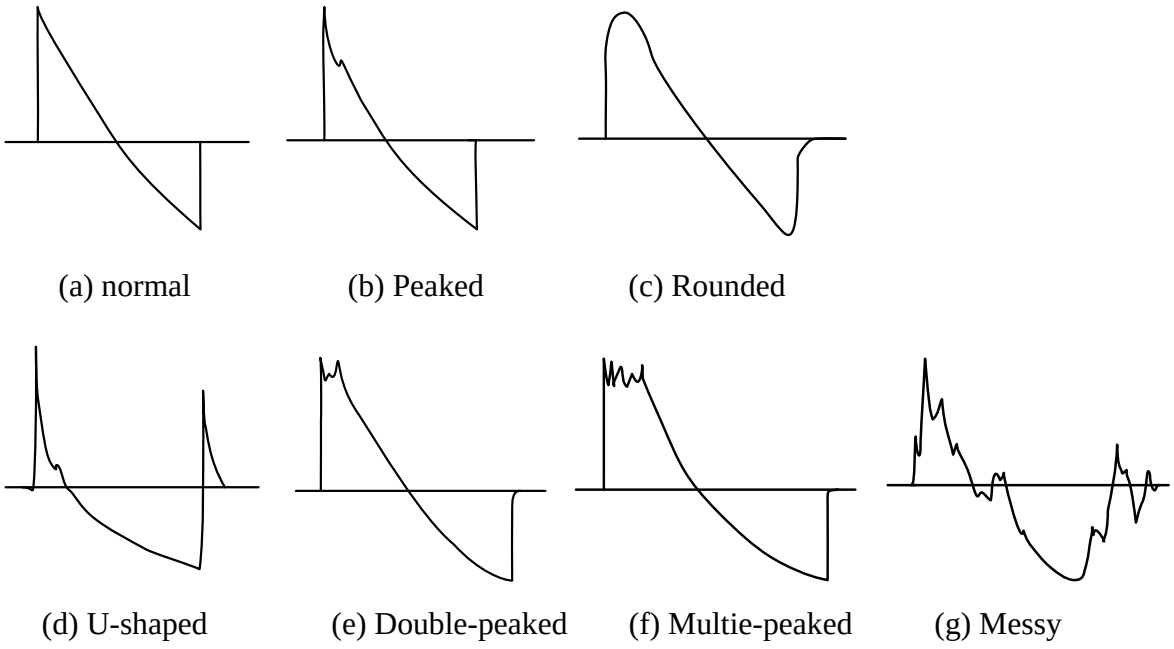

Figure 1 - 3 Classification of distorted N-shape wave by Gionfrido's scheme [Lee, R. A., et al (1991)]

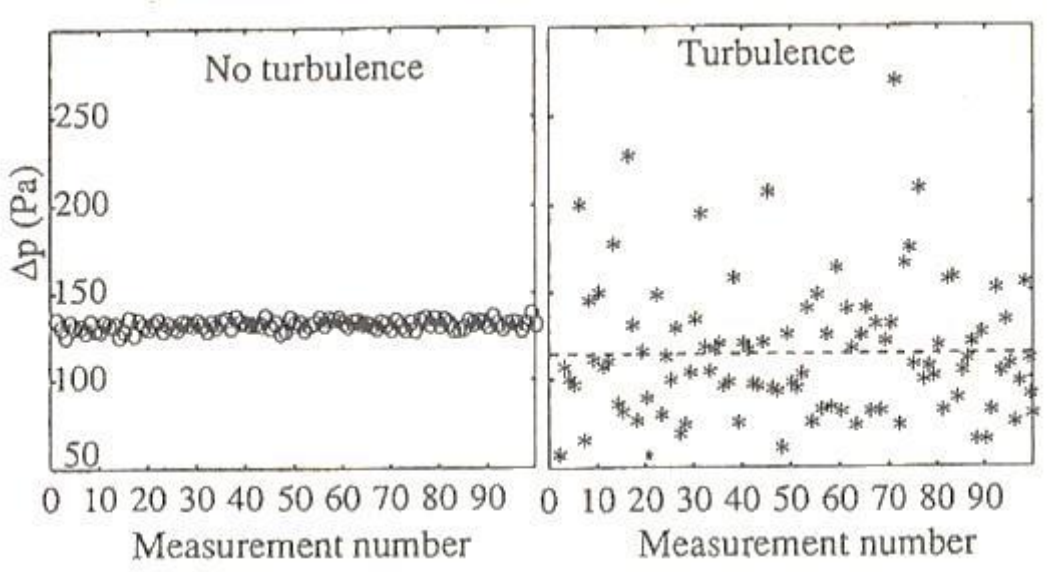

Figure 1 - 4 Peak overpressure scatters of spherical N waves measured with and without turbulence, dashed line shows the averaged peak overpressure without turbulence [Lipkens, B., et al. (1997)]

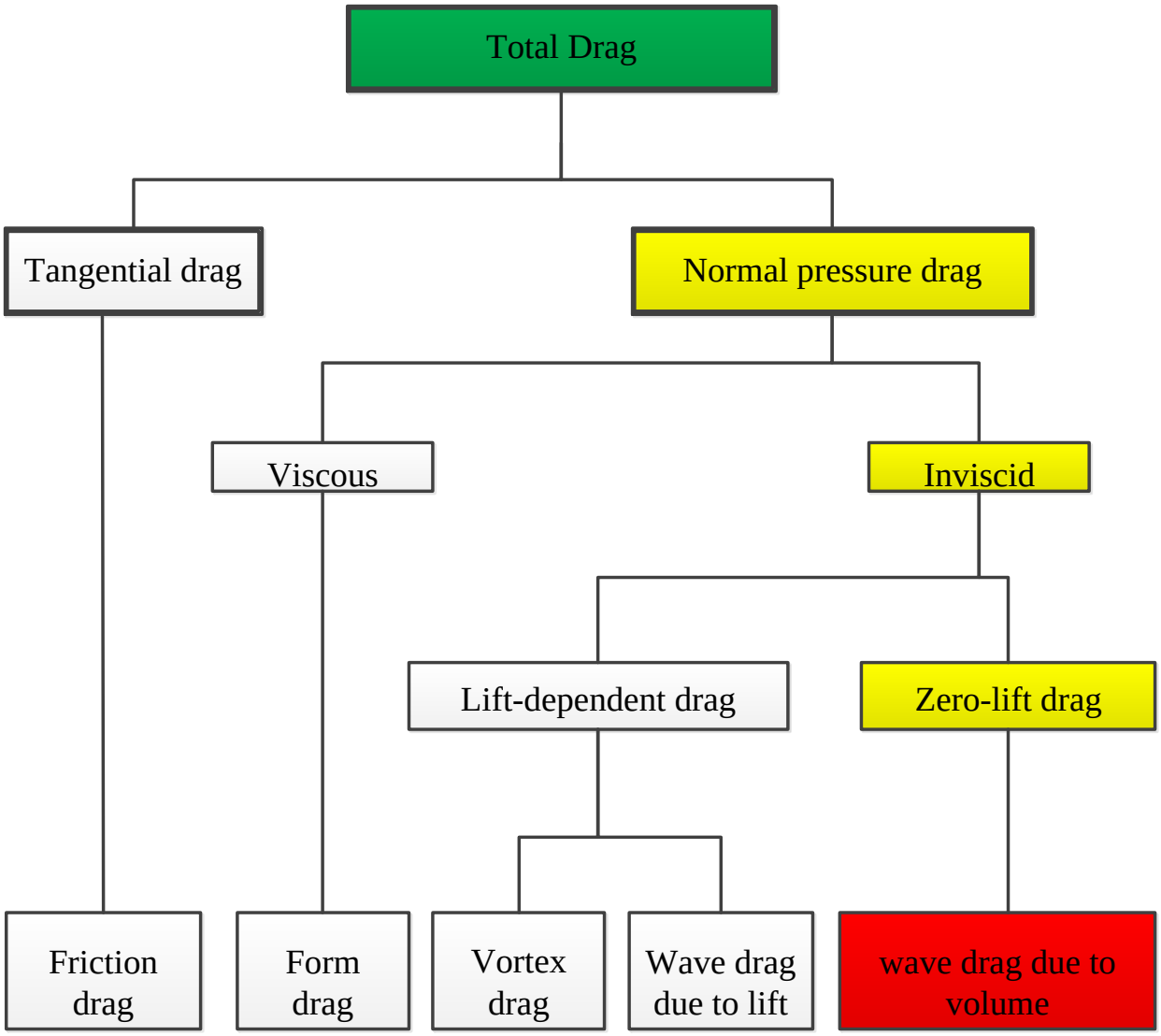

Figure 1 - 5 Component of aircraft drag force [Covert, E. E., et al. (1985)]

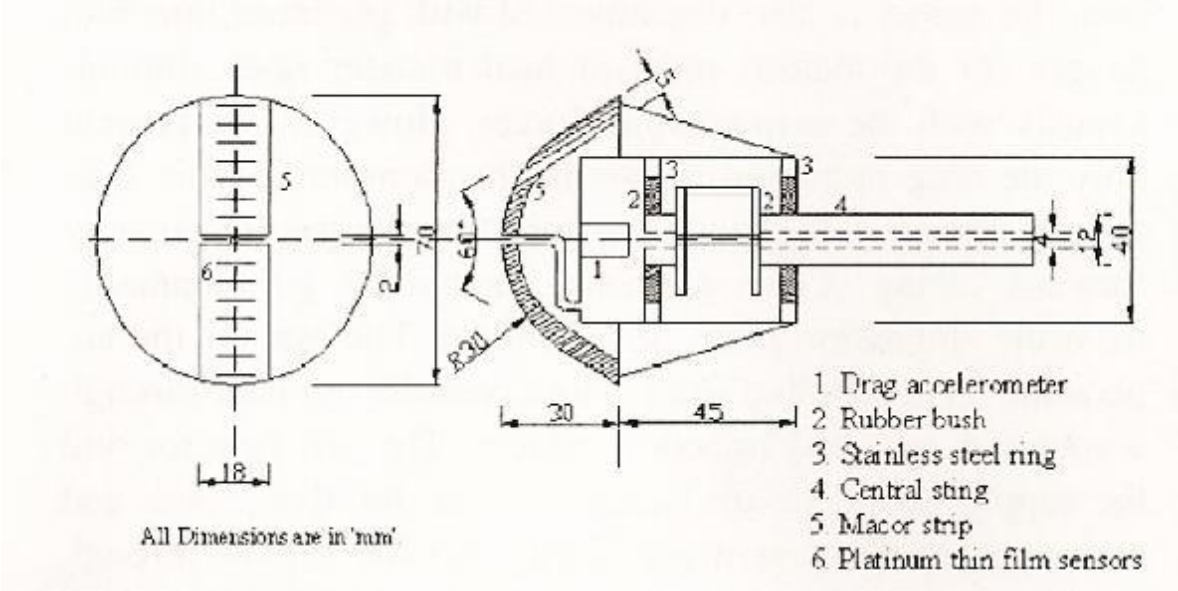

(a)

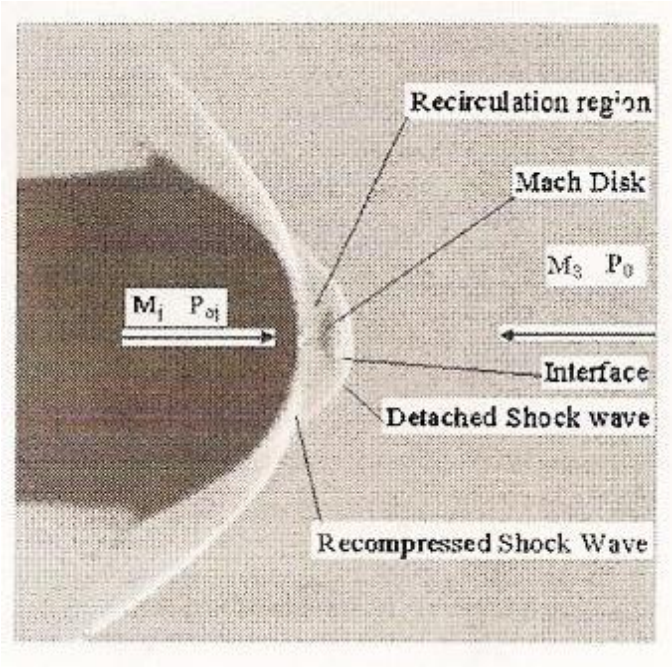

(b)

Figure 1 - 6 Injection method; (a) configuration of injection system, (b) flow features over a blunt cone with an opposing supersonic jet [Balla Venukumar, G., et al. (2006)]

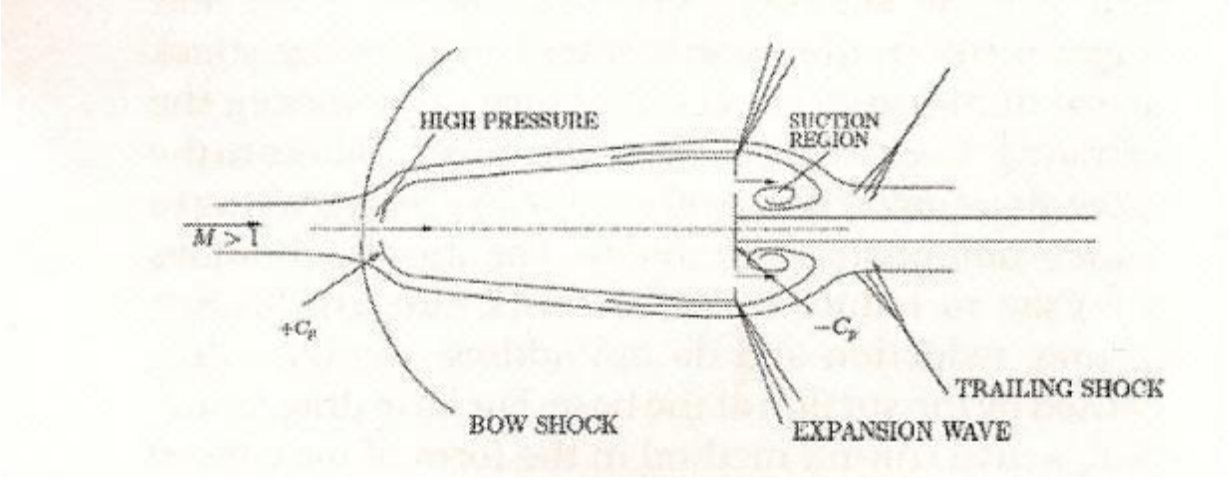

(a)

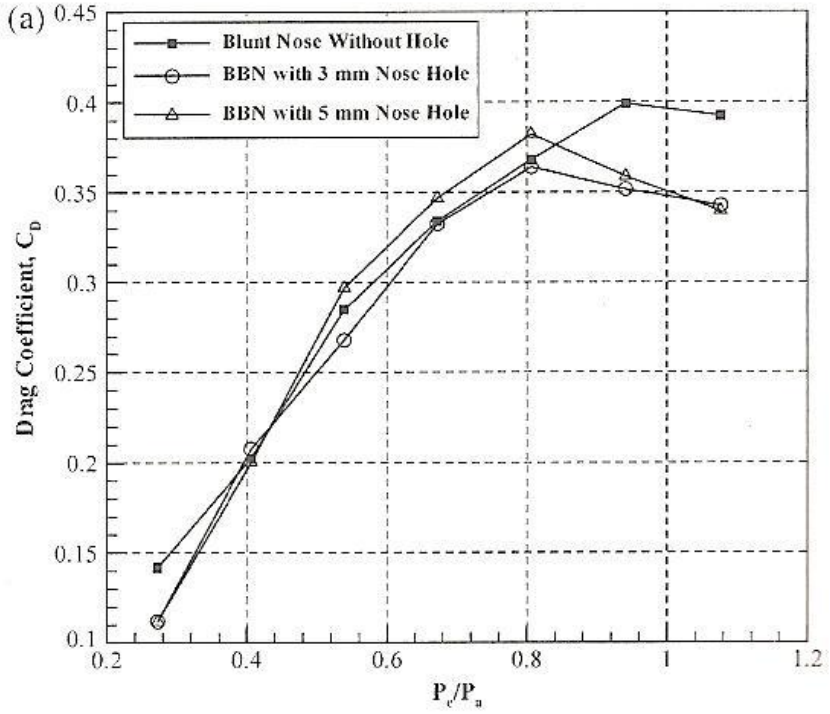

(b)

Figure 1 - 7 Breathing Blunt-nose method, (a) illustration of breathing blunt-nose model, (b) drag coefficient variation with nozzle pressure ratio; p_t / p_a = nozzle pressure ratio (total pressure/ambient pressure) [Vashishtha, A., et al. (2009)]

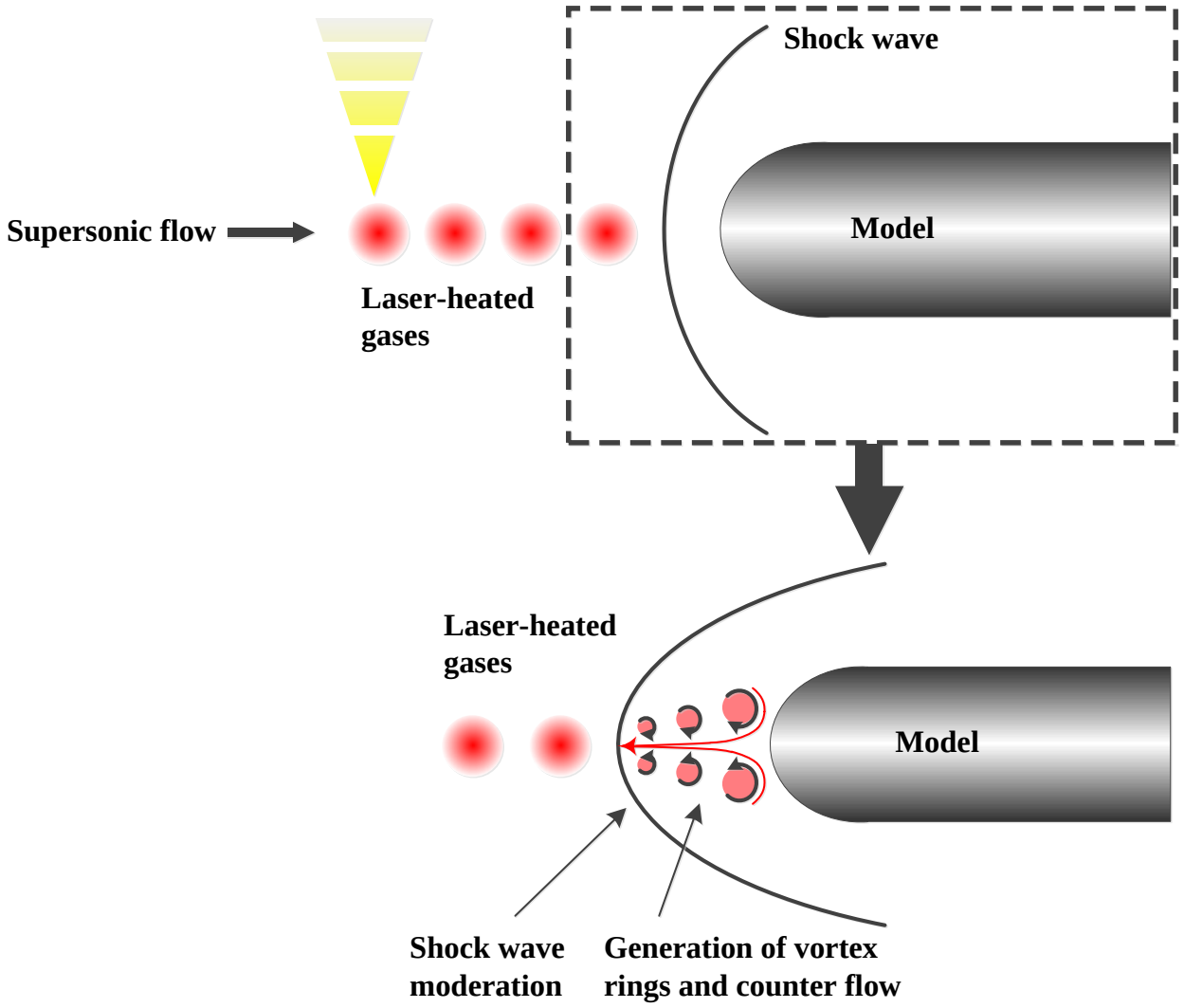

Figure 1 - 8 Concept of drag reduction using energy depositions

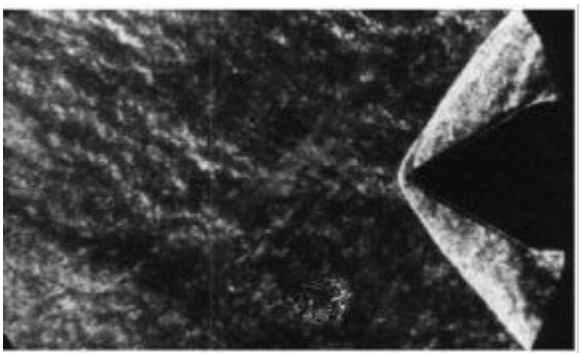

(a)

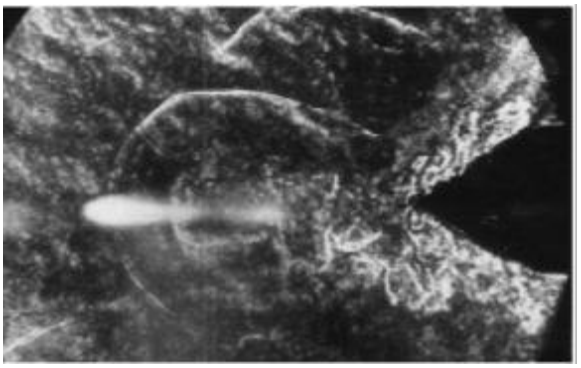

(b)

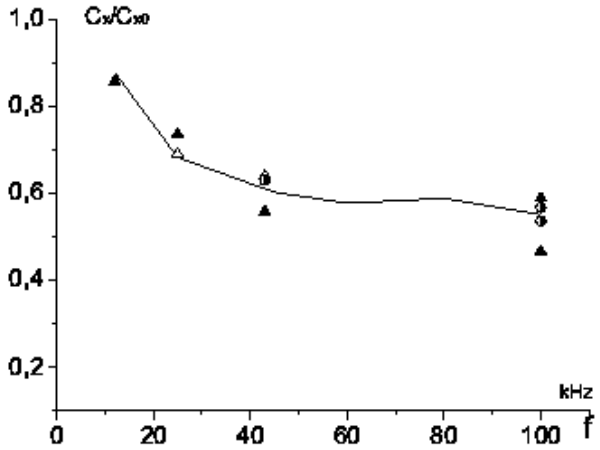

(c)

Figure 1 - 9 Shock wave deformation before(a) and after(b) the energy depositions of 100kHz, and drag reduction up to 40% over cone shape model; c_x=drag coefficient, c_{x0}=base drag coefficient without energy depositions [Tretyakov, P. K., et al. (1998)]

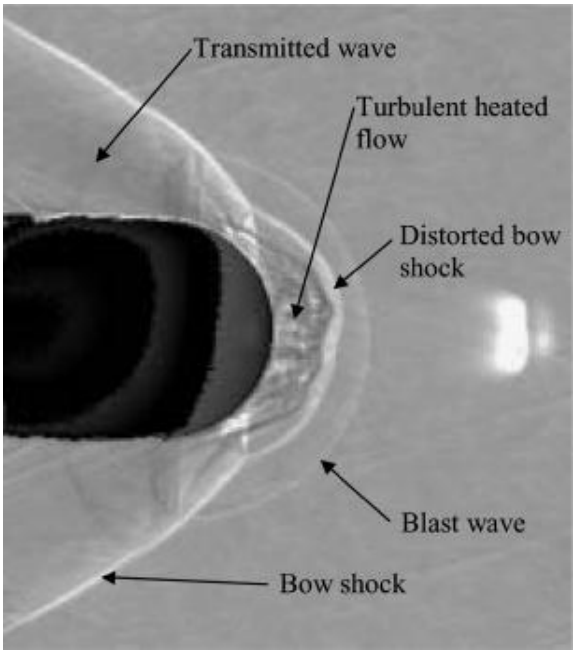

(a)

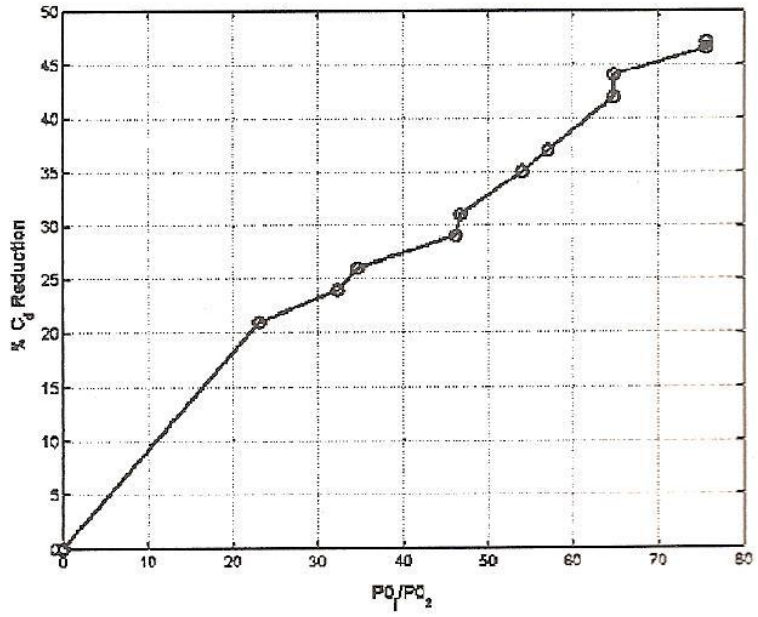

(b)

Figure 1 - 10 Counterflow method for wave drag reduction, (a) Flow feature over a blunt cone, (b) drag reduction with the ratio of counterflow total pressure to the pitot pressure [Balla Venukumar, G., et al. (2006)]

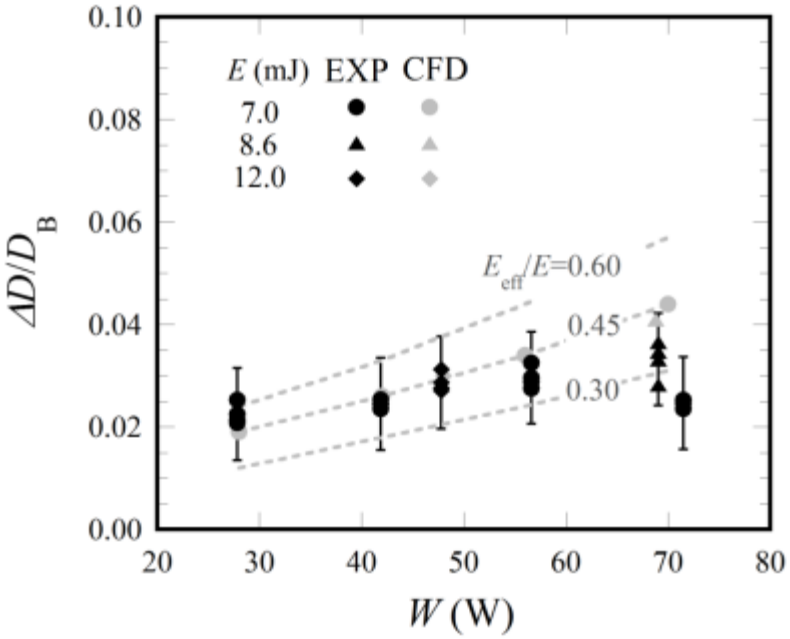

(a)

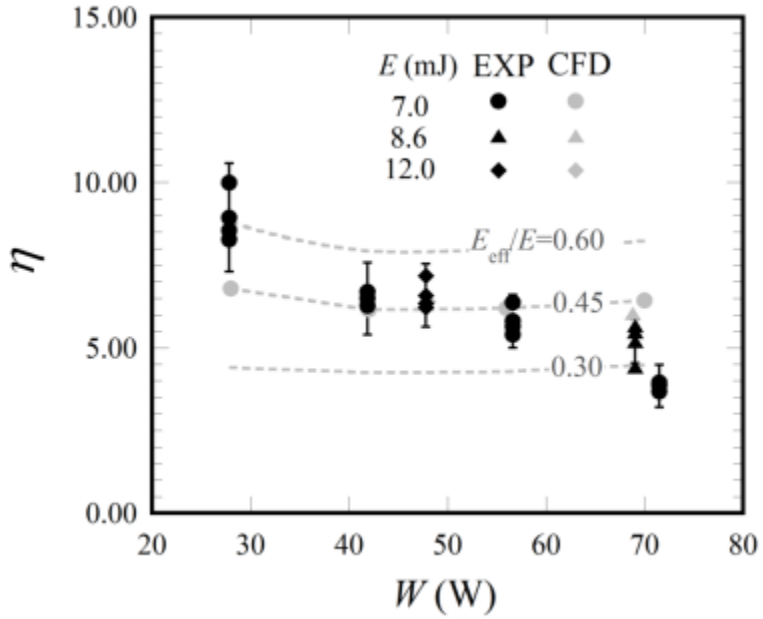

(b)

Figure 1 - 11 Drag reduction performance with laser pulse energy depositions up to 10kHz, (a) amount of drag reduction, (b) efficiency, η, of energy deposition; D_B=base drag force without energy depositions [Sasoh A., et al. (2010)]

Chapter 2. Weak Shock Wave and Turbulent Slit-Jet Interaction

This chapter describes weak shock wave and turbulent slit jet interaction phenomenon. Background is sonic boom mitigation due to turbulent atmospheric conditions. Pressure modulation of a weak shock wave induced by an Nd:YAG laser pulse when passing across a turbulent slit jet was experimentally investigated. With the slit jet the peak overpressure reduces on an average while its standard deviation becomes significant. Using schlieren visualization method, relationships between an overpressure history and shock front deformation are reported remarkably in this chapter. The peak overpressure was increased when the inherently-spherical shock wave was locally flattened, whereas it was decreased when a hump in the shock wave front was formed.

2-1. Introduction

The behavior of a weak shock wave presents problems both to compressible fluid dynamics and to nonlinear acoustics. For instance, the so-called 'von Neumann paradox' [Ben-Dor, G. (2007)., and Colella p. et al. (1990)] is a problem of oblique shock wave reflection occurring when the reflected wave is so weak at the intersection with the incident shock wave that its behavior is not simply determined from the three-shock-theory. The sonic boom is another example in which weak shock wave behavior is complex when propagating over a long distance. [Niedzwiecki, A. et al. (1978), Bass, H. E. et al. (1987), and Takayama, K. et al. (1995)]

In sonic boom propagation, its peak overpressure and waveform characteristics are varied depending upon the propagation medium or topography. In particular, when a shock wave propagates through turbulence, the post-shock pressure field is significantly modulated. However, current understanding of the associated mechanisms is quite limited.

The interactions between a shock wave and a vortex have been much studied. Ribner et al. (1987) obtained an analytical expression of acoustic wave emission caused by shock-vortex interaction from a linear theory. Ellzey et al.(1995) classified shock-vortex interaction into a weak and strong ones. The weak interaction involves small shock wave deformation and acoustic

wave emission which could be predicted by the linear theory. The strong interaction involves large shock wave deformation, leading to the formation of complex shock patterns. Chatterjee reported that the type of shock pattern formed in compressible vortex-shock wave interaction depends strongly on an incident shock Mach number. [Chatterjee A. (1999)] Three-dimensional shock deformation resulting from the interaction between a spherical shock wave and a vortex ring was studied in Refs. [Minota, T. (1993)) and Minota, T. et al. (1998)]

Although the mechanisms of shock wave distortion due to vortices were well understood, the impact of the shock-vortex interaction on post-shock pressure modulation was not of a primary interest.

The post-shock pressure modulations resulting from the interaction with jets were studied using a conical shock tube by Ribner et al. (1973). In this study, the jet blew either in the same or in the opposite direction of the shock wave propagation. Fig. 2-1(a) shows the conventional overpressure profile without turbulence. An overpressure spike occurs in the leading part of a typical N-shaped pressure profile of the blast front(Fig. 2-1(b)) when the jet opposes the shock front, while the interaction of the shock wave with a jet in the same direction led to a rounded variation(Fig. 2-1(c)). Pierce argued that these pressure modulations could be modeled based on geometrical acoustics. [Pierce, A. D. (1968)]

Many studies on sonic boom generated from a supersonic aircraft dealt with the interaction of a shock wave and a turbulent flow. The primary interest is the modulation of the peak value and the rise time of the overpressure variation. Pierce (1972) reviewed the extent of the variability in overpressure waveforms recorded during actual flight tests; random nature of the waveform variability was classified into several types; a high peak overpressure corresponds to a spiked waveform, while a low one corresponds to a rounded waveform.

Lipkens et al.(1998) conducted laboratory model experiments of a weak shock wave modulation through a turbulent flow. A shock wave was generated using an electric spark and a turbulent jet flow was ejected from a slit**.** The turbulence caused enormous variability in the waveform of the post-shock overpressure. On average, the slit jet led to an increase in the rise time and a decrease in the peak overpressure. However, the standard deviation became much larger than the average decrement; implying that in some cases the peak overpressure was

enhanced although in majority it was weakened. Such ‘statistical’ behavior cannot be reproduced by deterministic computational fluid dynamics simulation. [Biringen S. et al. (2005)] The associated mechanisms of the pressure modulation warrants further investigations; under what conditions is the shock strength increased or decreased; how to deform the shock shape in the interaction processes.

The purpose of this study is to better understand interaction mechanisms between a weak shock wave and a turbulent flow, highlighting the relations between shock wave front deformation and post-shock overpressure modulation.

2-2. Experimental Methods

A schematic diagram of the experimental set up is illustrated in Fig. 2-2. A blast wave, a shock wave accompanied with an expansion zone behind, is generated by focusing an Nd:YAG laser pulse (wavelength of 1,064 nm, FWHM of 9 ns, output energy of 0.45 J) using a convex lens with a focal length of 100 mm. The overpressure is measured on the 200-mm-dia., 5-mm-thick, aluminum disk at 167 mm from the focus with a central, flush-mounted piezoelectric pressure transducer (Model-HM102A18, PCB Piezotronics Inc., rise time of 1 μs , natural frequency of 500 kHz). The axis of the disk is aligned to a direction of shock wave propagation. A sheet of shear flow from a slit on the upper plate of a stainless steel sub-chamber of an inner volume of 0.014 m^3, which hereafter will be referred to as the 'slit jet,' is supplied normal to the shock wave propagation direction. The sub-chamber overpressure from the atmospheric value (Δp_s) is kept at 20 kPa. The distance between the focus and the slit jet is set to110 mm.

The overpressure history measured with the pressure transducer A is caused by the reflection of a laser-induced blast wave against the disk surface. Expansion waves originated in the disk peripheral arrives at the pressure transducer about 580 μs after the initiation of an overpressure rise due to the blast wave. As will be seen later, the overpressure of the present interest lasts about 60 μs . During this period, the overpressure signal is not affected by the disk finite size. Although the uncertainty of the pressure transducer which the manufacturer claims equals ± 0.8 %, the measured overpressure signal contained larger oscillatory components of the natural frequency. As much as possible this component was eliminated in designing the transducer mount so as not to violate the validity and generality of the following results.

The x - and y - axes are defined as shown in the figure. The z-axis, not shown in the figure, is normal to them. The surface of the upper plate is on the x - z plane (-150 mm $\leq x \leq$ 150 mm, y = 0, -150 mm $\leq z \leq$150 mm). The slit has a 2 mm (-1 mm $\leq x \leq$ 1 mm) × 200 mm (-100 mm $\leq z \leq$ 100 mm) rectangular sides. The slit jet flows along the y - z plane, primarily in the y

direction. The disk axis and the focus is on a line of y = 100mm and z = 0mm, parallel to the x-axis.

Distributions of y component of a flow velocity and its fluctuation on z = 0 plane are measured using a CTA (Constant-Temperature Anemometer) type hot-wire. The hot-wire has a diameter of 5 μm. The output signals are recorded in a digital oscilloscope with a sampling frequency of 20 kHz. Hot-wire calibrations were conducted using a Pitot probe which was placed side by side in a low-turbulence wind tunnel where the turbulence intensity is estimated better than 0.18%. [Sakai, Y. et al. (2001)]

A Schlieren optical system is employed to visualize shock wave motions. It consists of two 300-mm-dia. concave mirrors (focal length; 3m) and a xenon flush lamp with a light intensity of 10 kW/sr and a nominal duration time of 200 μs. A knife edge which is placed at the focal point in the Schlieren optics vertically cuts off about half of the object beam. One hundred instantaneous images are sequentially taken using a high speed framing camera (HyperVision HPV-1, Shimazu Co., resolution 312×260 pixels) with a framing interval of 4 μs/frame.

In the present experiments the shock Mach number upon the disk, which is evaluated from the overpressure on the pressure transducer A, is of the order of 1.007, corresponding to a density jump of 2.5 % of the atmospheric density. With our optical setup, such a weak shock wave front yields a Schlieren image of poor contrast. In order to improve the quality of the flow visualization, a differential image is numerically obtained by subtracting a gray-scale Schlieren image at a past moment (reference image) from that at the moment of the interest (object image). The technically-same process is done in Background-Oriented Schlieren (BOS) method. [Ramanah, D. et al. (2007), and Richard, H. et al. (2001)]

However, in this study the differential image is used as it is, whereas in the BOS the deflection of a background image is used in evaluating the diffraction of rays. In this method, ahead of the shock wave of the past moment the steady-state background noise can be eliminated whereas the shock wave and accompanied flow can be captured with a much enhanced contrast; as will be seen later an instant shock wave shape is much clearly obtained.

2-3. Results and Discussion

Figure 2-3 and 2-4 present the turbulent flow field on the *x*-*y* plane (*z* = 0) measured by the hot-wire anemometer. The flow field was measured without the disk. At *y* = 50 mm, the slit jet slightly has a saddle-back profile because of vena contracta effects. The width of the slit jet (1 % $\bar{u}$) is estimated to be 96 mm at *y* = 100 mm, then increases along the *y*-axis, thereby becoming 128 mm at *y* = 200 mm. This velocity distribution is little disturbed by the disk at *x* = 75 mm. Due to the entrainment of mass flow, the centerline (*x* = 0 mm) velocity is gradually decreased along the *y*-direction; 31.5 m/s at *y* = 100 mm and 21.0 m/s at *y* = 200 mm. The flow field is almost symmetric; the extent of asymmetry in the mean velocity is smaller than 7.8 %. The turbulence intensity is referred as the ratio of the root-mean-square of velocity fluctuation (u_{rms}) to the mean velocity ($\bar{u}_0$) at *x* = 0 mm, *y* = 100 mm and *z* = 0 mm. The turbulence intensity in Fig. 2(b) has a saddle-back distribution near the slit. At *y* = 100 mm the peak value of the turbulence intensity equals 17.5 % at x = 10 mm. Then, the peak value is decreased and the distribution is converted into an almost-top-hat shape downstream. The peak value at *x* = 0 mm and *y* = 200 mm equals 11.8 %. Reynolds number of the slit jet is evaluated 4.7×104 based on $\overline{u_0}$(=31.5 m/s) and the FWHM(Full Width at Half Maximum) of the slit jet velocity (= 27 mm)at the reference point (*x* = 0 mm, *y* = 100 mm and *z* = 0 mm).

Figure 2-5 presents the representative overpressure (Δp) histories under the conditions of no-slit jet(a) and slit jet (b and c). Here, the time, t, is originated in the laser pulse initiation. The sequential enhanced Schlieren images are shown in Fig. 2-6, in which (a), (b) and (c) correspond to the respective symbols in Fig. 2-5. Each image is subdivided to four regions A to D, see Fig. 2-6(d). The region A is a differential image between t = 96 μs and 40 μs. Since at t = 40 μs the shock wave has not entered the view, this region corresponds to the distribution of density fluctuation at t = 96μs. In the same way, the region B correspond to an image at 176 μs obtained from differentiation between 176 μs and 96 μs, C at 256μs from 256 μs and 176 μs, and D at 336 μs from 336 μs and 256 μs, respectively. In this way, in each image four shock waves at *t* = 96

μs, 176 μs, 256 μs, 336 μs are visualized as dark shadows; an expansion region behind each shock wave is recognized as a bright zone. Figure 2-7 shows the distributions of shock front curvature evaluated from Figs. 2-6(a) to (c) at t = 336 μs. The local curvature, C, distributions are normalized to the curvature of a perfect sphere of the blast wave (C_0). After digitizing the x - y location of a shock wave front, it is fitted to a b-spline function using 4th order base functions.

The curvature measured without the slit jet, the case (a), is almost constant and closes to the spherical one (see Fig. 2-6). As seen in Fig. 2-5(a), when the shock wave gets reflected on the pressure transducer, the overpressure is suddenly increased to a maximum value, $\Delta p_{m,0}$, of about 3.1 kPa, which corresponds to a local shock Mach number of 1.007. Then due to the expansion the overpressure decreases. The secondary shock wave caused by the driver gas implosion appears as a small peak at t = 385 μs. After the secondary shock wave, the overpressure further decreases down to a negative value. At around t = 400 μs, the overpressure starts to recover toward the atmospheric value. This overpressure variation shows the typical pressure history of laser induced blast wave. [Liang, S. M. et al. (2001)] The post-shock overpressure lasts for effectively about 60 μs. The disturbance originating in the sub-chamber surface which may contaminate the overpressure history arrives thereafter; at about 194 μs after the impingement of the shock wave on to the pressure transducer A.

In the cases both of (b) and (c) in Fig. 2-6, before the shock wave passes the slit jet (t = 176 μs), the distortion of the spherical shock front shape is negligible. However, the shock wave becomes distorted when passing through it (t = 256 μs and 336 μs). In the case of (b), as seen in Figs. 2-6(b) and 2-7, the normalized curvature of the shock front near the pressure transducer is decreased, having a flat shape, locally almost as a normal shock. As seen in Fig. 2-5(b), the peak value of the overpressure, Δp_m, is increased to 3.5 kPa. Hereafter, such a case will be referred to as the 'strong case.' In the case of (c) in Figs. 2-5 and 2-6, the shock front has a hump slightly above the pressure transducer. As seen in Fig. 2-7, the curvature greatly oscillates around it. The curvature has a large positive peak. The local shock strength is weakened, having a smaller peak value of 2.3 kPa ('weak case,' hereafter).

Figure 2-8 presents the probability histogram of the peak overpressure measured with the slit jet obtained from fifty runs. With the slit jet, the number of events has a maximum at around Δp_m / $\Delta p_{m,0}$ = 0.7±0.05, spread from 40% to 160% of that without the slit jet. The mean and

standard deviation (σ) of the peak overpressure are given in Table 2-1. With the slit jet, the peak overpressure is decreased on average by 12% and its standard deviation is vastly increased by 27 % of the mean value of $\Delta p_{m,0}$ which is obtained without the slit jet. Similar characteristics were obtained by Lipkens et al. (1998);. They also used the rectangular slit with the width typically of 25.4 mm to generate the turbulent shear flow. The mean value of the peak overpressure in their experiment is 130.5 Pa. When a spherical shock wave propagates through the slit jet, the peak overpressure is decreased on average by 10 %; its standard deviation became to be 29 % of $\Delta p_{m,0}$.

Several modulation types of the peak overpressure and corresponding numerically-enhanced Schlieren images at t = 336 μs are presented in Figs. 2-9 (strong case) and 2-10 (weak case). The relationships between an overpressure history and shock wave deformation seen in Figs. 2-5 and 2-6 are clearly reproduced. In the strong cases of Fig. 2-9 where the peak overpressure exceeds the nominal value, in all cases the shock front has a flat shape in front of the pressure transducer. On the other hand, the shock front has a hump in the weak cases of Fig. 10. In both cases overpressure modulations after the peak value have various patterns; peaked type (Fig. 2-10(b-d)), rounded type (Fig. 2-9(a), Fig. 2-10(a) and (d)), multi peaked type (Figs. 2-10(b) and (c)). Although not shown in the paper, in a single run the transition between the strong and weak cases did not occur at all.

The shock wave distortions and overpressure modulations observed in this study seem to have the same characteristics appearing in shock-vortex interaction. [Ellzey, J. L. et al. (1995)] When a shock wave propagates in a region where the flow velocity is in the same direction, the shock velocity is increased, however the overpressure is decreased because the shock Mach number relative to the upstream becomes decreased. On the other hand, when a shock wave propagates in a region of the opposite flow velocity, the shock speed is decreased; the overpressure is increased because the shock Mach number is increased. However, in the cases of the present study the shock wave propagates through a complicated velocity field which spatio-temporally fluctuates. Many interactions occur at finer scales. The observed shock behavior is a result of integration of the interactions over the shear layer. The above-mentioned phenomenological explanation needs to be refined by better characterizing instant turbulent flow fields in the slit jet and by better diagnosing the interaction with the shock wave, which is beyond the scope of the present study.

2-4. Summary

In order to demonstrate the sonic boom distortion due to the inhomogeneous atmospheric conditions which is described turbulent flowfield. The interaction phenomenon between the laser –induced blast wave and slit jet flow was investigated. Propagation Mach number of blast wave caused by the explosion of laser beam was approximately 1.007. Slit jet was used to generate the turbulent flow.

The present study has obtained clear relations between the overpressure modulation and a local shock front deformation in a weak shock wave-turbulence interaction; When the peak overpressure is increased, the shock front becomes locally flat; the local curvature is decreased. When the peak overpressure is decreased, the shock front has a hump; the local curvature greatly oscillates. These shock wave modulations through a region of non-uniform velocity should be better diagnosed with finer spatiotemporal resolutions, so that microscopic shock-vortex interactions can be related with the macroscopic shock wave behaviors which are observed in the present study. This challenging scope warrants further investigations.

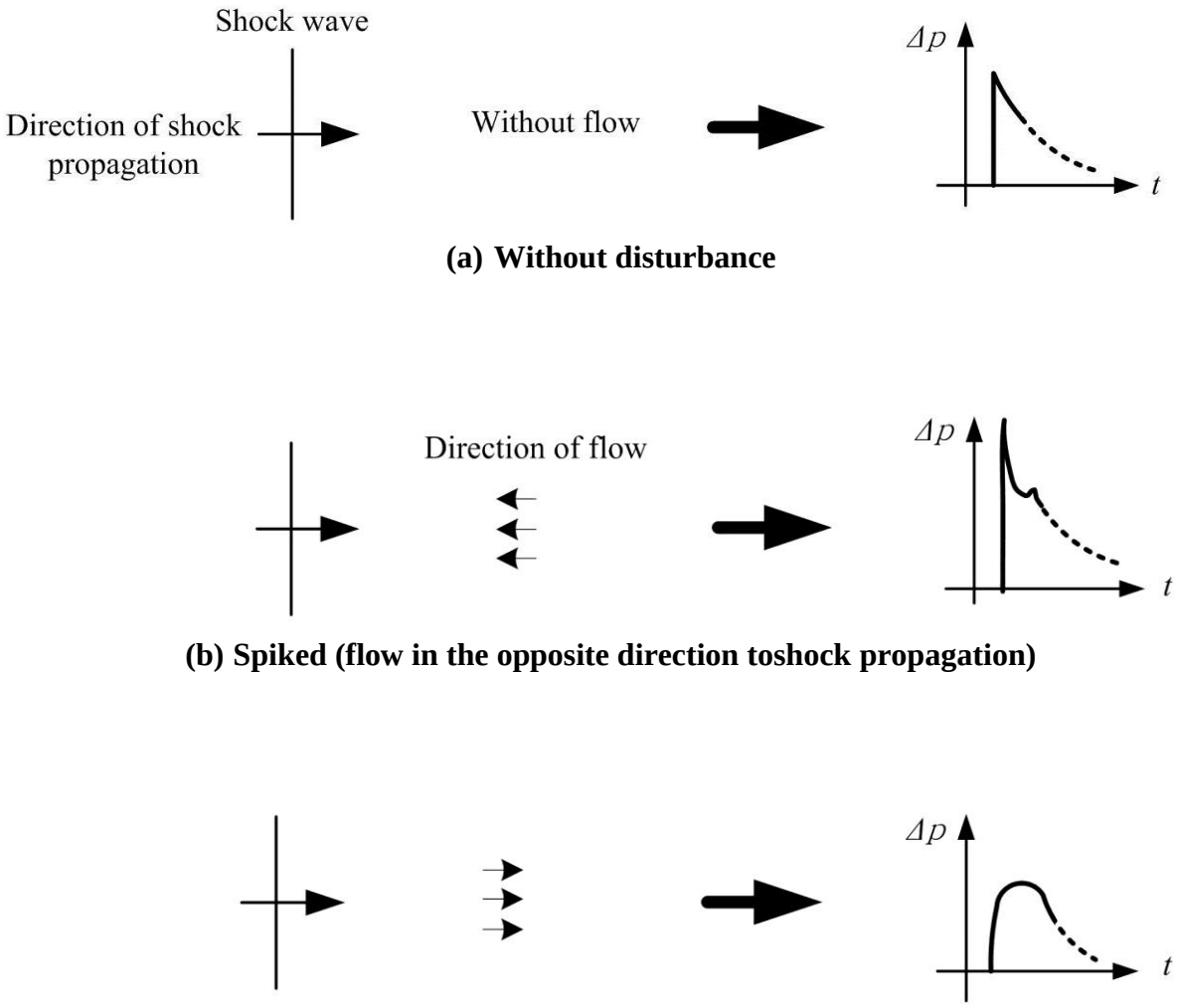

(a) Without disturbance

(b) Spiked (flow in the opposite direction toshock propagation)

(c) Rounded (flow in the same direction as of shock propagation)

Figure 2 - 1 Overpressure rise patterns after shock wave-flow interaction

Table 2 - 1 Statistical Results

	Mean value (kPa)	σ (kPa)
Without slit jet	3.11	0.03
With slit jet	2.73	0.85

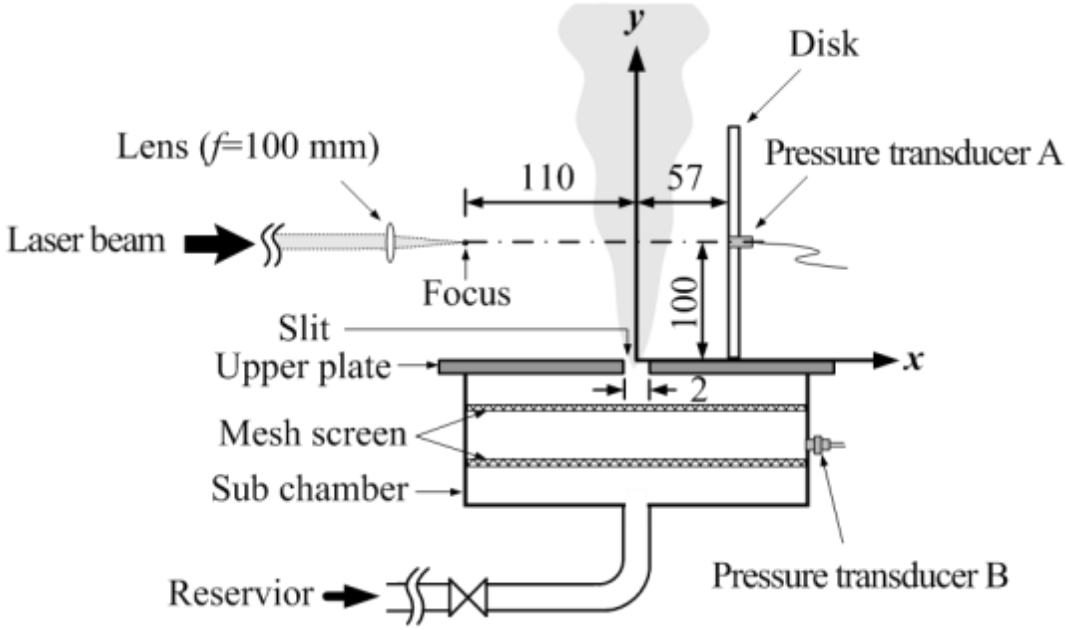

Figure 2 - 2 Schematic illustration of experimental set-up, unit in mm

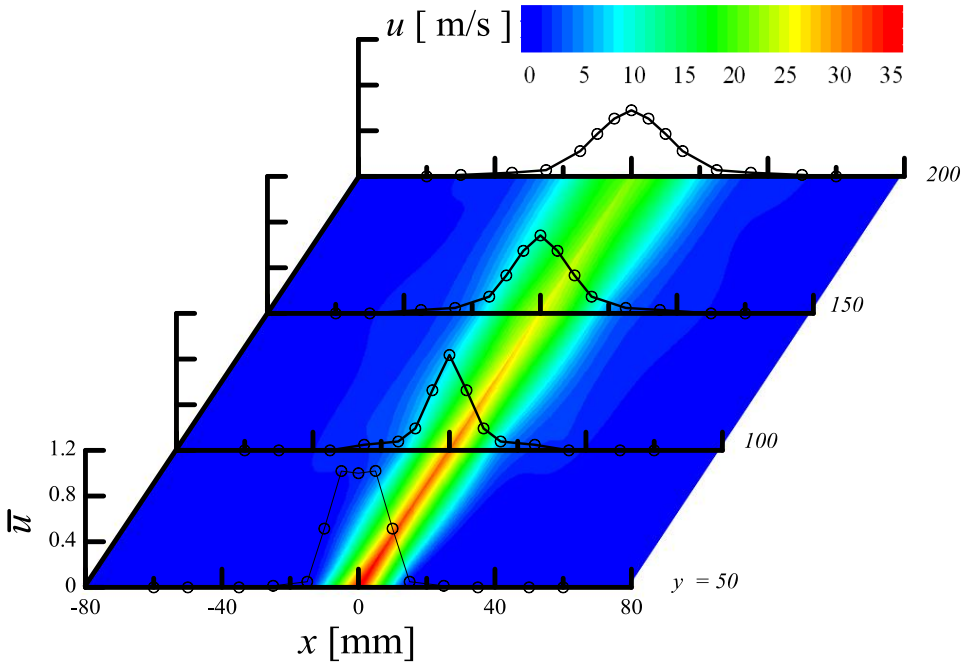

(a) $\bar{u}$ [m/s]

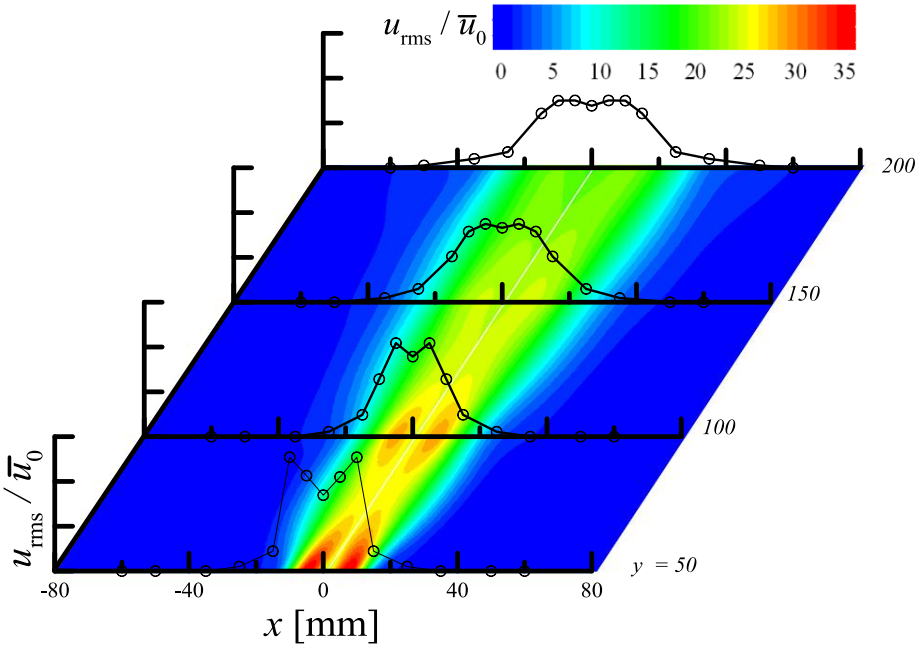

(b) $u_{rms} / \bar{u}_0$

Figure 2 - 3 Contours of mean velocity and turbulent intensity

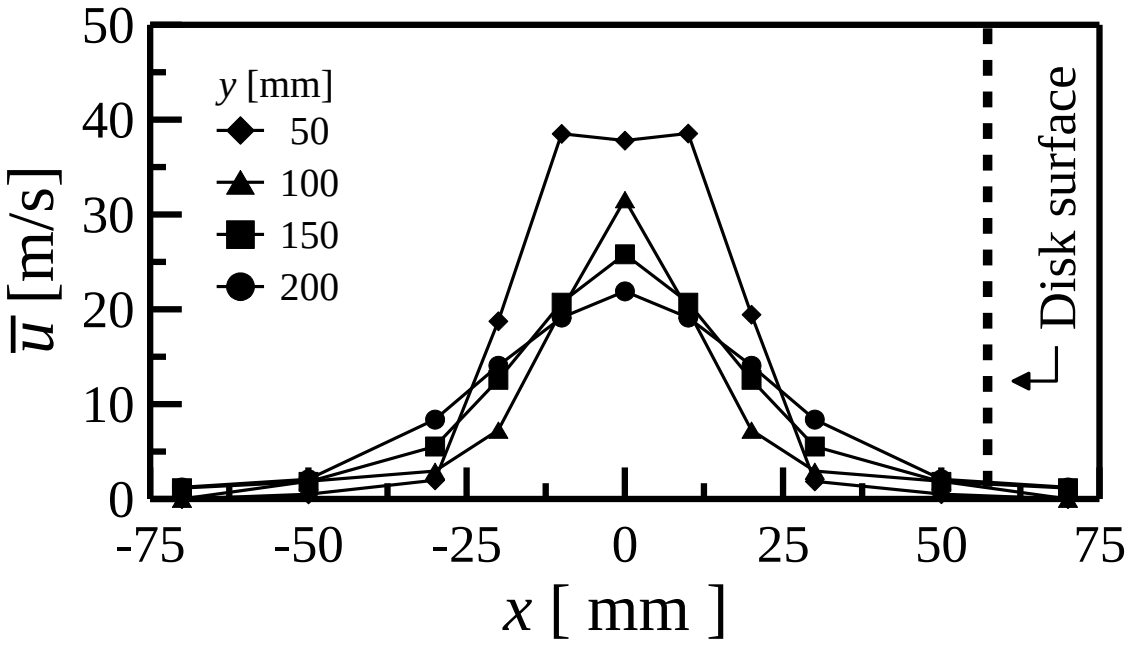

(a) $\bar{u}$ [m/s]

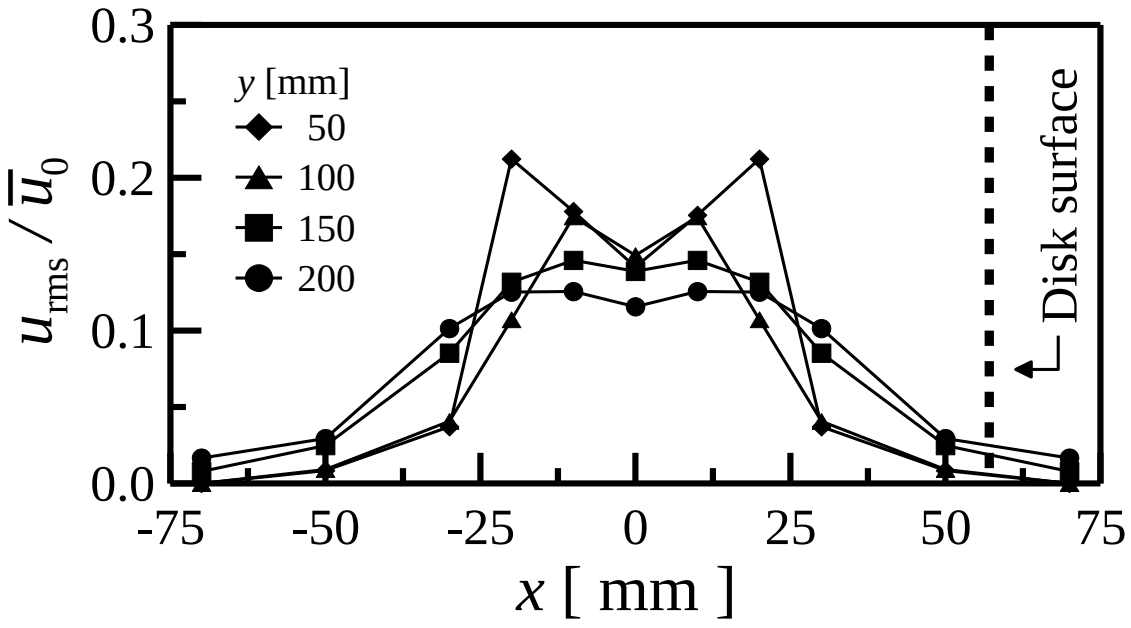

(b) u_{rms} / $\bar{u}_0$

Figure 2 - 4 Distributions of $\bar{u}$ and u_{rms} / $\bar{u}_0$ measured without the disk on *x*-*y* plane ; Δp_s = 20 kPa, Disk position is indicated for reference purposes.

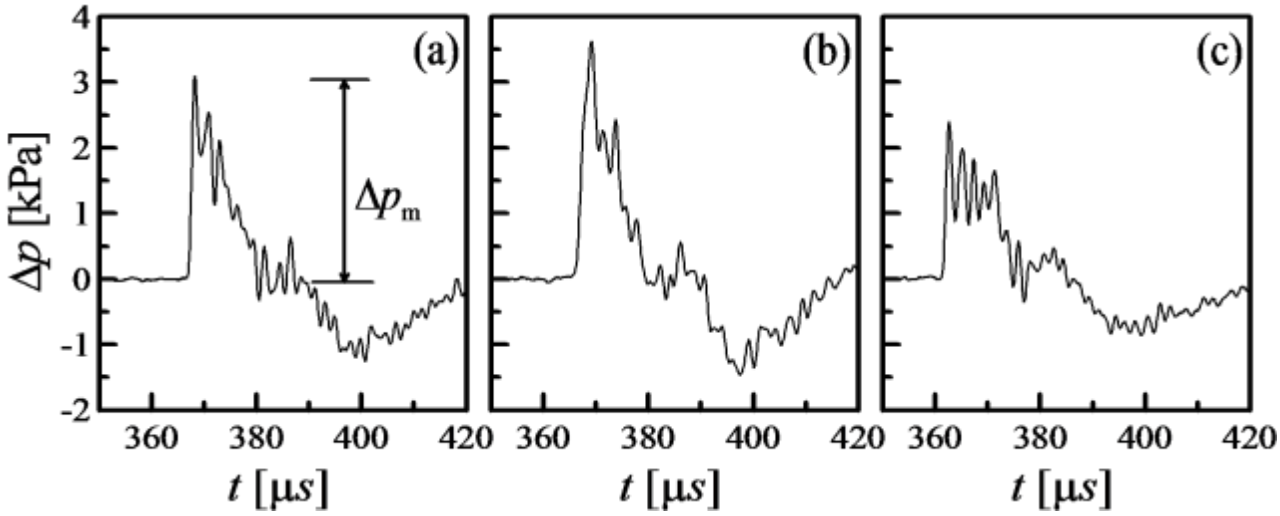

Figure 2 - 5 Examples of overpressure histories measured with pressure transducer A; (a) without slit jet, (b) with slit jet (strong case) and (c) with slit jet (weak case)

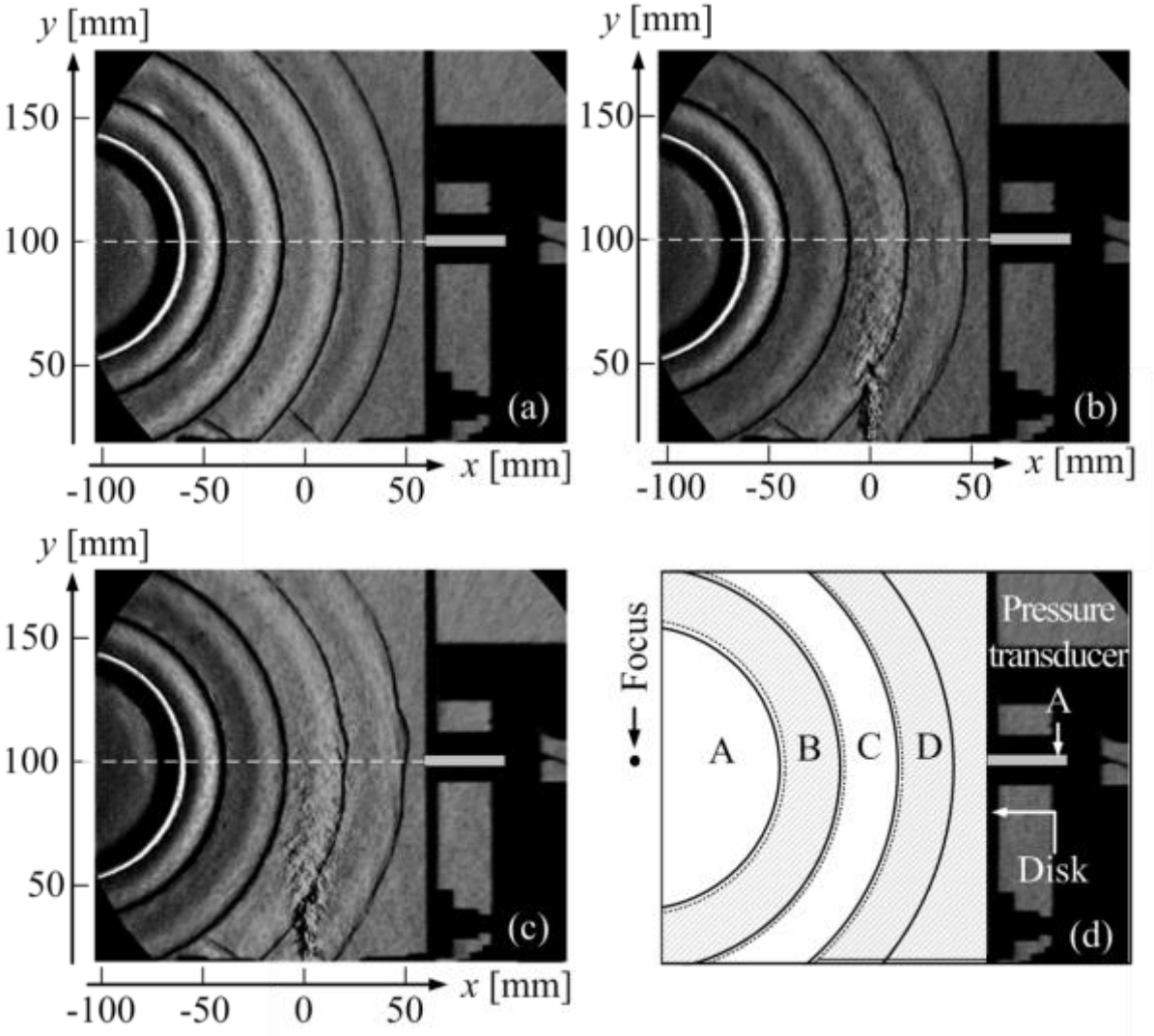

Figure 2 - 6 Sequential visualization images corresponding to Fig. 2 - 5 ; (a) without slit jet, (b) with slit jet (strong case), (c) with slit jet (weak case) and (d) region of instants (dashed line ; boundary, solid line ; shock wave), A; differential schlieren image between t = 96μs and t = 40μs, B; differential schlieren image between t = 176μs and t = 96μs, C; differential schlieren image between t = 256μs and t = 176μs, D; differential schlieren image between t = 336μs and t = 256μs.

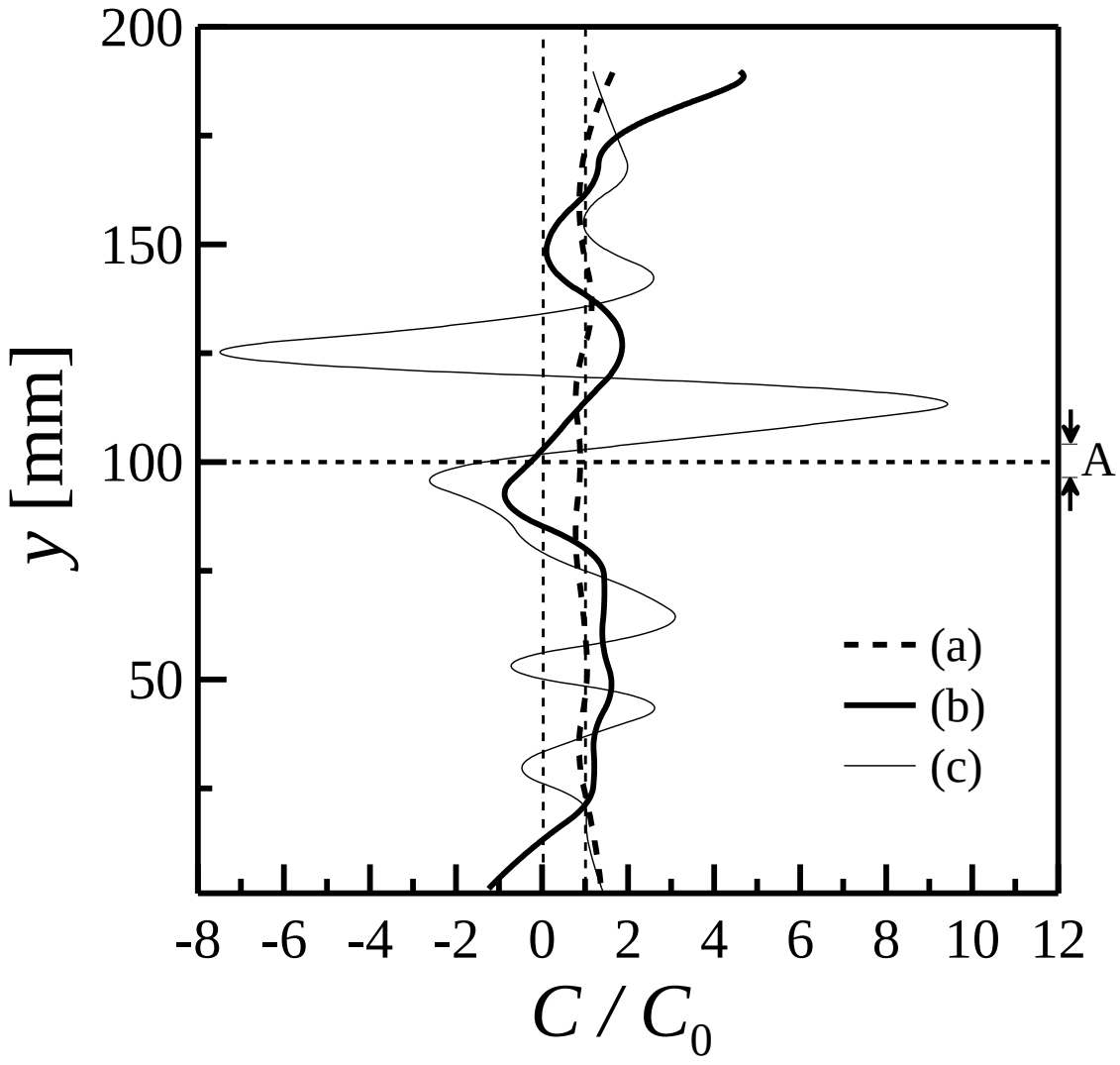

Figure 2 - 7 Shock wave curvature distributions the along *y*-axis at *t* = 336 μs ; (a) without slit jet (Fig. 2-5a), (b) strong case (Fig. 2-5b) and (c) weak case (Fig. 2-5c), The regime marked by the arrows on the right side of the graph indicates the location of the pressure transducer A on the disk surface

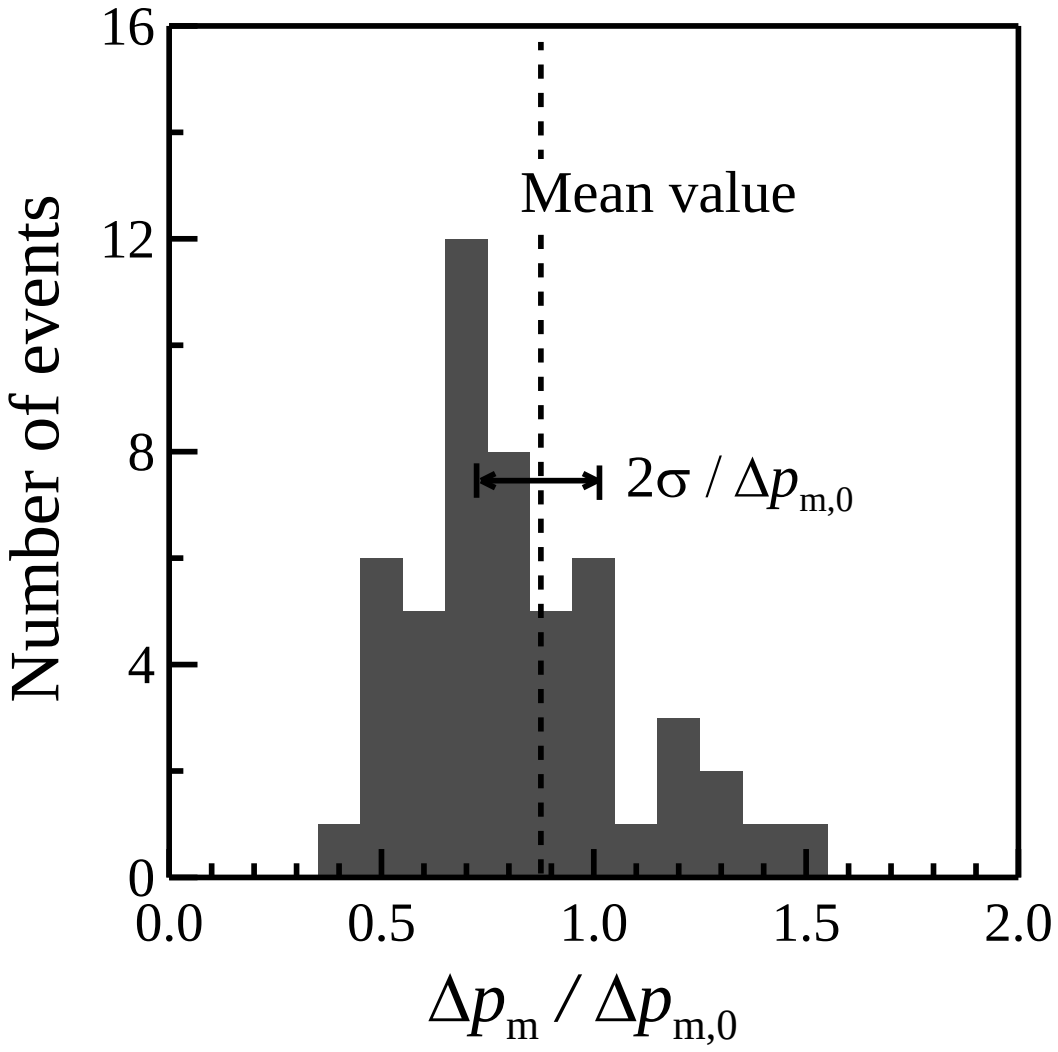

Figure 2 - 8 Histogram of peak overpressure values over 50 operations with slit jet

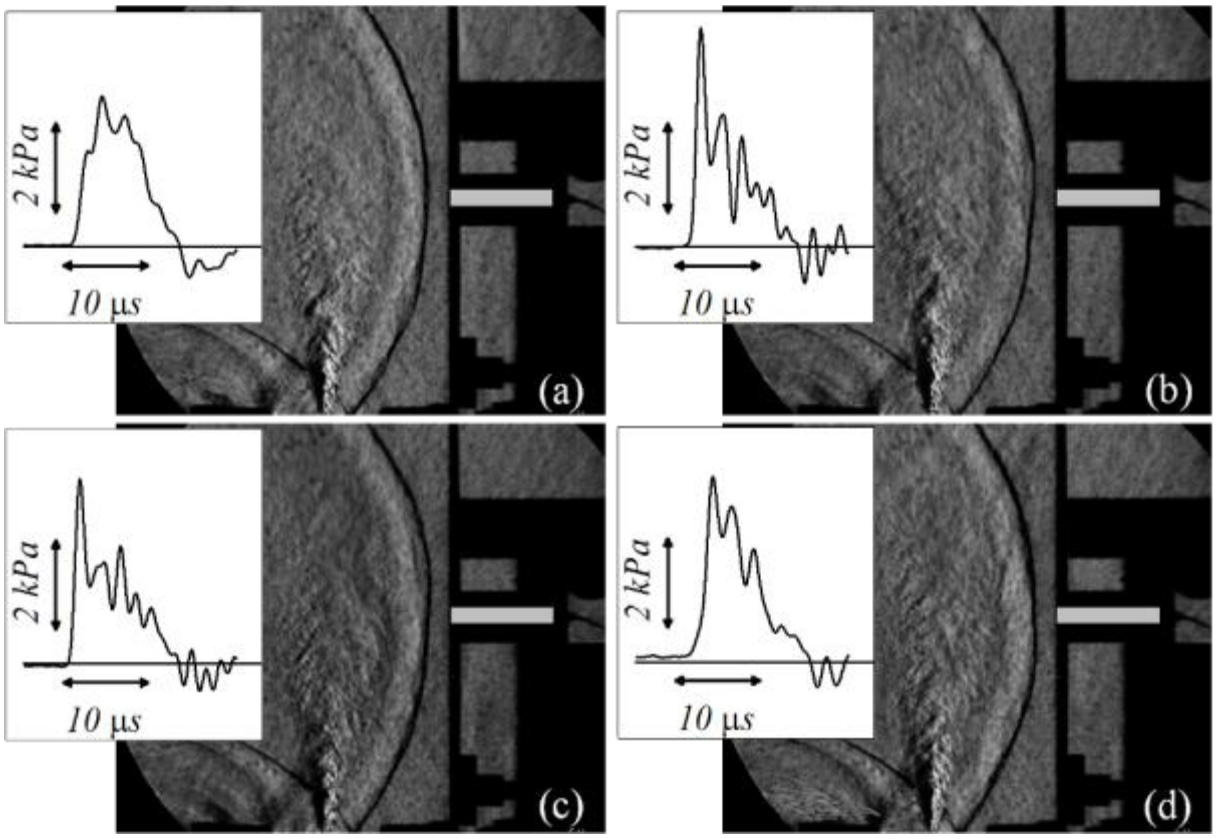

Figure 2 - 9 Δ*p* histories and corresponding shock wave configurations at *t* = 336 μs, strong cases

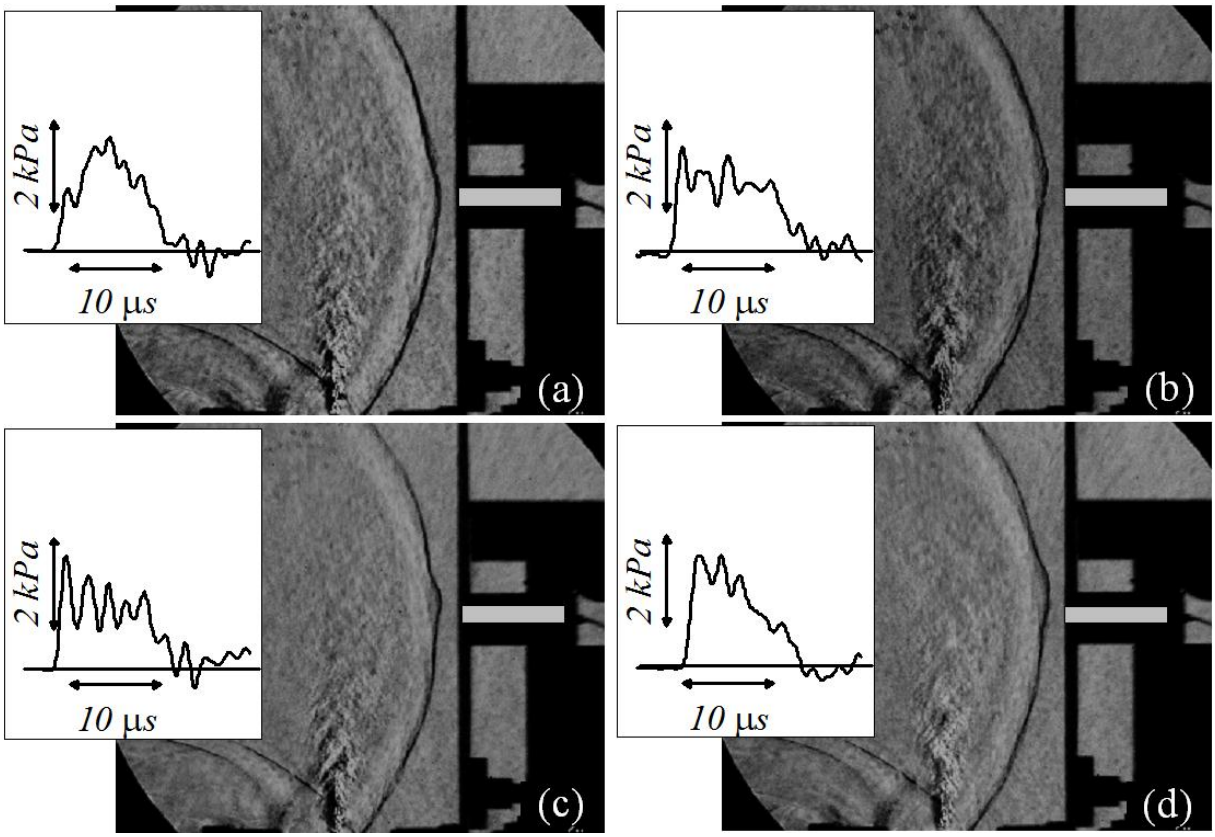

Figure 2 - 10 Δ*p* histories and corresponding shock wave configurations at *t* = 336 μs, weak cases

Chapter 3. Wave Drag Reduction Performance over a Blunt Body due to Energy Depositions

Wave drag reduction performance is described over a 20-mm-dia., flat-nosed cylinder in a Mach 1.94 flow due to the laser pulse energy depositions up to 60 kHz. Interactions between the laser-induced, low-density region and the bow shock wave are diagnosed with framing Schlieren visualization, stagnation pressure measurement. Baroclinic interaction between the laser-induced low density region and the bow shock wave over the cylinder yields a vortex ring which generates counter flow along the center axis. Stagnation pressure histories are measured to better understand the pulse-to-pulse interaction at high-repetitive laser frequencies. Under constant laser pulse energy condition, drag reduction performance is evaluated with laser frequency increasing. In this case, drag reduction performance improves almost linearly, and the drag reduction scales with the repetition frequency even with strong pulse-to-pulse interactions which lead to the formation of the acting spike to the shock layer. With constant input power, power gain only depends upon the laser pulse energy.

3-1. Introduction

Aerodynamic drag force can be classified into friction and pressure drag. Friction drag is determined entirely by a state of boundary layer, and does not change greatly between subsonic and supersonic flight. However, pressure drag rapidly increases near the transonic flow due to shock wave generated by the aircraft body. Drag force due to shock wave is called wave drag. Shock waves have been a detriment for the development of supersonic aircrafts, which have to overcome high wave drag and surface heating from additional friction. The design for high-speed aircraft tends to choose slender shapes to reduce the drag and cooling requirements. Although this profile is adequate for fighter planes and missiles, it becomes engineering tradeoff between volumetric and fuel consumption efficiencies. In particular, this tradeoff significantly increases at the operating condition of commercial supersonic aircraft, which is preferred to be wide-body capable of carrying hundreds of people.

So far, wave drag reduction in supersonic vehicles by using structural method which involves attaching a physical spike on the body nose had been studied.[Bogdonoff, S. M. et al. (1959); Maull, D. J. (1960)]. The spike forms a conical shock wave that changes the flow direction outward, significantly reducing the drag of the body. However, it was reported that the spike has to endure a large heat flux at the apex, as well as the pitching moment generated in the flight with a finite angle of attack. Since structure change of flight body for drag reduction reaches the limit, possibility of energy deposition technique was proposed to modify further aerodynamic performance.

In the past decade, advanced technology using energy deposition, which is produced by laser beam, micro wave or electric spark has been suggested actively to attempt the flow control. The energy deposition technique is applied mainly in fluid engineering filed such as a modification of shock structure, active control of boundary layer, lift enhancement and wave drag reduction.

Of these local flow control techniques using energy deposition, this study is contributed to reduce the wave drag of supersonic flight. The intensive plasma generated by laser beam focusing is useful to control the supersonic flow field. When the laser energy is deposited into the oblique shock wave, blast waves and residual hot-spot interacts with bow shock wave in front of supersonic flight. Thereafter, plasma is transmitted to shock wave, and vortex is generated by well known baroclinic effects. This energy deposition technique has received much attention recently, and related investigations have been much conducted.

Many researchers have been investigated on the wave drag reduction by using energy deposition. Knight(2008) characterizes the energy deposition scheme by using a deposited energy, pulse duration and pulse interval in respective dimensionless forms. If the pulse interval is long enough, flow after a pulse energy deposition is independent from previous pulses.

Several numerical studies were conducted to examine the drag reduction due to energy deposition over blunt-body. Riggins et al. (1999) investigated the drag reduction with the help of a computational fluid dynamics method using 2-D, axisymmetric Navier-Stokes equations. According to their study, drag force was reduced to value as low as 30% associated with power gain of up to 33 at Mach numbers of 6.5 and 10. Wave drag reduction by a single pulse energy

deposition was calculated in sphere model by Taguchi et al. (2007). The drag reduction was proportional to the freestream Mach number in their study.

Experimental study of a single laser pulse energy deposition was performed over a sphere in a supersonic flow with Mach number of 3.45 by Adelgen et al. (2005). The flow was visualized by Schlieren method and local pressure histories were measured using a piezoresistive pressure transducer that was recess mounted in the sphere model. An energy was deposited using an Nd:YAG laser pulse (wave length; 532nm, pulse duration; 10 ns, pulse energy; 12 to 300mJ). Kandala and Candler (2004) and Zheltovodov et al. (2007) conducted numerical simulation of Adelgen et al.'s experiment, thereby reproducing basic characteristics of the pressure modulation at the stagnation point. Sakai et al. (2008) conducted a similar experiment in an in-draft wind tunnel with Mach number of 3.0, and measured the stagnation pressure history using a flush-mounted piezoelectric pressure transducer, which was reproduced in their own numerical simulation.

Tret'yakov et al. (1996) conducted steady-state drag measurement in Mach-2 argon flow by irradiating CO_2 laser pulses at a repetition frequency of up to 100 kHz. A significant drag reduction of up to 45 % of the baseline drag was obtained. However, operation data with the efficiency of energy deposition being larger than unity was not presented.

With a blunt nose such as a sphere and flat-nose cylinder the amount of drag reduction is significant although the baseline drag, that is the one without energy deposition, is large. On the other hand, a sharp nose like a cone has a small baseline drag, yet the impact of energy depositions is small because the residence time of the modulated flow due to energy deposition is shorter. In order to obtain good trade-off between the baseline drag and the impact of energy depositions, Sakai et al. (2009) proposed a truncated cone shape with energy pulse depositions. In his numerical simulation, condition that the drag becomes smaller than that of a conical nose of the same apex angle and that the efficiency of energy deposition exceeds unity were both satisfied. This promising result strongly encourages further studies of this subject.

More recently Sasoh et al. (2010) measured the time-averaged drag reduction modulated with repetitive laser pulse energy depositions up to 10kHz. They obtained drag reduction of 3%

with energy deposition efficiency of 10. Also, valuable visualization results were presented to understand details mechanism of flowfield variation related with repetitive energy depositions.

The main objective of this chapter is accurately to investigate the drag reduction characteristics due to the energy deposition with high-repetitive laser pulses up to 60kHz. The laser path is modified to solve the refraction problem mentioned by Sasoh et al. (2010). In present experimental system, the precise deposited energy level without loss caused by optical problem. As a results, a deposited laser energy value is evaluated more precisely than the previous experimental set up and drag reduction performance is well characterized. Amount of drag reduction was obtained by 21% associated with power gain of 10 over blunt nose model. So far, visualization results and stagnation pressure variation due to energy deposition were suggested only for one or a couple of laser pulse experimentally except for numerical studies in relevant previous works. In this study, very interesting visualization results and pressure histories owing to high-repetitive laser pulses are provided experimentally.

3-2. Experimental Apparatus

In this chapter, the experimental apparatus described in order to investigate the drag reduction performance due to the repetitive-laser pulse energy depositions. As shown in Figs. 3-1 and 3-3, Experimental facility is consisted into supersonic wind tunnel, laser optic system and diagnostic system. While the supersonic wind tunnel is operating, measurement system which is included with stagnation pressure, drag force and visualization system is accomplished. Figure 3-2 shows the photo of detail test section in supersonic wind tunnel. Window diameter for visualization is 90mm.

The experimental conditions are given in Table 3-1 and 3-2. First, drag reduction performance with constant pulse energy is estimated. In this case, laser frequency is changed as shown in Table 3-1. Second, the effect of pulse energy on drag reduction performance is examined by taking the input power to be constant as given in Table 3-2.

3-2-1. Supersonic wind tunnel

Figure 3-3 shows a schematic diagram of experimental system. An in-draft wind tunnel of a design Mach number of 2.0 is connected to a vacuum chamber of an inner volume of 11.5m^3. The tunnel operation is initiated by opening the pneumatically-driven butterfly valve. The test section has an 80×80mm square cross section. The intake is made of brass, and has a 440 mm $\times$ 440 mm square inlet cross-section. Mach number of wind tunnel was estimated by Rayleigh-Pitot formula. Figure 3-4(a) shows distributions of static pressure and Pitot pressure along the *y*-axis. Note that *x* coordinate is defined with flow direction. From a pitot pressure of 73.7 kPa on the centerline and a static pressure of 13.8 kPa on the side wall measured at the model nose location, the effective test flow Mach number is evaluated from Fig. 3-4(a) to be 1.94 as shown in Fig. 3-4(b). Here, Rayleigh-Pitot formula is defined by,

$$\frac{p_{pitot}}{p_s} = \left(1 + \frac{\gamma-1}{2} M^2\right)^{\frac{\gamma}{\gamma-1}} \tag{3-1}$$

In supersonic flow a bowed shock wave appears in front of the Pitot probe being nearly normal upstream of the probe tip and thus the compression takes place in two steps. First non-isentropic compression in the normal shock and further isentropic compression. The relation between measured pressure values and the local Mach number are given for supersonic flow by the Rayleigh-Pitot formula.

Downstream of the test section, the flow passage is enlarged so that instruments can fit to the limited test section volume. In our experiments, diameter of the cylindrical model, *d*, is 20 mm. A laser beam is focused ahead of the model on the center axis at a separation distance of *l*. In the following experiments, *l* is set to 2.0*d*; around that value it was confirmed in preliminary experiments that the sensitivity of drag reduction characteristics to *l* was weak.

3-2-2. Laser optic system

A highly-repetitive, Nd:YLF (Neodymium: Yttrium Lithium Fluoride) laser (wavelength; 1047nm, pulse duration; 10ns, repetition frequency; 10 kHz max., average power; 85 W max.), see Fig. 3-5, is used for energy depositions with a repetition frequency of up to 10kHz. The output laser beam with a 5 mm × 5 mm square cross-section is reflected against three 45-degree reflection mirrors for 1-μm wavelength light before the wind tunnel. As seen in Fig. 3-6, another laser of a higher repetition frequency yet with a smaller pulse energy, Nd:YVO_4 laser (wavelength; 1064nm, pulse duration; 10ns, repetition frequency; 100 kHz max., average power; 400 W max.) was also used to a repetition frequency of up to 60 kHz. For Nd:YVO_4 laser, rectangular size of laser beam is a 6 mm × 6 mm. Energy charts of Nd:YLF and Nd:YVO_4 are illustrated in Fig. 3-7 and 3-8, respectively. In these charts, energy per laser pulse and input power can be found.

Laser optic system is consisted of assembled lenses, two mirrors and BK-7 window as shown in Fig. 3-9. The size of coherent laser beam is expanded up to approximately 2 times with a pair of concave and convex lens to enhance the efficiency of laser beam breakdown. Expanded laser beam by concave lens with focal length of -30 mm turns into parallel beam through convex lens with focal length of 60 mm. this expanded laser beam is reflected by mirrors. And then laser beam is focused by a convex lens with a focal length of 60 mm which is installed right before a wind tunnel window, as side-on laser. The window is made of BK-7, has a diameter, thickness of 90mm and 15mm, respectively. Transmittance of BK-7 window presents in Fig. 3-10. This data was obtained from manufacturer. In the range from wavelength of Nd:YLF laser to one of $Nd:YVO_4$, transmittance is more than 99%. The time-averaged laser power is measured using a power meter (1000W-SH-V2 ROHS, Ophir) behind the window without the focal lens. The transmittance of the focal lens is measured separately, and is taken into account in evaluating an effectively-sent power. In the followings, the value of laser pulse energy effectively sent on to the focal spot, which is about 76% of an output energy from a laser device.

3-2-3. Stagnation pressure measurement

Stagnation pressure is measured by flush-mounted piezoelectric pressure transducer (PCB Piezoelectronics, Inc. Model-H112A21, rise time of 1μs, natural frequency of 250 kHz) on the head of cylinder model. A diameter of sensing part is 5.56mm. Sampling ratio of pressure measurement is 10MS/s. The output signals of the load cell, the pressure in the sub-chamber and stagnation pressure are recorded in a digital storage scope (DL750，Yokogawa co.).

3-2-4. Drag force measurement

In this study, a 20-mm-dia. cylinder model is used to evaluate the drag on its forehead. Figure 3-11 shows the cylinder model and drag measurement system [Sasoh, A. et al. (2010)].

The model is made of brass and is held in the 35mm-outer-dia. brass housing. The clearance between the cylinder model and the housing with two O-rings is set to the order of 500μm. The aft-head of the cylinder model is set in a room, which is pneumatically isolated from the wind tunnel test section and connected to a sub-chamber (inner volume; 0.018 m^3) outside of the wind tunnel. The pressure in the sub-chamber, p_{sub}, is regulated and monitored using a semiconductor pressure transducer (DG-920, Tokyo Aircraft Instrument co.). The cylinder model is also backed by a load cell (MR-50N-0418, Showa Measurement Instrument co., maximum load 50 N) in the room to measure the force balance over it. For further details of the force balance in the drag measurement, reader should refer to Sasoh et al. (2010).

Figure 3-12 and 3-13 shows an example of result of force calibration. The calibration is conducted under a quiescent atmospheric air. First of all, the sub is evacuated through the vacuum pump with only Valve 1 being open. When the sub-chamber pressure, p_{sub}, becomes below 10kPa, Valve 1 is closed. Then, Valve 2 is rapidly opened within 0.1 sec. This motion yields the signals at 'a' in Fig. 3-12; the load cell experiences the first load of about 27.5 N, the pressure balance. To reduce the sub-chamber pressure as a step motion, Valve 3 which is connected between the sub-chamber and secondary sub-chamber which has an inner volume of 0.0023 m^3 is rapidly opened. Before opening Valve 3, the initial pressure inside secondary sub-chamber equal to ambient pressure. Thereafter, pressure of sub-chamber keeps balance with one of secondary sub-chamber. This step is indicated by 'b'. After the end of first step, point a, Valve 3 is closed, and then secondary sub-chamber pressure recovers with opening Valve 4. To go to point c, Valve 3 is opened again after closing Valve 4. As a result of these Valves operating, sub-chamber pressure reaches to another equilibrium state. With same processes, pressure of housing system is reduced step by step in order to estimate the dynamic response of drag measurement system. Last calibration step is indicated by point d. Thereafter, sub-chamber pressure has ambient pressure (point e) with opening the valves 3 and 4. As shown in Fig. 3-13, the force to the load cell restored to the respective constant values in the successive three unsteady lading cycles. It was estimated that resolution of force balance system is about 0.015 N and dynamic response time is 0.09sec. The pressure balance shows fairly good linearity from point c to point e. In experiments of this study, drag force is estimated to be of approximately 21N, and then reduced due to the energy, depositions by up to about 20 %; the force balance is within the linear range shown in Fig. 3-13. In order to examine the above-mentioned drag measurement

performance, we conduct in-situ calibration before and after a series of experiments of each day. The output signals of the load cell, the pressure in the sub-chamber and stagnation pressure are recorded in a digital storage scope (DL750，Yokogawa co.) with a sampling rate of 20kS/s.

3-2-5. Flow Visualization

Framing schlieren visualization is done using a high-speed framing camera (HPV-1, Shimadzu Co., 312 × 260 pixcels, 106 frame/s max., 100 frames). A xenon flush lamp (SA-200F，Nissin Electronic co., duration; 2ms)) is used as the light source. A pair of 300-mm-dia. concave mirrors (focal lengths; 1 m and 2 m) are used to obtain and image a collimated beam in schlieren setup.

3-2-6. Procedure of Data Acquisition

Figure 3-14 shows the procedure to obtain the measurement date. After starting the wind tunnel, static pressure obtained from static hole which is installed at upper wall of wind tunnel is decreased. This static pressure is measured by digital pressure transducer 1. If static pressure decreases by certain value, preliminary trigger signal is sent to the delay generator. The main trigger signals are arranged to control several devices such as HPV-1 high speed camera, flash ramp and oscilloscopes. And also, irradiation time of laser beam is determined via the delay generator. However, to operate the laser device, function generator is used with adjusting of laser pulse repetition frequency.

Stagnation pressure measured by PCB pressure transducer is recorded via oscilloscope 1 with high speed sampling rate. Drag force signal which is obtained by force balance system including load cell is recorded to oscilloscope 2 after amplifying

3-3. Interaction between a Laser-Heated Gas and Bow Shock Layer

In the steady-state supersonic flow without energy depositions, a standing bow shock wave is formed over the cylindrical model with a stand-off distance of about 0.45 *d.* Since the location of the laser beam focus, *l*, is set to 2.0 *d*, a laser pulse heats the air sufficiently upstream of the bow shock wave. Figure 3-15 shows framing Schlieren images obtained with laser pulse energy, *E*, of 13.2mJ/pulse and a laser pulse repetition frequency, *f*, of 2kHz. Corresponding to Fig. 3-15, stagnation pressure history is presented in Fig. 3-16. The time-dependent stagnation pressure, p_{st}, is normalized by the steady-state value without laser pulse irradiation, $p_{st,0}$. Here, Δt is originated in the instant of a laser pulse irradiation, not the first one but after about 600th irradiations. A trigger signal to control the high speed camera is taken prior to the laser pulse irradiation. After the laser pulse is irradiated, the air is locally heated through optical breakdown. Since the laser pulse period is of the order of 10 ns, the heating is done in an almost-constant volume. This heated air with a higher pressure than the surroundings expands, under the present condition, almost spherically. In this way, a low-density gas is generated upstream of the bow shock wave, then moved downstream with the test flow velocity. Due to the expansion, a laser-induced blast wave is propagated around the laser-heated gas. At Δt = 60μs, the laser-induced blast wave already arrived the model body, whereas the laser-heated gas does not arrive even at the bow shock wave. Blast wave induced stagnation pressure is confirmed as the first pressure rise of (A) in Fig. 3-16. Then, the gas near the body undergoes, short expansion (B) followed by re-compression to induce a secondary shock wave. At Δt = 72μs, the laser-heated gas is entering the shock layer, and the bow shock wave extrudes upstream due to the 'lens effect.' [Knight, D.(2008); Sasoh, A. et al. (2006)]. After the laser-heated gas completely enters the shock layer, a vortex ring is formed at Δt = 92μs. Secondary peak pressure is occurred by interaction between laser-heated gas and bow shock wave. When the low density regime transmits through the bow shock layer, secondary shock wave is generated with its compression. Therefore, secondary shock wave impinges on model at (B). This behavior is well-known from investigations of the blast wave propagation and reflection. Moving downstream, along axi-symmetric stream lines,

the diameter of vortex ring increases, and reaching the full diameter of the model nose. In this case, stagnation pressure is decreased by $p_{st}/p_{st,0}$=0.9 due to baroclinical vortex ring. Drag reduction due to the energy deposition is realized as a result of this pressure ratio drop between (C) and (D). At Δt = 240μs and thereafter, the laser-heated gas leaves past the nose. At Δt = 376μs, the flow has effectively restored to the initial steady state.

3-4. Shock Layer Interaction with Trains of Heated Gases

The histories of $p_{st}/p_{st,0}$ with f are shown in Fig. 3-17. With f=1kHz, the pressure modulation as seen in Fig. 3-16 is repeated in an almost independent manner; the pressure ratio restores to unity after each laser pulse irradiation. However, with higher f, the baseline value does not go back to unity. With f=10kHz, pressure fluctuations caused by laser pulses interaction is significantly affects to pressure history. In this case, vortex ring generated by another pulse influence the pressure field in front of the model before former vortex ring induced pressure disturbance is not perfectly recovered. These pressure characteristics make new steady flow field after laser irradiation and time-averaged stagnation pressure is decreased by around $p_{st}/p_{st,0}$ = 0.93 with standard deviation, σ, of about 5%. Time-averaged stagnation pressure is decreased more significantly as repetitive frequency becomes higher. It can be observed that the stagnation pressure ratio has 0.7 for f=50kHz. With high-repetitive laser pulse, next vortex is arrived to the distorted shock before shock shape is restored to the original form. Therefore, apex angle of shock layer becomes smaller with time, and transition of shock layer is maintained during short time.

Figure 3-18 and 3-19 show the variations of time-averaged stagnation pressure variations and RMS (Root Mean Square) value of stagnation pressure modulations caused by laser pulses. For low repetitive laser frequency, it was shown that fluctuation of stagnation pressure is recovered completely because each laser pulses affect independently to the stagnation pressure. In this case, drag reduction can be realized only by the pressure drop, while the vortex ring stays in front of the body. While the laser frequency is increased, time-averaged stagnation pressure is almost linearly decreased, and that is decreased up to approximately 30% at f=50kHz. When the laser pulses of low frequency are irradiated, the modulation of stagnation pressure has been influenced separately on the laser pulse. Since interval between pulses is long, the stagnation pressure does not modulate for a long time after recovering of stagnation pressure as seen in Fig. 3-17. RMS value of stagnation pressure becomes significant with laser frequency. However, it has come to its peak at f = 25 kHz. Thereafter, pressure modulations become weak. This implies

that the flow field influenced by the vortex rings becomes stable at high repetitive energy depositions.

Schlieren images at different repetitive laser frequencies are compared in Fig. 3-20. Apex anlge of distorted shock shape due to the interaction with laser-heated gas becomes smaller with frequency increasing. In Fig. 3-20(a), a couple of vortex ring can be found between bow shock wave and blunt body model, and vortex ring moves downstream axisymmetrically. When laser pulses are irradiated at f=25 kHz, three vortex rings appear obviously in front of model. In this case, the curvature of the shock layer is smaller than that of f=10 kHz. Over f=40 kHz, the vortex ring is not be observed because vortex rings are broken rapidly, since vortices leads to the flow instability in front of the model. However, the shock layer which is composed of several vortices has cone shape like a virtual spike, and its effective apex angle decreases with increasing frequency.

3-5. Drag Reduction Performance

3-5-1 Drag reduction performance with constant pulse energy

Figure 3-21 shows the histories of the measured drag force normalized by the baseline value, D_0 obtained without laser pulse irradiation. Laser pulses are irradiated during one second. From 1kHz to 10kHz, energy deposition in flow field is accomplished by using Nd:LYF laser, and input laser energy per pulse is kept at 6.6mJ regardless of the frequency. Nd:YVO4 laser with E=6.2mJ/pulse is used to deposit the energy over f=10kHz. Before and after the laser pulse irradiations, the drag exhibits a steady-state value with fluctuation of a root mean square (RMS) of 0.24 %. During the laser pulse irradiations, the drag is decreased in a quasi-steady-state manner. The higher f, the larger the drag reduction, ΔD, is increased. With f=50kHz, a 21% drag reduction is obtained.

Figure 3-22 presents the drag reduction characteristics with varying f. With a constant value of E, $\Delta D/D_0$ almost linearly increases with f. The coefficient in the linearity is slightly larger with the Nd:YVO_4 laser presumably due to better beam quality. If same laser energy per pulse is irradiated into the flow field, laser induced laser-heated gas of same size and strength has influence on the drag reduction. When the pulse energy of 4.6mJ is deposited to reduce the drag, same tendency on drag performance is also obtained. However, the amount of drag reduction is lowller than that of E=6.2 mJ, since weak pulse energy is irradiated into the air. Consequently, it is indicated that a higher repetitive frequency might affect linearly to drag reduction, and the amount of drag reduction can be predicted if pulse energy is known. In the experiments, drag reduction is realized by about 21% at f=50kHz and E=6.2mJ.

Figure 3-23 presents the performance of the power gain of energy deposition. The power gain is defined by,

$$\eta = \frac{saved\ power}{input\ power} = \frac{\Delta D\ U}{W} \tag{3-2}$$

, where U is freestream velocity. Although the power gain is shown approximately 8.0 at low laser frequency with E=6.2~6.7mJ, its error range is more wide comparing with one of high input power. The efficiency monotonically decreases with increasing W. Then power gain stays an almost constant value of about 7.0 in the range of 30W to 300W. It is concluded that the power gain with same pulse energy may keep at constant value independently of laser frequency.

3-5-2. Drag reduction performance with constant input power

In the previous section, drag reduction characteristics with varying only f at a constant E are presented. In this section, drag reduction characteristics with varying E at a constant laser power $W=fE$ will be presented.

Figure 3-24 shows stagnation pressure histories with a constant value of W (=26.4W). Results of four combinations of E and f are shown; Fig. 3-24(a) with the largest E and the lowest f, Fig. 3-24(d) the smallest E and the highest f. In Fig. 3-24(a), with the largest value of E (=13.2 mJ), largest decrement in the stagnation pressure is obtained. With increasing f and then decreasing E, the value and duration of the pressure decrement becomes small and short, respectively. In particular, with E = 5.3 mJ some of laser pulses fails to cause optical break down; leading to poor drag reduction performance.

Figure 3-25 summarizes the constant-power drag reduction performance. At a laser power of 19.8W, the drag reduction, $\Delta D/D_0$, has a peak value of about 2.0 % at around 2.5 kHz. Same tendency is shown in the input power=26.4W. Unfortunately, at the input power of 39.6W and 59.4W, the drag performance is just shown in low pulse energy conditions because laser facility is not allowed in wide operating range.

Power gain variations corresponding to Fig. 3-25 are shown in 3-26. The power gain increases with pulse energy since laser-heated gas size increases as pulse energy increase, and has a maximum value(=10) at E = 8.0. And then gradually decreases although more powerful pulse energy is irradiated. This is resulted that the most effective E-f combination should be demonstrated to optimize the drag reduction using energy deposition. It is better to increase the repetitive laser frequency in order to improve the efficiency of drag reduction performance at

given input power. However, the performance is not continuously improved as laser frequency increases because the deposition efficiency is diminished at low pulse energy in physical situation. In this study, threshold energy of laser pulse for breakdown is estimated about 4 mJ. It is of interest that the power gain is independent on the depositing frequency. Furthermore, the power gain due to the energy deposition is given as an only function of pulse energy.

3-6. Summary

Experimental study has been performed to investigate the drag reduction performance due to laser induced energy deposition. Steady-state drag reduction performance was measured from a force balance over the back-pressure controlled piston using a load cell installed into in-draft supersonic wind tunnel of Mach number=1.94. Repetitive laser pulses of up to 60 kHz were used to deposit the energy. Within the limited laser power capability, it has been experimentally demonstrated time-averaged drag reduction performance; 21 % drag decrease and power gain of energy deposition up to 10. It is remarkably concluded that pulse-to-pulse interaction in stagnation pressure history becomes significant with increasing the laser pulse repetition frequency (f), yet the drag reduction ($\Delta D/D_0$) scales almost linearly with f. It is estimated the combination of E-f effects to optimize the drag reduction performance over a given input power conditions. The power gain is given as a function of only laser pulse energy (E), and to increase the laser frequency is rather than pulse energy to obtain the higher drag reduction performance. In our laser optic system, the threshold pulse energy for laser beam breakdown was about 4mJ. The power gain had a peak value at E=8.0mJ.

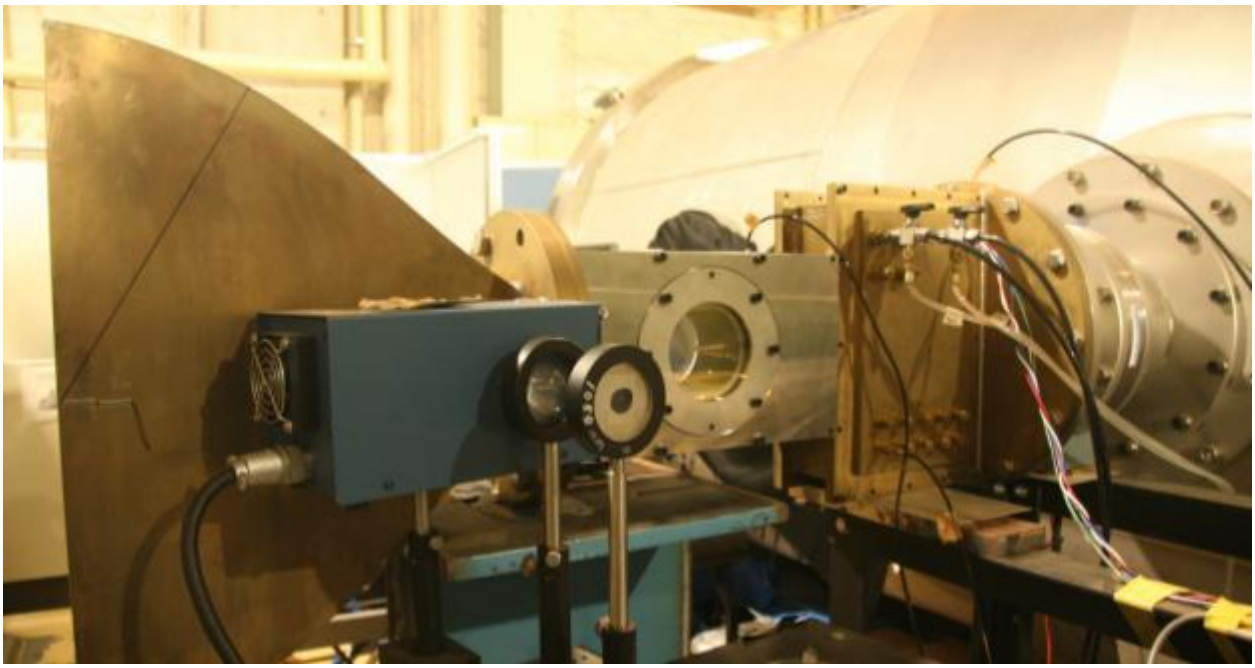

Figure 3 - 1Photo of wind tunnel

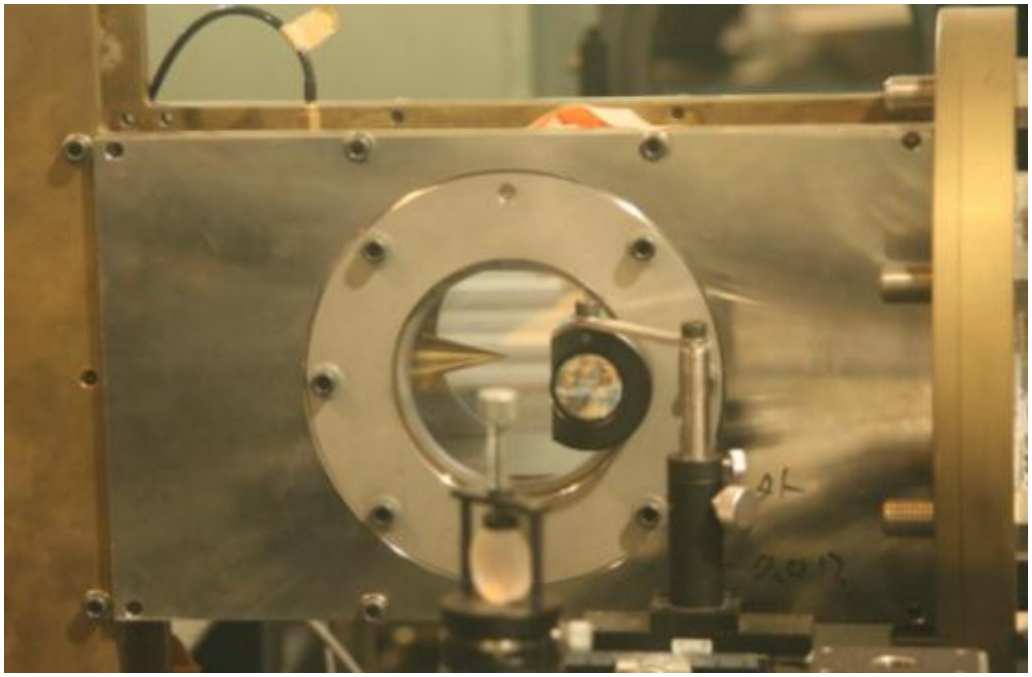

Figure 3 - 2Test section

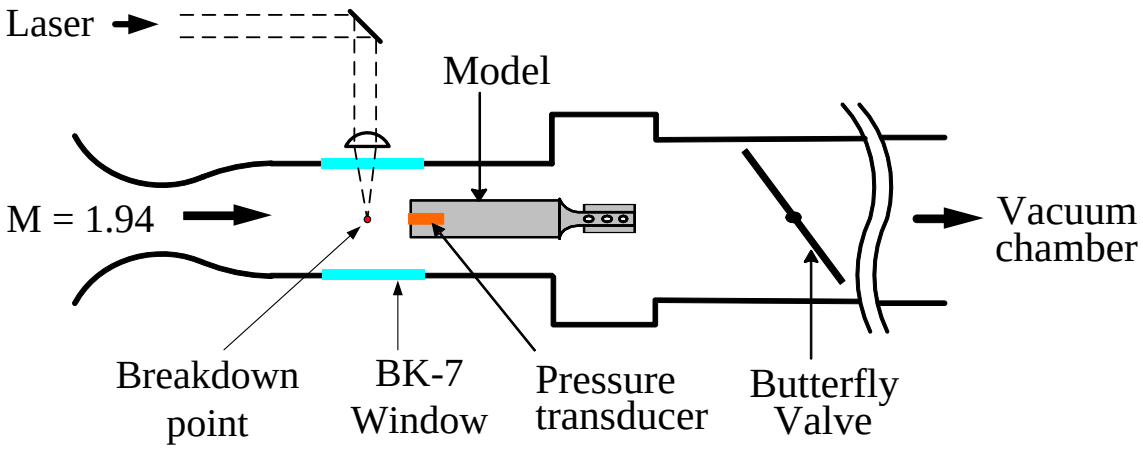

Figure 3 - 3 Schematic diagram of experimental setup

Table 3 - 1 Experimental conditions (with constant pulse energy)

Pulse energy, *E*	**Laser frequency, *f***
6.2~6.6 mJ	1~50kHz
4.6 mJ	5~60kHz

Table 3 - 2 Experimental conditions (with constant input power)

Laser input power	
19.8 ~ 59.4 W	Combinations of *E* and *f*

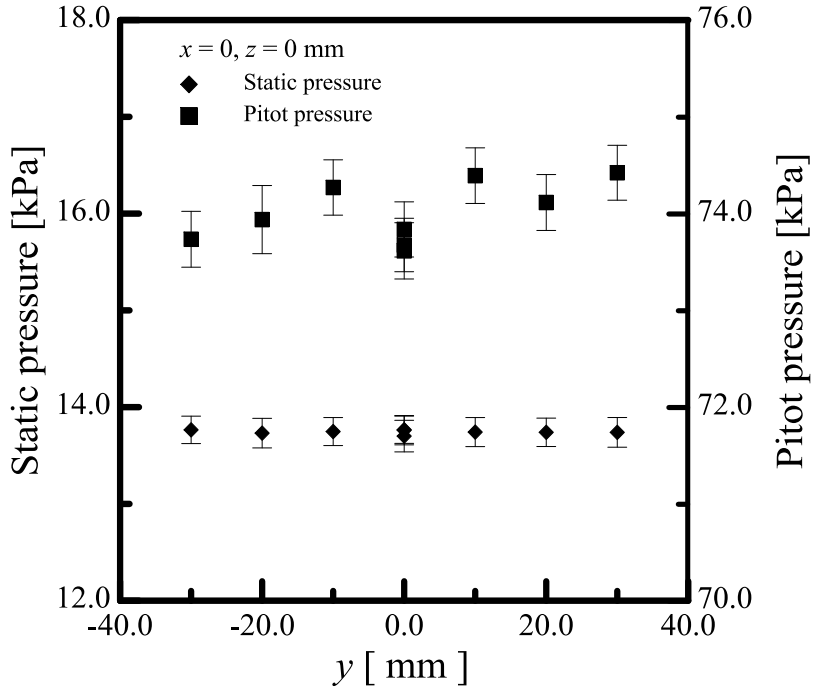

(a) Distributions of static and Pitot pressure

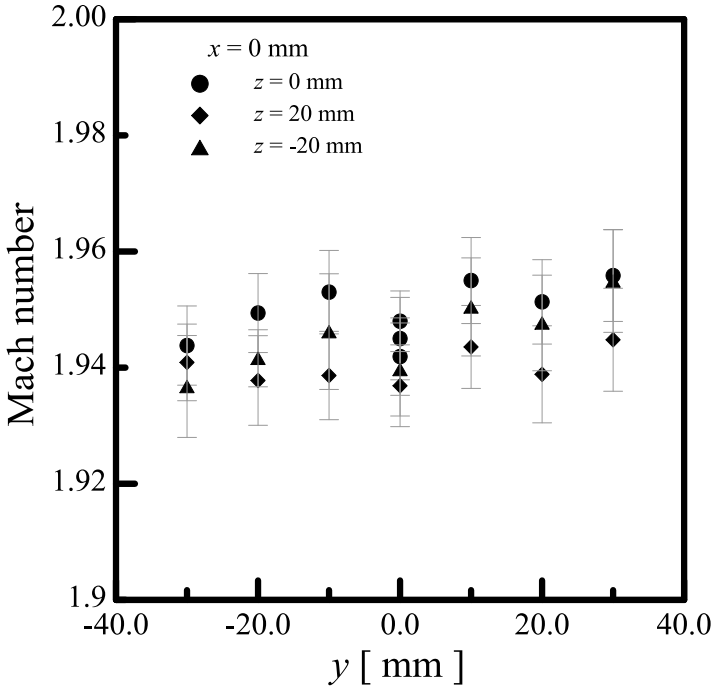

(b) Mach number distributions

Figure 3 - 4 Estimation of supersonic wind tunnel Mach number

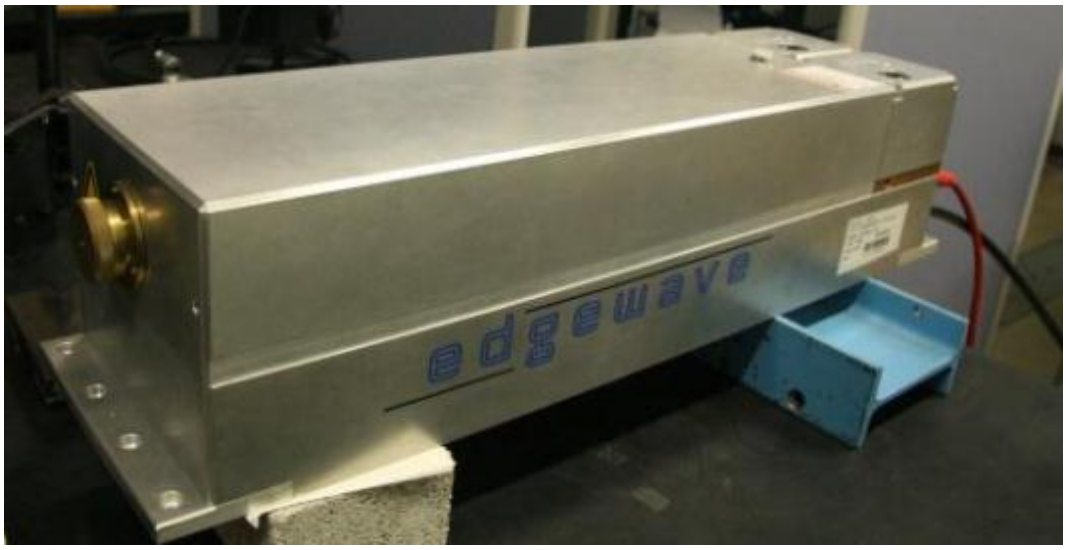

Figure 3 - 5 Photo of Nd:YLF Laser

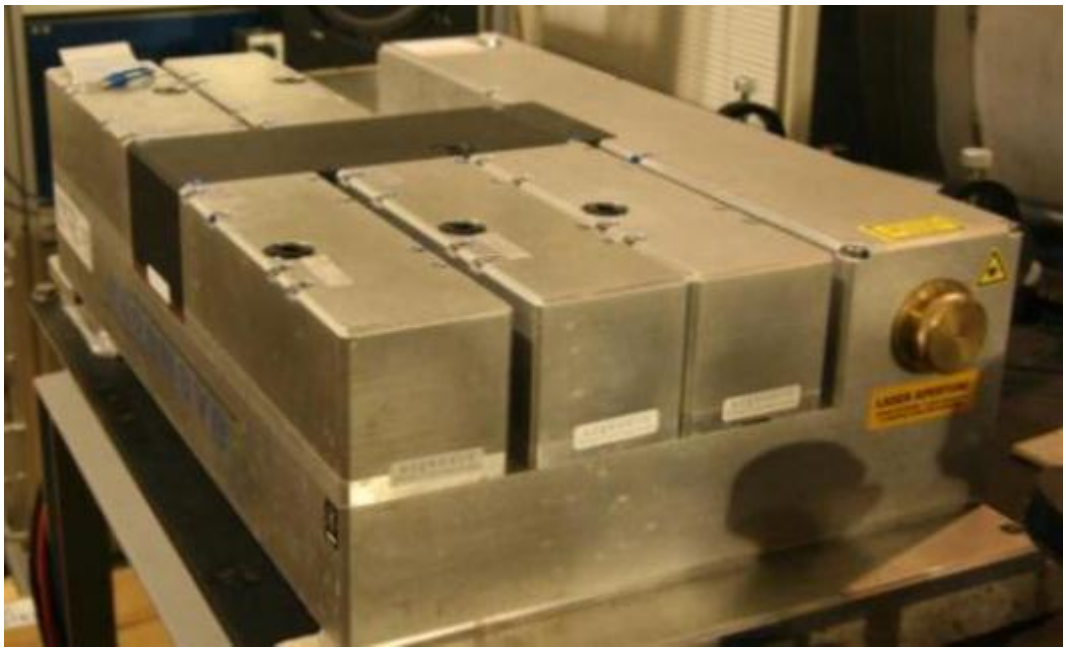

Figure 3 - 6 Photo of Nd:YVO_4 Laser

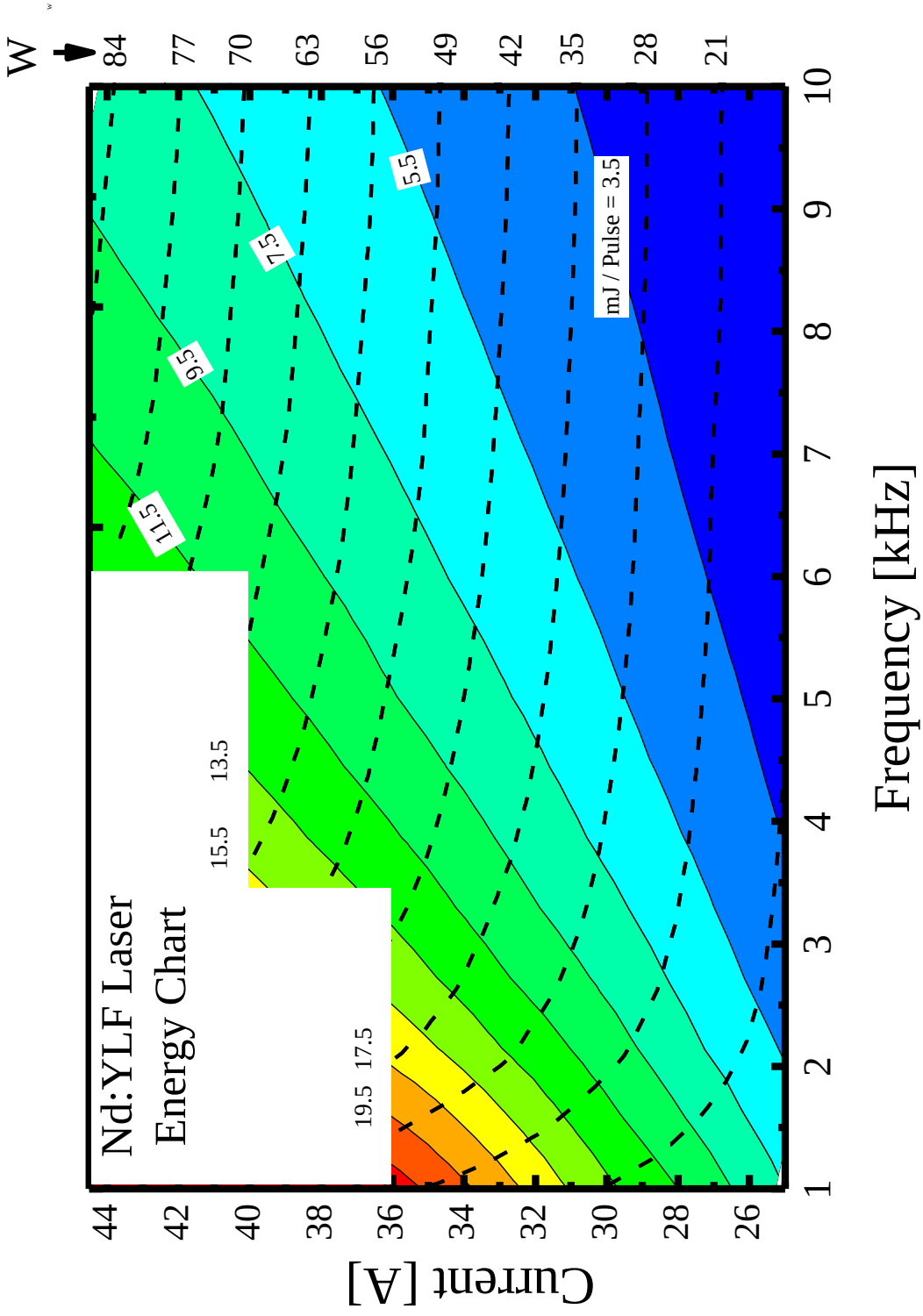

Figure 3 - 7 Energy chart for Nd:YLF laser

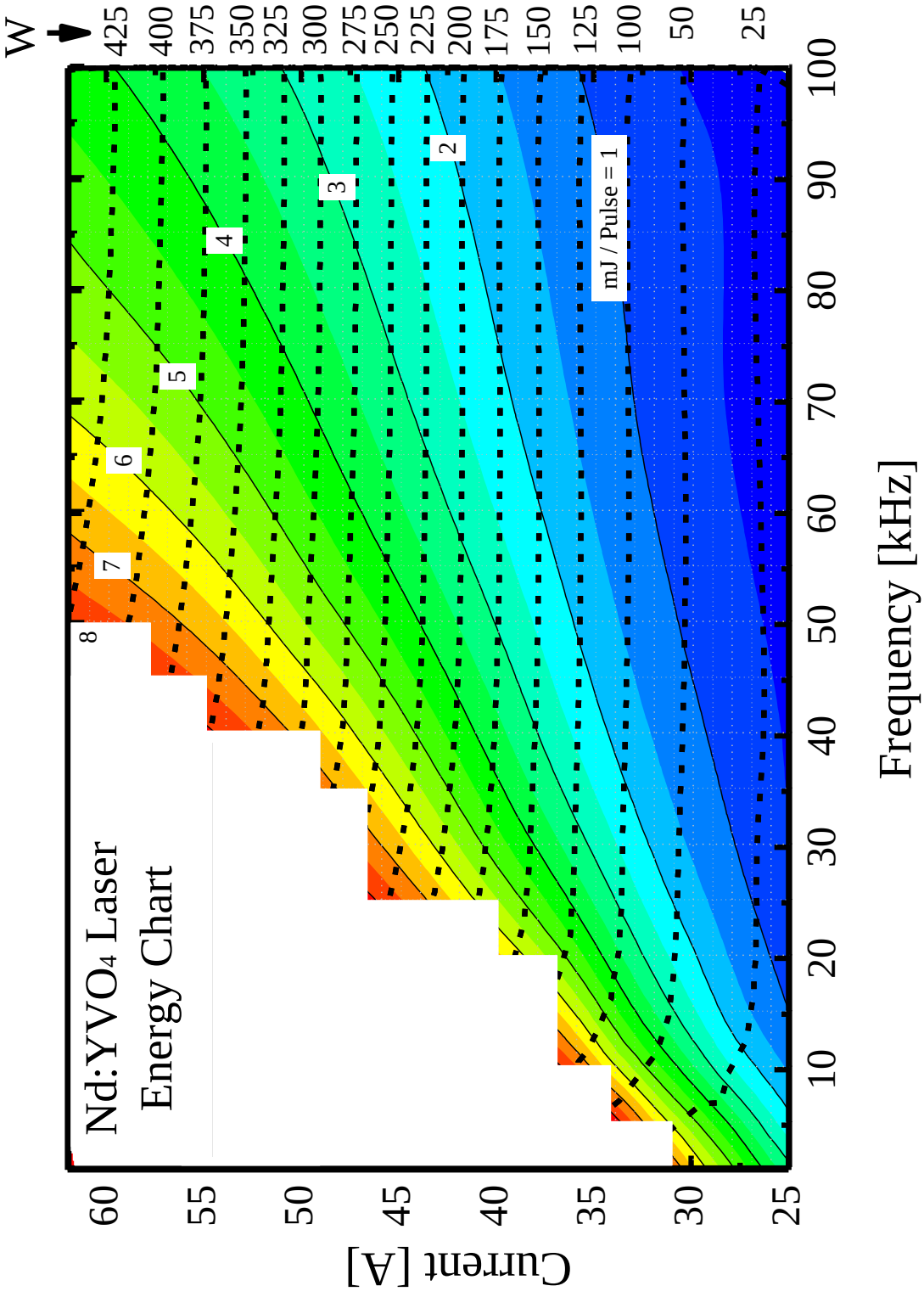

Figure 3 - 8 Energy chart for Nd:YVO_4 laser

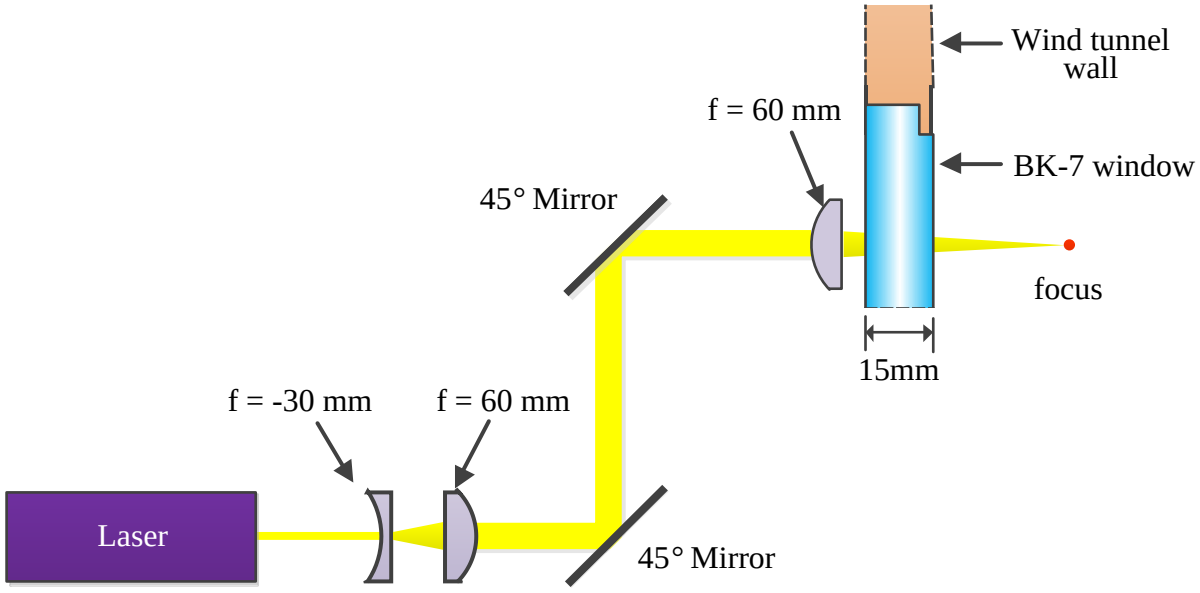

Figure 3 - 9 Laser optic system

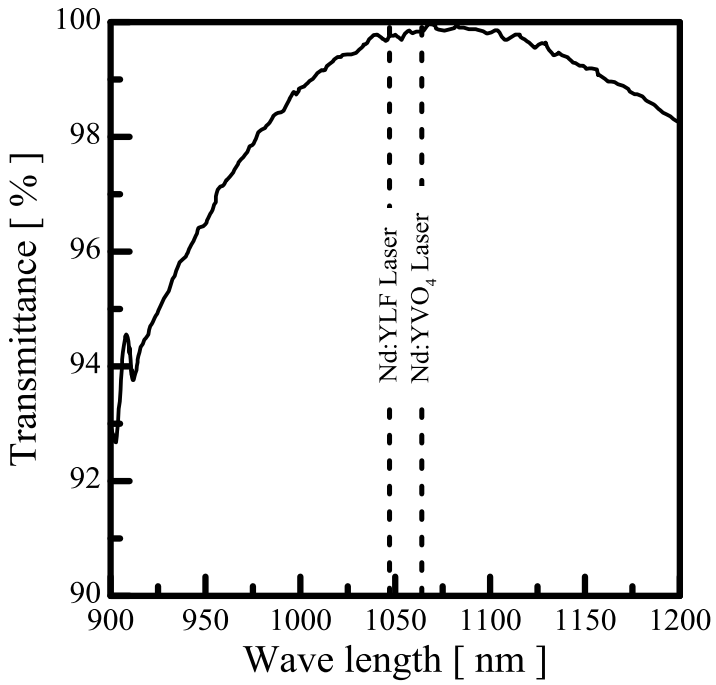

Figure 3 - 10 Transimittance of BK-7 window installed wind tunnel side

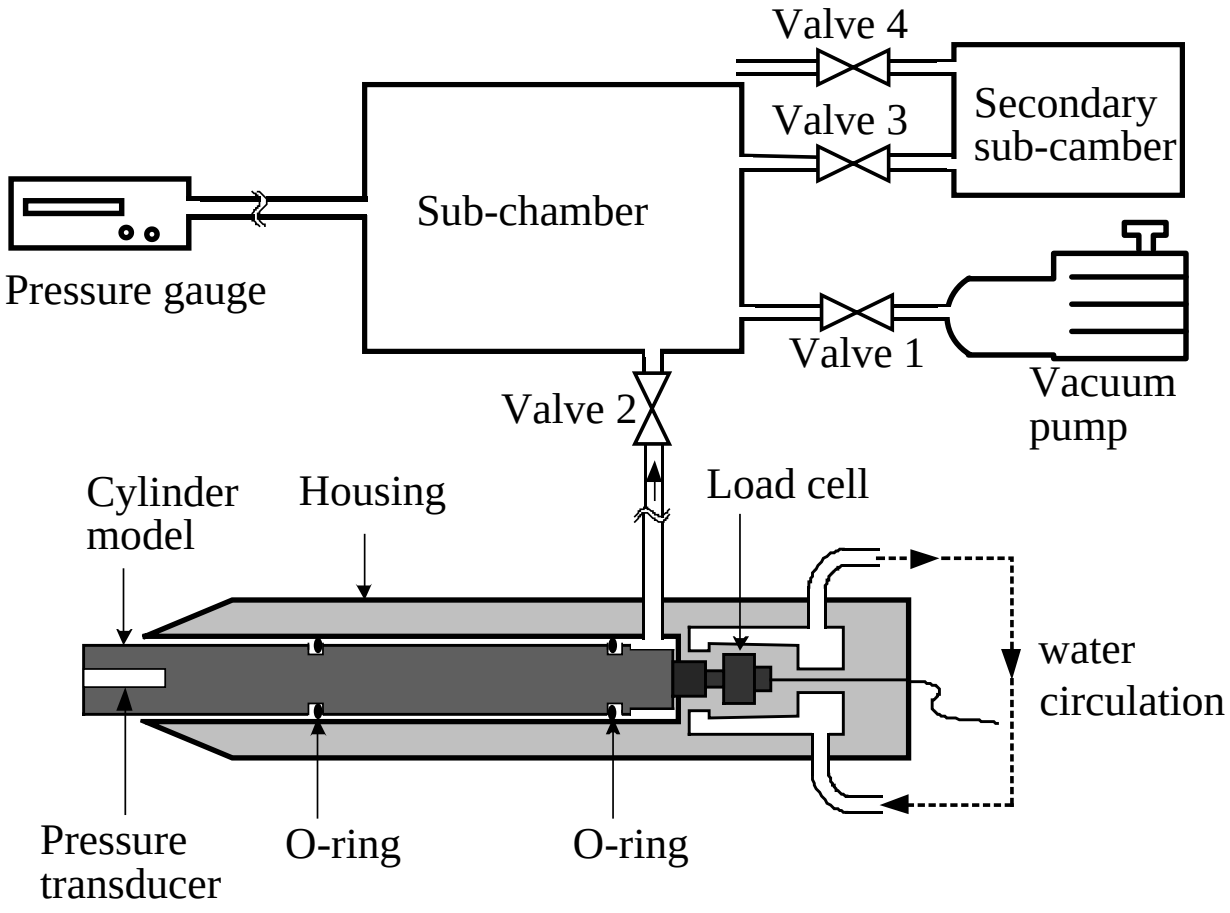

Figure 3 - 11Force measurement system using load cell

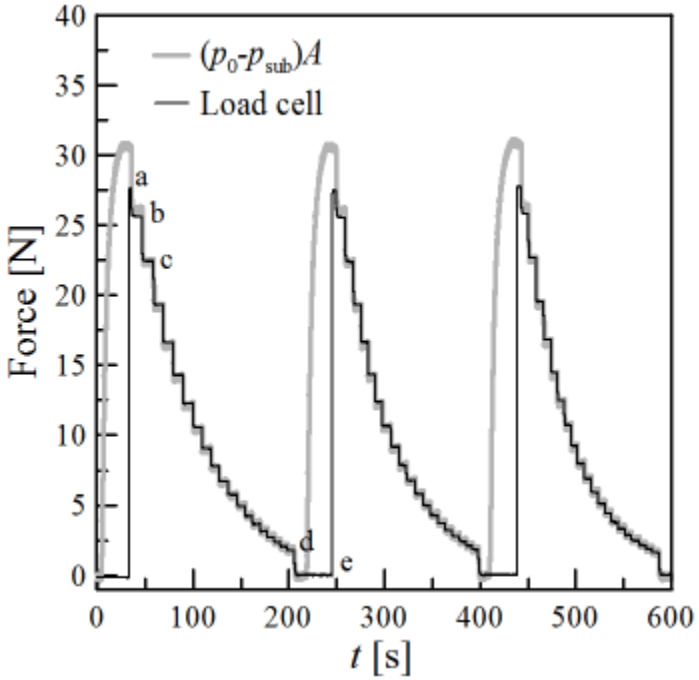

Figure 3 - 12 History of load cell signal in unsteady load response test

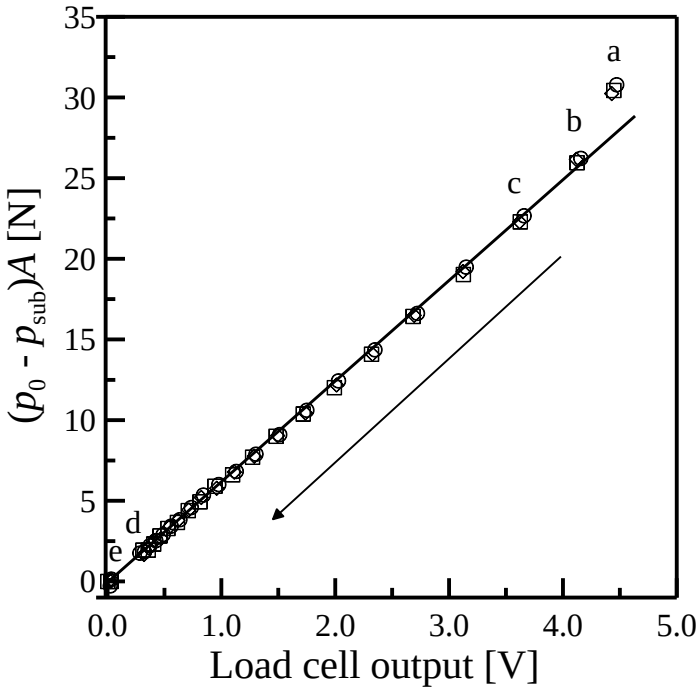

Figure 3 - 13 Calibration results of load cell

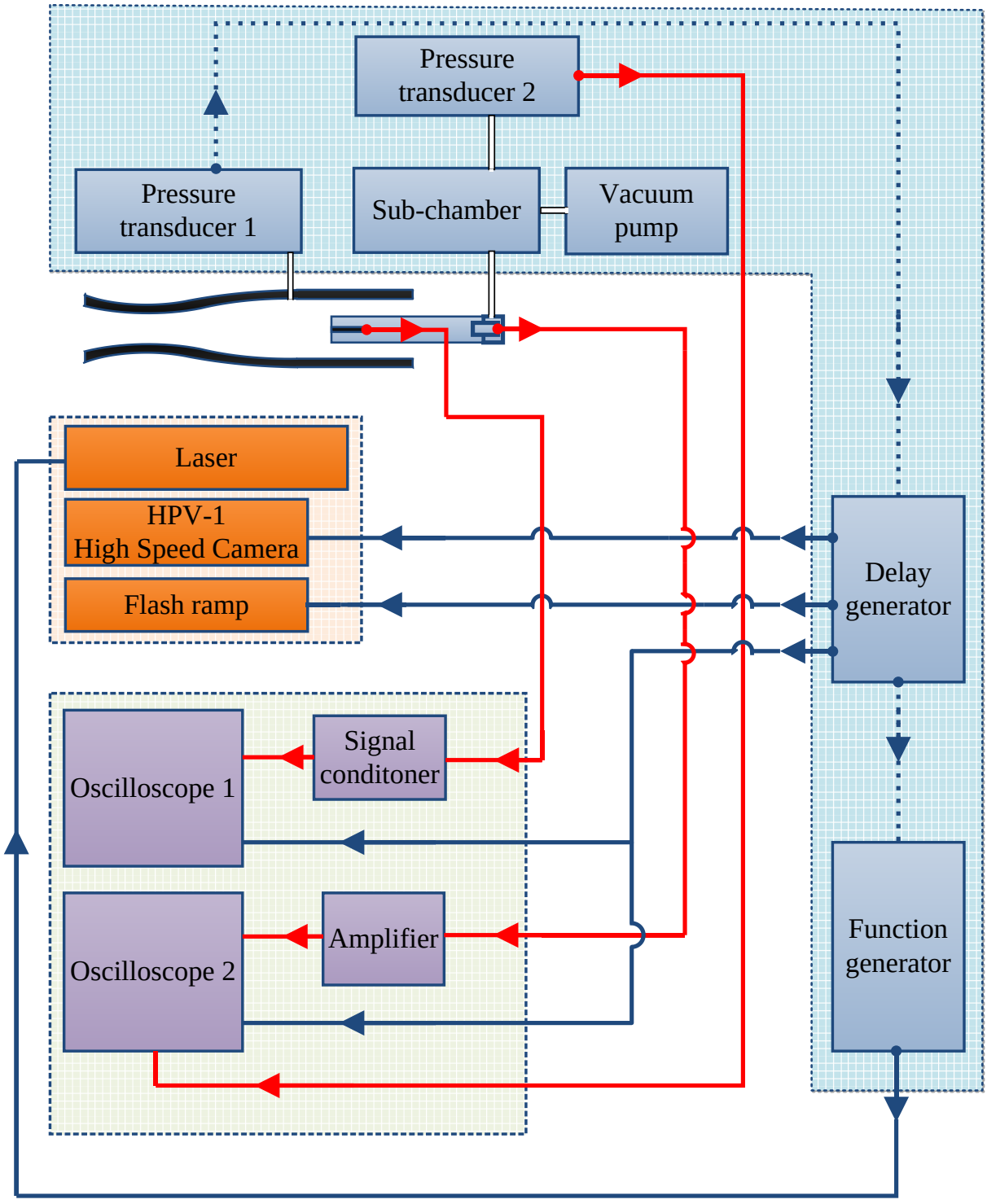

Figure 3 - 14 Data acquisition system

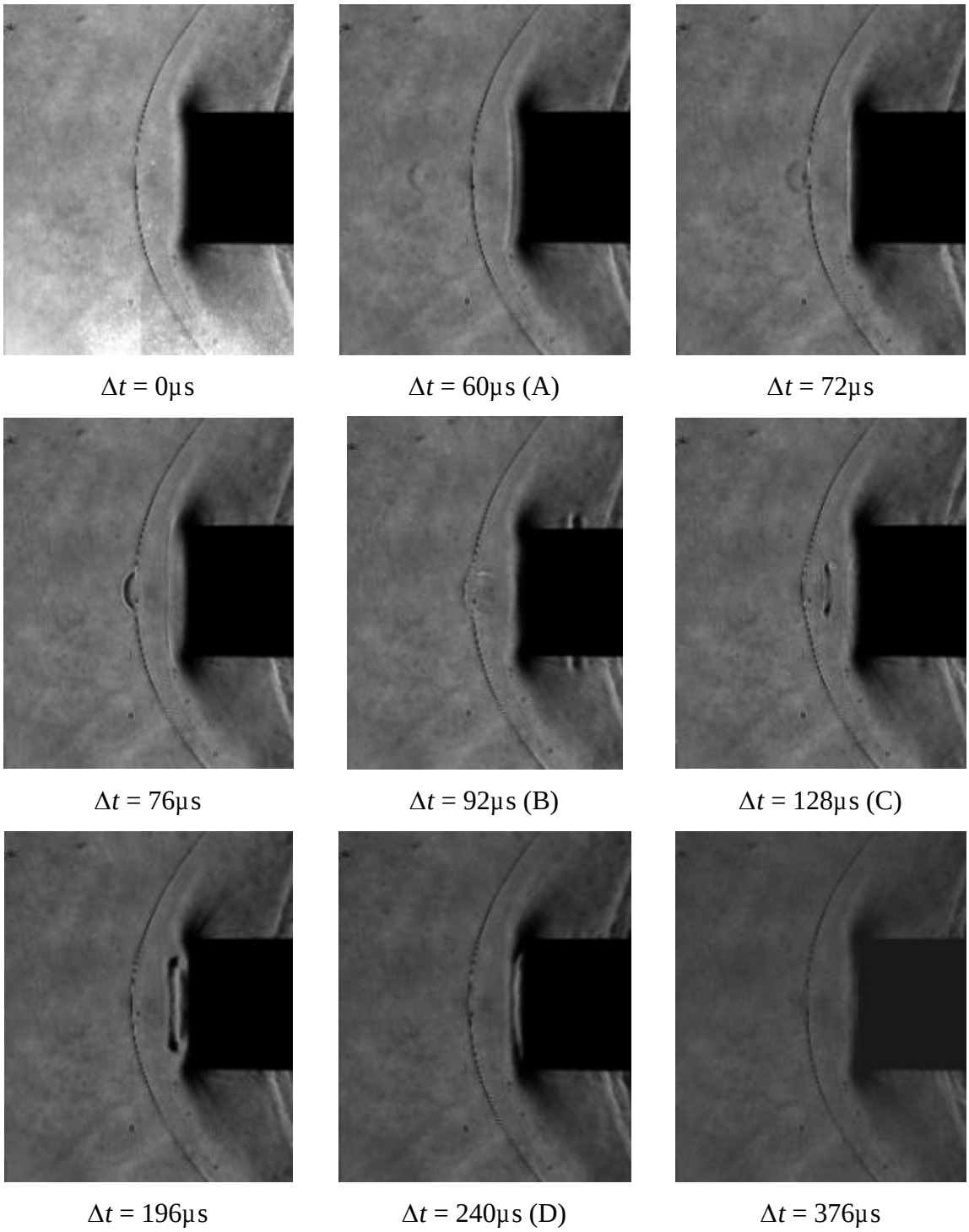

Figure 3 - 15 Sequential Schlieren images, *l/d*=2.0, *E*=13.2mJ/pulse, *f*=2kHz, framing interval=4μs, exposure=0.5μs

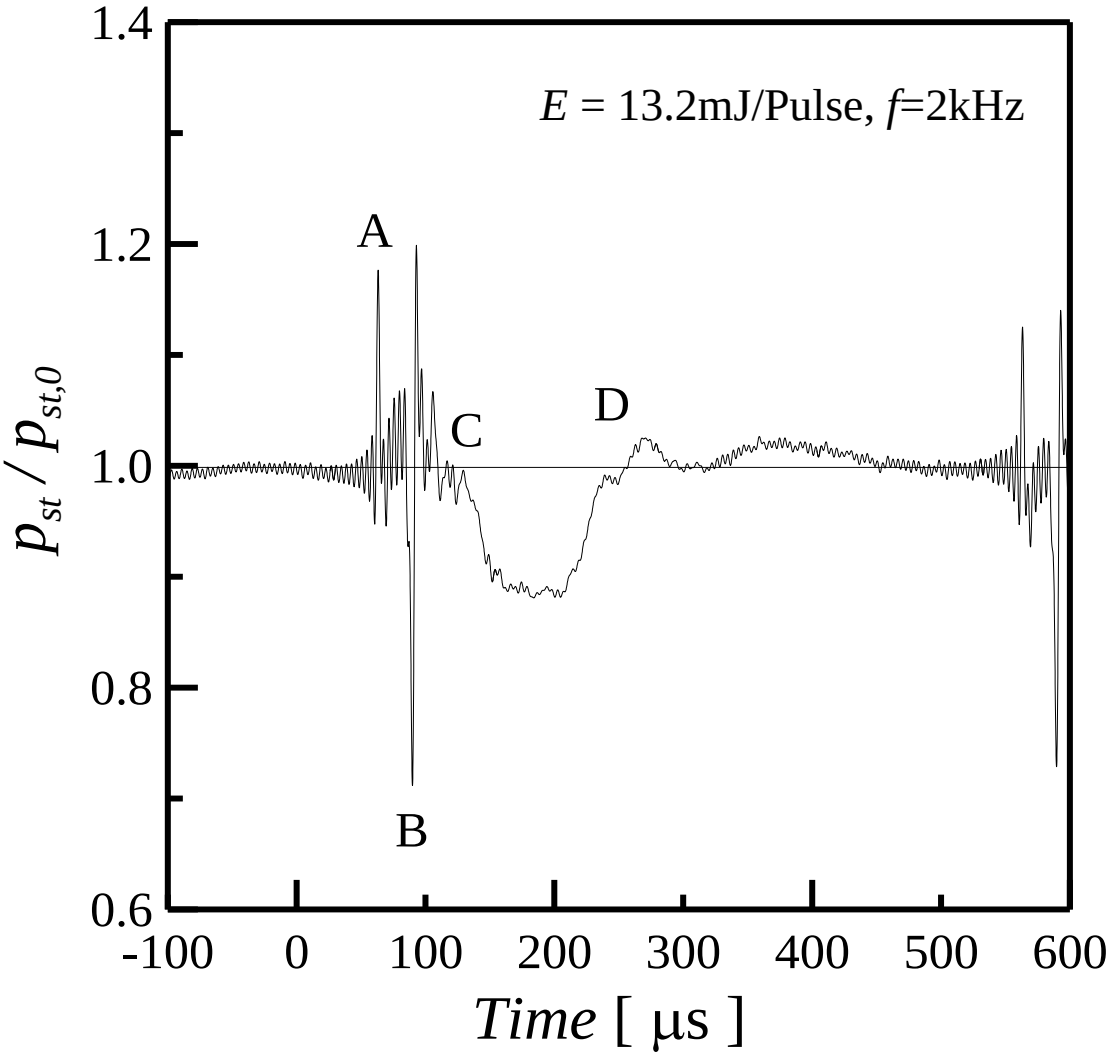

Figure 3 - 16 Stagnation pressure history corresponding to Fig. 3-15, *E*=13.2mJ/pulse, *f*=2kHz

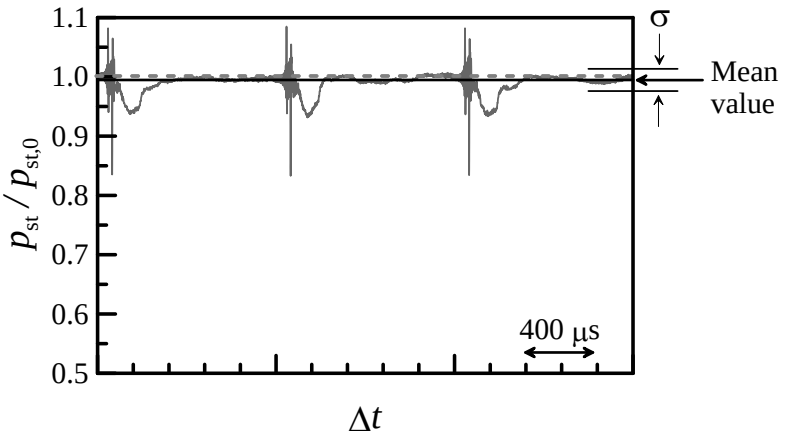

(a) *f*=1 kHz

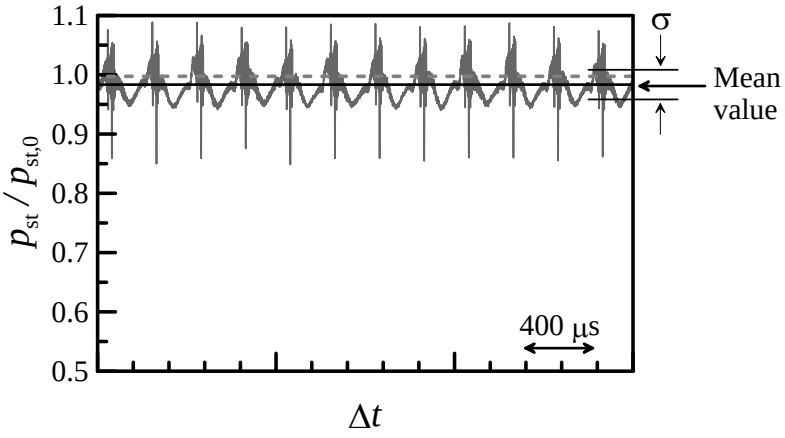

(b) *f*=4 kHz

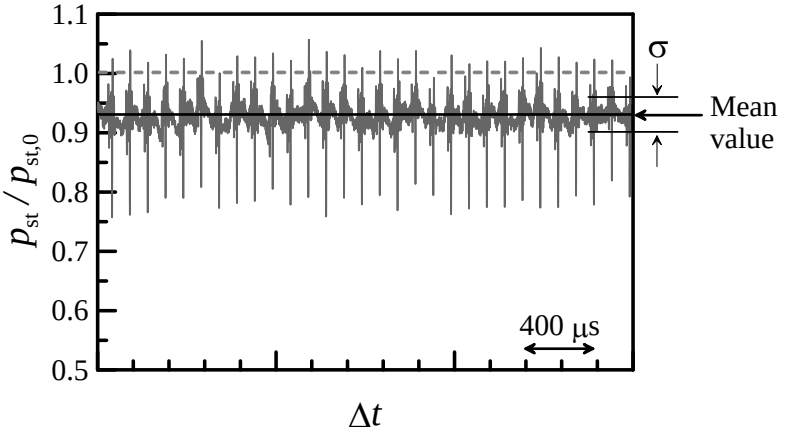

(c) *f*=10 kHz

(continued)

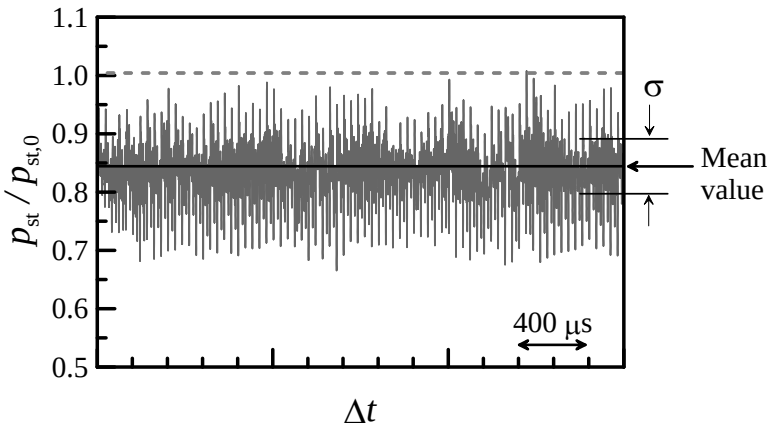

(d) *f*=25 kHz

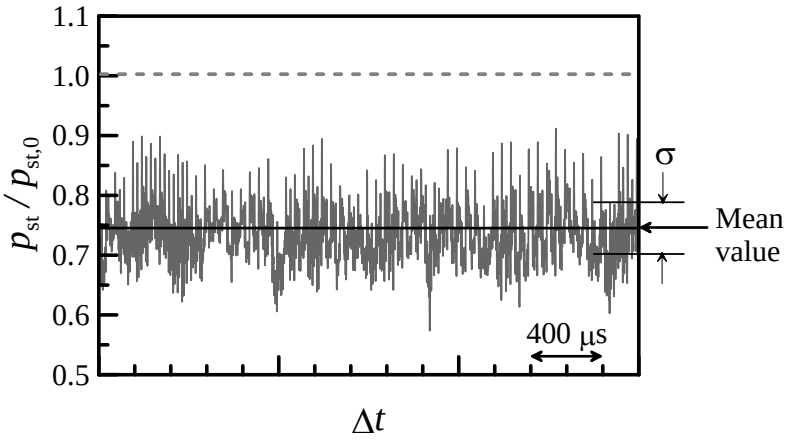

(e) *f*=40 kHz

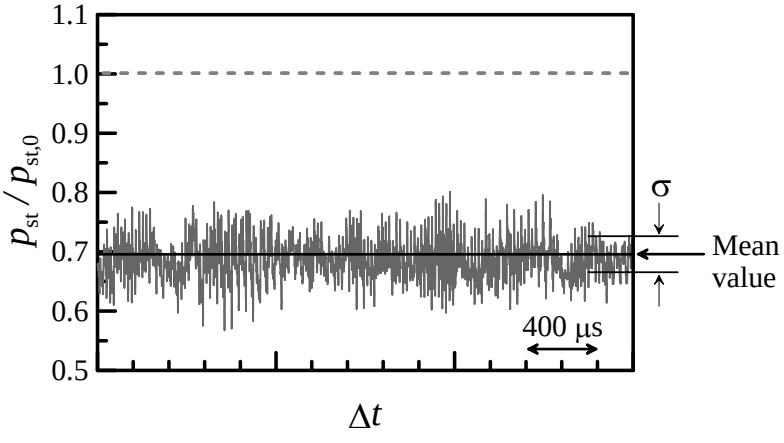

(f) *f*=50 kHz

Figure 3 - 17 Stagnation pressure histories, *l/d*=2.0, *E*=6.2~6.6mJ/pulse *f* = 1kHz ~50kHz, *t* is originated in the moment of the first laser pulse irradiation

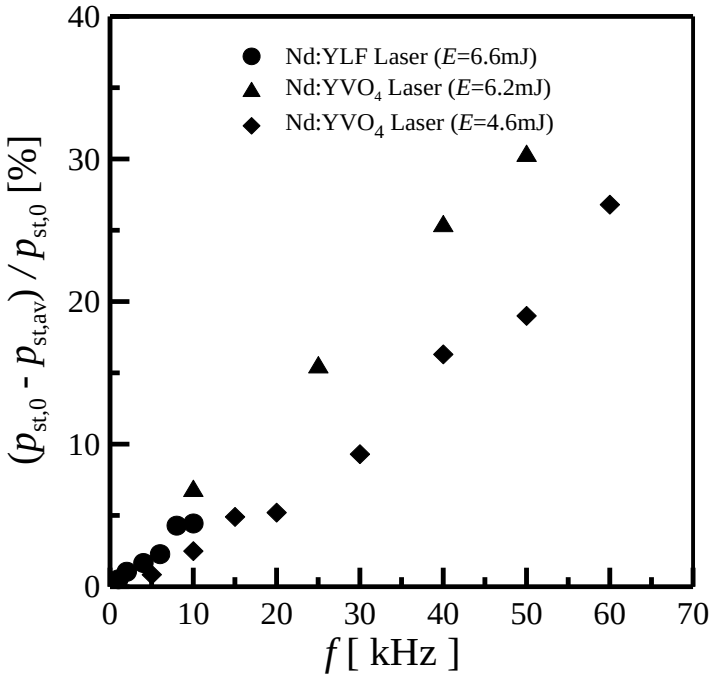

Figure 3 - 18 Time-averaged stagnation pressure as a function of laser frequency

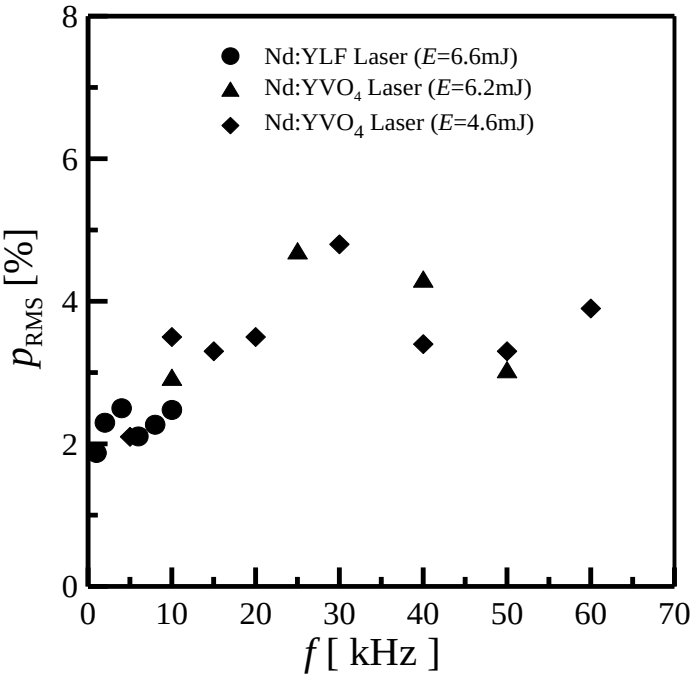

Figure 3 - 19 RMS value of stagnation pressure

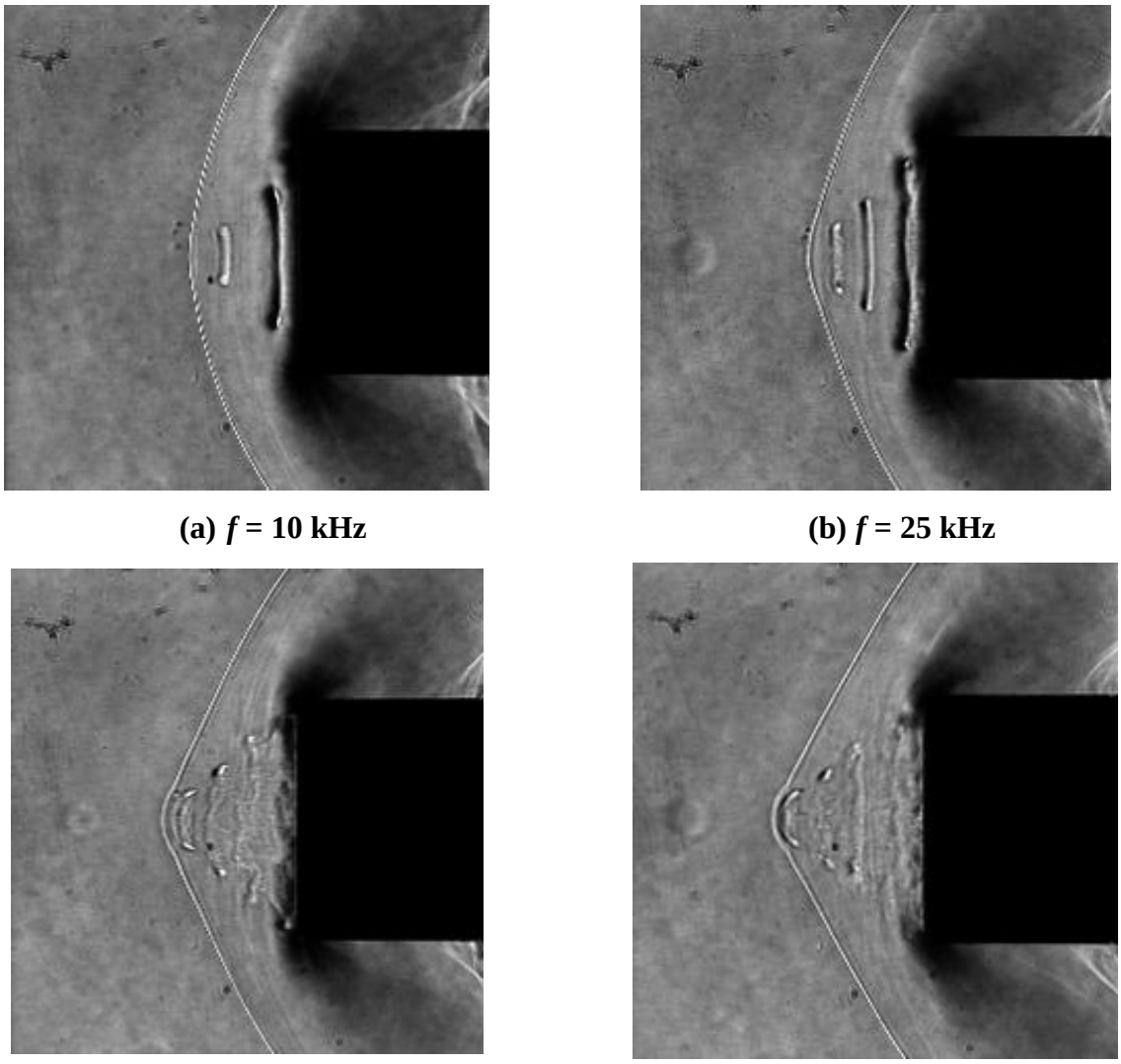

(a) f = 10 kHz **(b) f = 25 kHz**

(c) f = 40 kHz **(d) f = 50 kHz**

Figure 3 - 20 Still Schlieren image induced by high-repetitive laser pulses, l/d=2.0, E=6.2mJ/pulse

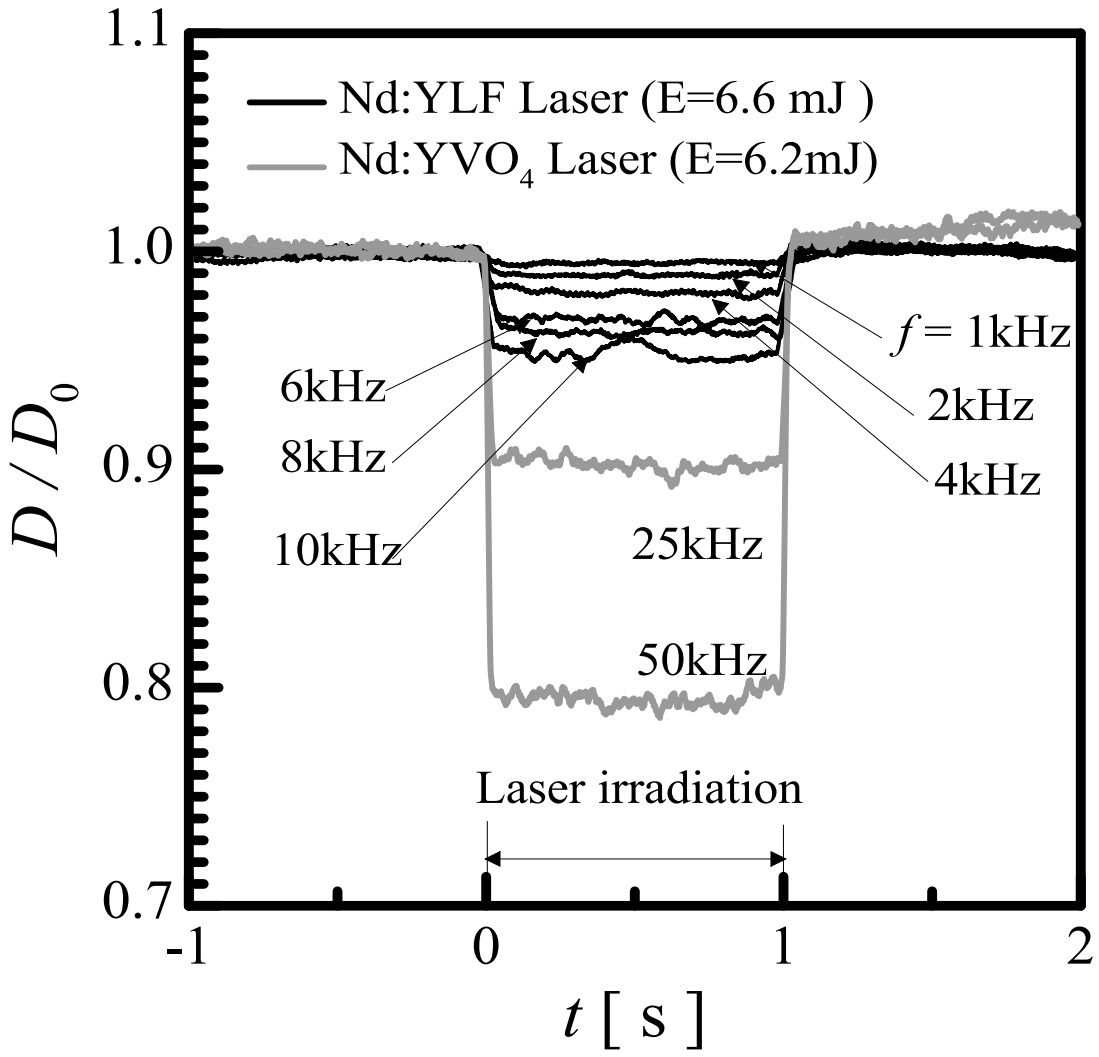

Figure 3 - 21 Normalized drag histories from 1kHz to 50kHz, *l/d*=2.0, *E*=6.2~6.6mJ/pulse

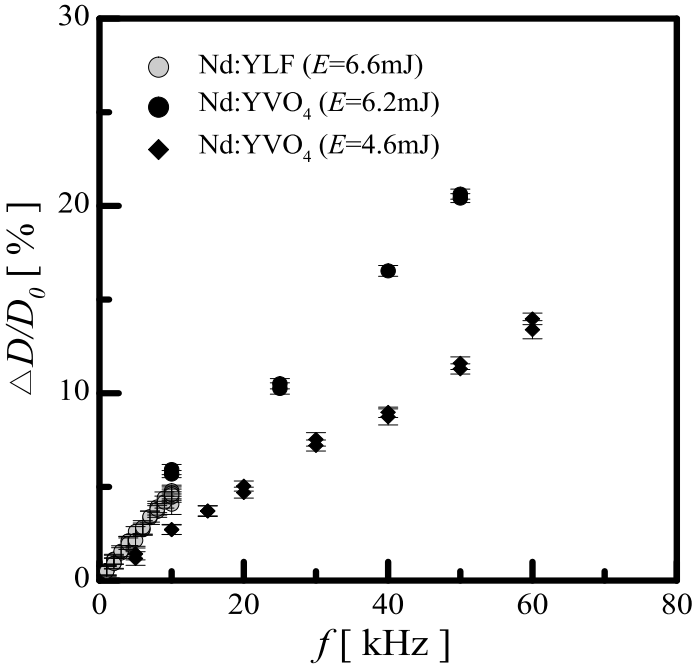

Figure 3 - 22 Drag reduction performance vs laser frequency, *l/d*=2.0, *E*=4.6~6.6mJ/pulse

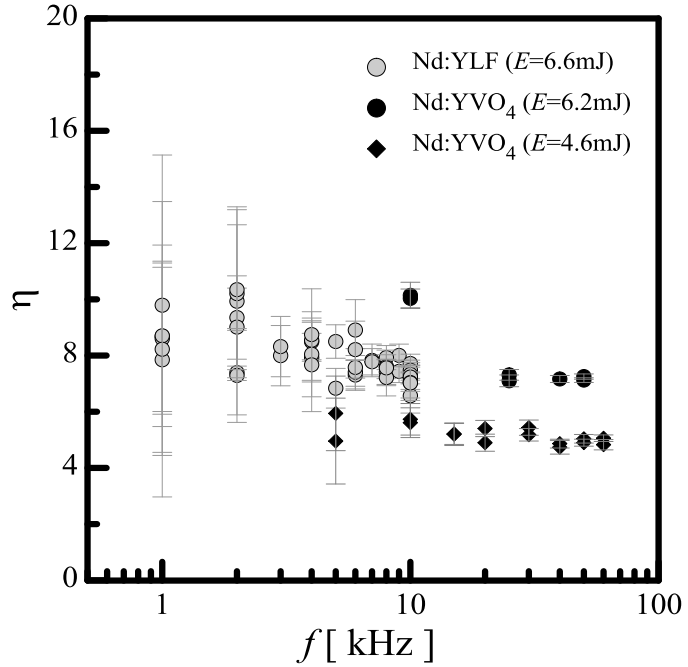

Figure 3 - 23 Power gain due to the energy deposition, *l/d*=2.0, *E*=4.6~6.6mJ/pulse

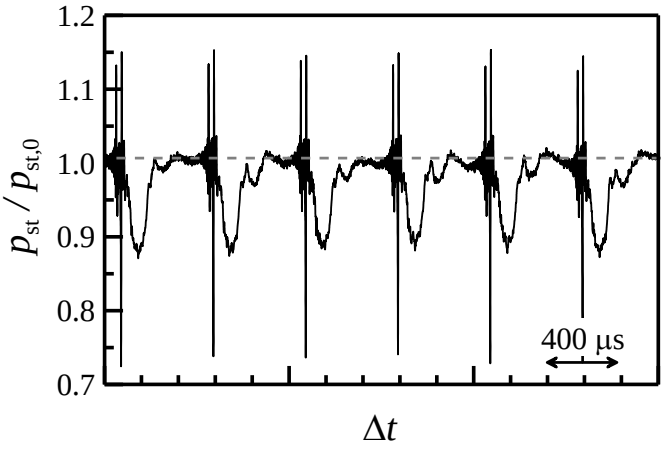

(a) *E*=13.2 mJ, *f*=2 kHz

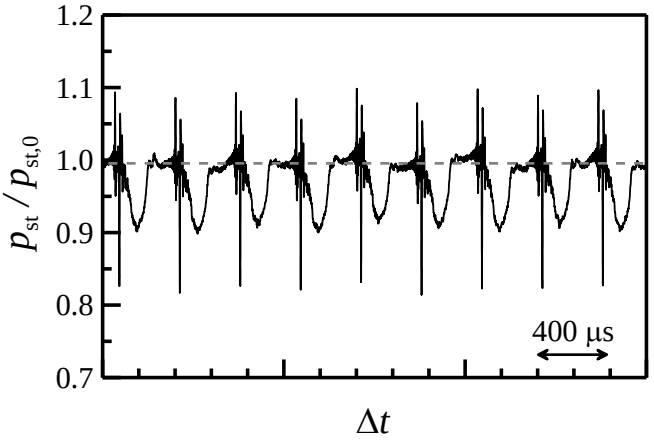

(b) *E*=8.8 mJ, *f*=3 kHz

(continued)

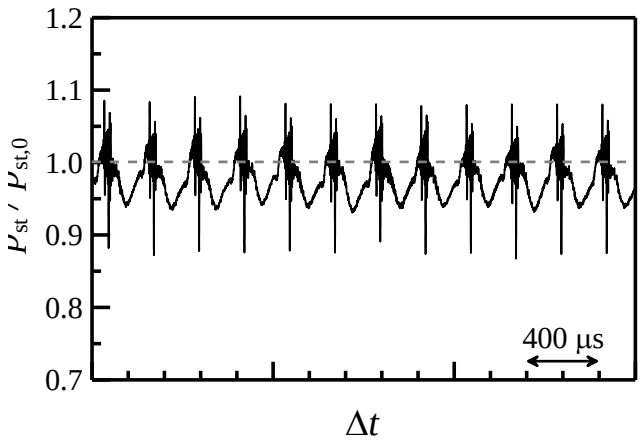

(c) *E*=6.6 mJ, *f*=4 kHz

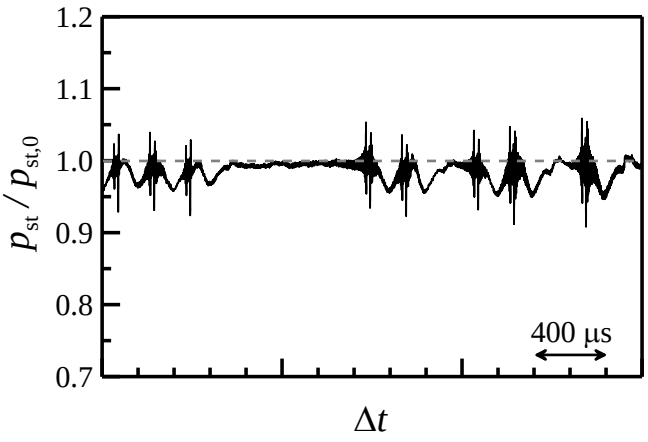

(d) *E*=5.3 mJ, *f*=5 kHz

Figure 3 - 24 Stagnation pressure histories, *l/d*=2.0, input power=26.4W

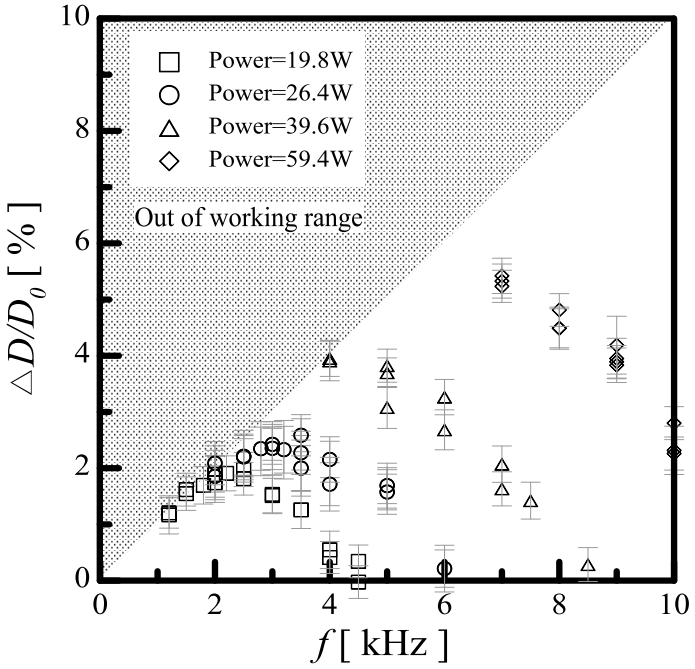

Figure 3 - 25 Effect of *E-f* combination on normalized drag reduction under same input power, *l/d*=2.0

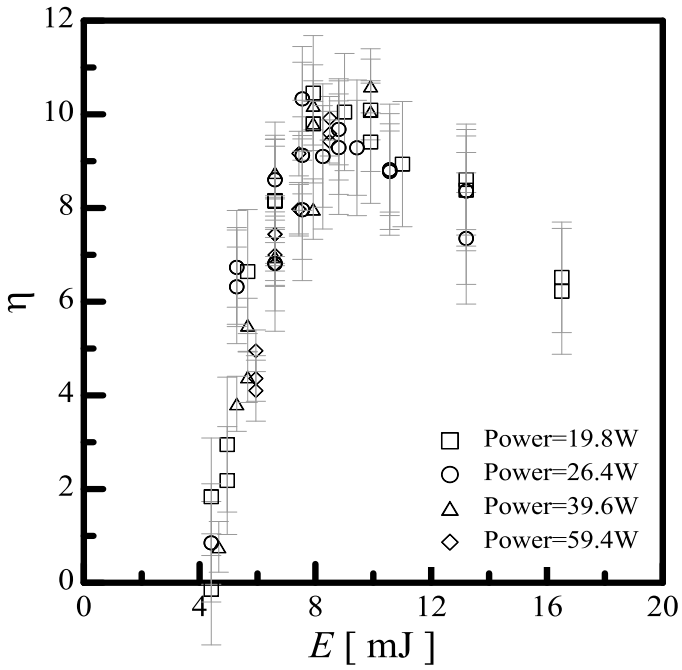

Figure 3 - 26 Power gain vs energy per pulse, *l/d*=2.0

Chapter 4. Interactions among Baroclinically-Generated Vortex Rings

Interaction phenomenon among the vortex rings is described in this chapter. Vortex rings with a constant circulation are repetitively generated by depositing laser pulse energies ahead of a bow shock wave over a flat-head cylinder. Each vortex ring is formed after baroclinic interaction between a laser-heated gas and the bow shock wave. Motion patterns of vortices interaction is classified into 3 motion types. For low pulse repetition frequency, vortices interact weakly. With increasing the pulse repetition frequency, mutual interactions among the vortices become stronger. In this case, alternate pitching motions at f_0=10 to 20 kHz and 'slip-through' motions at f_0=30 kHz appear. These interaction motions present the sub-harmonic frequencies in Power Spectral Density (PSD) distributions. With high-repetition frequency over 40 kHz, a quasi-steady-state acting spike which decreases the stagnation pressure is built up.

4-1. Introduction

It has been experimentally or numerically demonstrated that supersonic flows can be significantly moderated with laser pulse energy depositions. [P. K. Tret'yakov, P. K., et al. (1996); Sakai, T. (2009); Adelgren, R. A., et al. (2005); Sasoh, A. et al. (2006); Zheltovodov, A. A., et al. (2007); Sasoh, A., et al. (2010); Knight, D. D. (2008)] The fundamental processes occurring after a single energy deposition have already been well studied: A low-density bubble is generated by locally depositing an amount of laser pulse energy ahead of a shock layer; interacting with the shock wave a vortex ring is generated due to the baroclinic effect, which in turn moderates the pressure field in the shock layer. [Adelgren, R. A., et al. (2005); Sasoh, A. et al. (2006); Zheltovodov, A. A., et al. (2007)] With repetitively sending laser pulses, vortex rings can be repetitively generated and wave drag reduction can be realized on a time-averaged basis. [Sasoh, A., et al. (2010); Knight, D. D. (2008)] However, associated interactions among the vortex rings have not been well studied either due to low repetition frequency or to modest diagnostic instrumentation.

In general flow situations, vortex-vortex interactions often appear and lead to various unsteady flow motions. If two vortices have circulations of the same direction, mutually attractive forces are exerted between them, and eventually the vortices merge. [Hussain, A. K. M. F. (1986)] Such fundamental motions of the vortices can be well modeled based on Biot-Savart's law. In many real situations, a vortex has a ring shape. When two vortex rings interact with each other, peculiar motions such as 'slip-through,' occurs and lead to complicated flow evolution and acoustic emission. [Bridges, J. E., et al. (1987); Mitchell, B. E., et al. (1995)] However, experimental methodology of realizing such vortex interactions are quite limited: A single vortex ring can be generated behind a transmitting shock wave from the open end of a shock tube, or as a result of shock-bubble interactions. [Tang, S. K., et al. (1995); Liow, Y. S. K., et al. (2005)] A pair of counter-rotating vortices can be generated as a byproduct in ejecting a jet to an open space [Brouillette, M., et al. (1997)]. However, it is difficult to generate many vortex rings having a constant circulation without contaminating flow fields. [Minota, T., et al. (1993)]

In this chapter, undisturbed vortex rings with a constant circulation can be repetitively generated by laser pulse energy depositions over a bow shock layer in Mach 1.94 flow. Mutual interactions among the vortex rings having three-dimensional nature, which lead to building-up an acting spike in the shock layer, are observed using high-speed framing schlieren images and stagnation pressure measurement with various laser pulse repetition frequencies of up to 60 kHz.

4-2. Experimental Methods

Figure 4-1 shows the schematic illustration of the experimental setup of this study. A supersonic flow of a Mach number of 1.94 is generated in an in-draft wind tunnel with 80 mm × 80 mm square cross-section. The nominal flow conditions are a temperature of 163 K, and a static pressure of 13.8 kPa for a stagnation pressure of 101.3 kPa. The wind tunnel is connected to a dump tank of an inner volume of 11.5 m^3; the effective run time is about 10 s. The central 30 mm × 30 mm square is an effective core in which the Mach number variation is within 0.7 %. At the test section, a pair of 90-mm-dia., BK-7 windows are flush-mounted on the tunnel side walls. Through the windows both the incident laser beam and a collimated probe beam for schlieren visualization are sent. A 20-mm-dia. circular cylinder model made of brass is set on the center axis. Laser pulses are focused on the axis at a separation distance of 40 mm from the flat head of the cylinder model. As the power source for the energy depositions, an Nd:YVO_4 repetitive-pulse laser (HD401-E, FWHM of 10 ns) is used. The output laser beam of 6 mm × 6 mm square is expanded with a pair of concave-convex lenses to a 12 mm × 12 mm square, then being reflected on two 45-degree reflection mirrors, and is focused with a lens with a focal length of 60 mm that is placed immediately before one of the BK-7 windows. The effective input energy of a single laser pulse, that is an output laser energy subtracted by losses on or through the lenses, mirrors and windows, is set to 4.6 mJ. The alignment of the focal point is examined from the view through the inlet of the wind tunnel. The time variation of the density field over the cylinder model is visualized through a schlieren system including two 300-mm-dia. concave mirrors and a circular knife edge. In a single run of the wind tunnel one hundred frames of schlieren images are captured into a high-speed framing camera (Shimadzu HPV-1) with a framing interval of 4 μs, 1/4 of which is an exposure period. At the center on the flat head of the cylinder model, a piezoelectric pressure transducer (H112A21, PCB Inc., rise time of 1 μs, sensitivity of 7.015mV/Pa, 5.56 mm in dia.) is flush-mounted to measure the time variation of the stagnation pressure.

4-3. Weak Interaction Regime (f_0 = 5 kHz)

When the static pressure is of the order of the atmospheric value (about 100 kPa), laser-heated gas itself experiences strong instability [Sasoh, A., et al. (2006); Glumac, N., et al. (2005); Brieschenk, S., et al. (2008)] ; for example, Glumac et al. (2005) shows formation of a center jet in the opposite direction of the laser beam, which in turn induces a vortex ring. However, at the lower pressure level of this study as well as of others [Adelgren, R. A., et al. (2005); Sasoh, A., et al. (2010)], from experimental observation the laser-heated gas does not experience such strong instability, and can be modeled as a sphere. Generation of a vortex ring from the interaction between a laser-pulse-heated gas of a spherical shape and a bow shock wave is well studied by Adelgren (2005), and Sasoh et al. (2010) When the heated gas enters a bow shock wave, a baroclinic term is generated as a result of a vector product of the density discontinuity surrounding the gas and a pressure jump across the shock wave, see Fig. 4-2. With an axi-symmetric configuration, a vortex ring is formed. A counter flow velocity is induced on the center axis. [Sasoh, A., et al. (2010)] Figure 4-3 shows sequential schlieren images of the interaction of a laser heated gas and the bow shock wave with a laser pulse repetition frequency, f_0, of 5 kHz. In this and following figures, Δt and τ ($=1/f_0$) designate a time elapsed from a reference moment and the time interval between successive laser pulses, respectively. At this low frequency, the interactions among the vortex rings are negligible. At $\Delta t / \tau = 0$, the sphere of the laser-heated gas enters the bow shock wave. At $\Delta t / \tau = 0.04$, a small hump in the bow shock wave is formed on the center axis due to the 'lens effect.' [Sasoh, A., et al. (2006); (2010)] Then due to the flow in the shock layer the vortex ring moves downstream with its radius increasing. It should be noted that in this weak-interaction condition, the vortex ring keeps its axi-symmetrical shape during the whole processes of the interaction. The stagnation pressure has a strongest spectrum of the fundamental frequency, f_0, see Figs. 4-8(a)(pressure history) and Fig. 4-9(a)(power spectra). Events in the interaction cause other spectra of higher frequencies. However, spectra with lower frequencies, which hereafter will be referred to as 'sub-modal spectra,' are weak.

4-4. Instabilities in Transitional Regime

In the intermediate frequency regime from 10 to 30 kHz in the present experiments, interactions among neighbor vortex rings become strong.

4-4-1. Alternate pitching motion and sub-modal spectra (f_0 = 10 to 20 kHz)

Figures 4-4(a) and (b) show examples of vortex ring motions observed in different operations yet under the same operation condition of f_0=15 kHz. In the case of Fig. 4(a), the vortex rings have pitching deflections in alternate orientations: For example, the vortex ring A has a clockwise pitching deflection, then the vortex B has the counter-clockwise, the vortex C clockwise; the vortexes D and E have obviously counter-clockwise and clockwise ones, respectively. Such motions continue at least during the period of flow visualization.

In the case of Fig. 4-4(b), the vortex rings have yawing deflections. Although in the present system for visualization, their orientations cannot be resolved, the vortex rings are believed to have alternate orientations as is observed in Fig. 4-4(a). Figure 4-5 schematically illustrates fundamental processes of vortex-to-vortex interactions observed in Fig. 4-4(a). Since all vortex rings have a vorticity in the same direction, attractive forces are exerted among them. An attractive force is obtained from Biot-Savart law in which its magnitude is in inversely proportional to a separation distance. For example, once the vortex ring A has a clockwise pitching deflection, it attracts the next-generated vortex ring B more strongly in the lower side because their separation distance becomes shorter; a counter-clockwise pitching deflection is induced in the vortex ring B. Due to this deflection, a stronger attractive force is exerted from the vortex B to the next vortex C, thereby inducing its clockwise deflection. Since such processes are repeated in successive vortex rings, the alternate pitching motions as are observed in Fig. 4-4(a) appear. The azimuthal orientation of such vortex-to-vortex interactions cannot be controlled a priori but is determined in situ in a random manner. If a triggering deflection occurs in the yaw

direction as in seen in Fig. 4-4(b), a similar alternate yaw motions appear. Such motions as shown in Figs. 4-4(a) and (b) are based on the same mechanisms, then will hereafter be referred to uniquely as 'pitching' motions. As seen in Figs. 4-8(b) and 4-9(c), which correspond to the run of Fig. 4-4(a), unlike in the weak interaction regime the power spectral density distribution in the stagnation pressure has a strong sub-modal line spectrum of $f / f_0 = 0.5$ which is caused by the above-mentioned alternate pitching motions. The same line spectrum is obtained with f_0 = 10 to 20 kHz; with f_0 = 20 kHz the spectrum of f=7.3 kHz ($f / f_0 \equiv 0.37$) is also strong. In this regime, another strong line spectrum are obtained at about f = 1.6 kHz ($f / f_0 \equiv 0.16$ with f_0 =10 kHz, $f / f_0 \equiv 0.0.11$ with f_0 = 15 kHz and $f / f_0 \equiv 0.08$ with f_0 = 20 kHz.), the origin of which is currently an open question.

4-4-2. Strong interaction (f_0 = 30 kHz)

Figure 4-6 shows schlieren images with f_0 = 30 kHz. In this case, the interactions among neighbor vortex rings become strongest, and 'slip-through' of vortices [Tang, S. K., et al. (1995); Liow, Y. S. K., et al. (2005); Yamada, H., et al. (1979)] is observed. At $\Delta t / \tau = 0$, the vortices F and G are placed in their original orders. However, the diameter of the vortex G is increased, whereas the diameter of the vortex F is decreased due to the flow already induced by previous vortexes. As a result, the diameter of the vortex G becomes larger than that of the vortex F; the former swallows the later – their relative locations and dimensions are inversed. This tendency can be found also in the interaction of the vortexes H and I. Such strong interactions continue, yet the shapes, dimensions and locations of vortex rings change with large randomness. The power spectra in this case, see Fig. 4-9 (e), are much different from those of f_0 = 20 kHz; sub-modal spectra become much dispersed without any discrete, strong line spectrum. Specrta of higher than f_0 becomes stronger. It should be noted that the spectra of f_0 = 30 kHz are basically similar to those of f_0=40 to 60 kHz. At this peculiar frequency, the laser pulse repetition frequency is low enough to distinguish elemental interactions among neighbor vortexes, yet is high enough to place vortex rings close enough to each other to obtain dispersed spectra in the stagnation pressure history.

4-5. Quasi-Steady-State Regime (f_0 = 40 to 60 kHz)

At relatively-high f_0, 40 to 60 kHz, a quasi-steady-state structure is established ahead of the flat head. This structure is composed of several vortex rings close to each other, and forms a 'virtual spike.' Although in the virtual spike many small perturbations, which correspond to the dispersed power spectra in the sub-modal regime, exist, the outline of the spike and the stagnation pressure are in quasi-steady-state, see Fig. 4-8(d). The effective angle of the spike depends on f_0. It is shown that frequency region of dispersed PSD appears at lower frequencies with increasing of f_0, see Fig. 4-9(e) to (h). This implies that the flow structure asymptotically approaches to a steady-state with increasing f_0.

4-4. Summary

Utilizing the baroclinic effect between a laser-heated gas and the bow shock wave, series of vortex rings of a constant vorticity are experimentally generated in the shock layer by repetitively depositing laser pulse energies. At low f_0 ($\leq$ 5 kHz,), interactions among the vortex rings are weak. In the intermediate repetition frequencies (10 kHz $\leq$ f_0 $\leq$ 30 kHz), strong interactions among neighbor vortex rings are observed. The pitching interactions yield sub-modal line spectra in the stagnation pressure history. At f_0 = 30 kHz, stronger interactions even lead to slip-through of vortex rings. Increasing f_0 over 40 kHz the flow field asymptotically approaches a steady-state structure to form a virtual spike composed of several vortex rings.

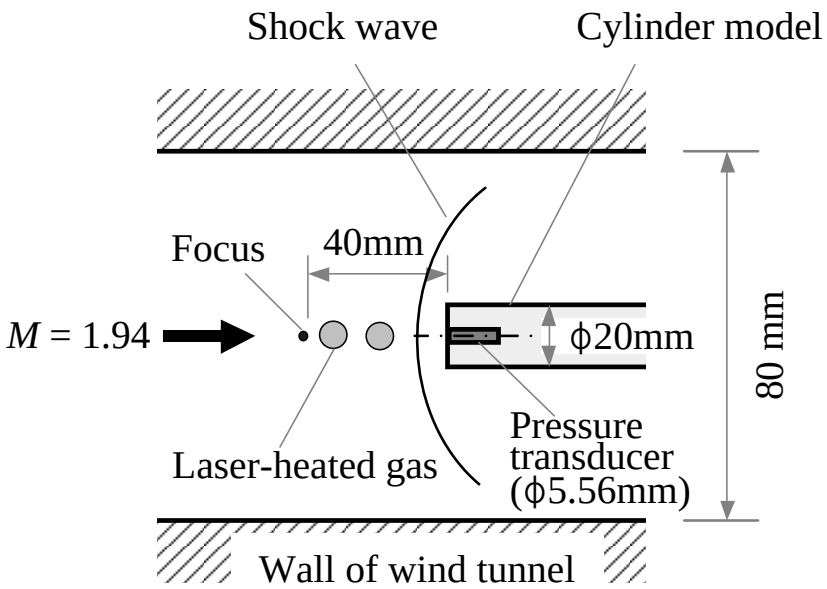

Figure 4 - 1 Experimental setup

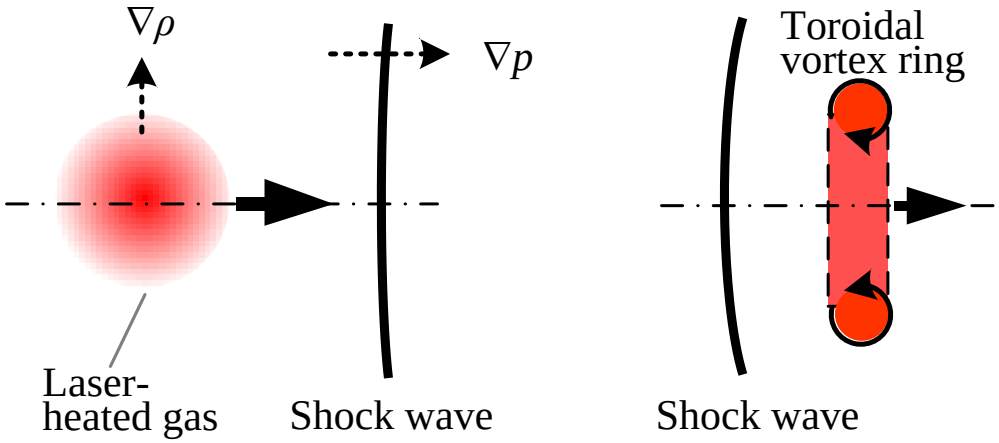

(a) Before entry (b) After entry

Figure 4 - 2 Generation of a vortex ring through baroclinic interaction between laser-heated gas and shock wave; ⊗ clockwise vorticity, ⊙ counter-clockwise vorticity

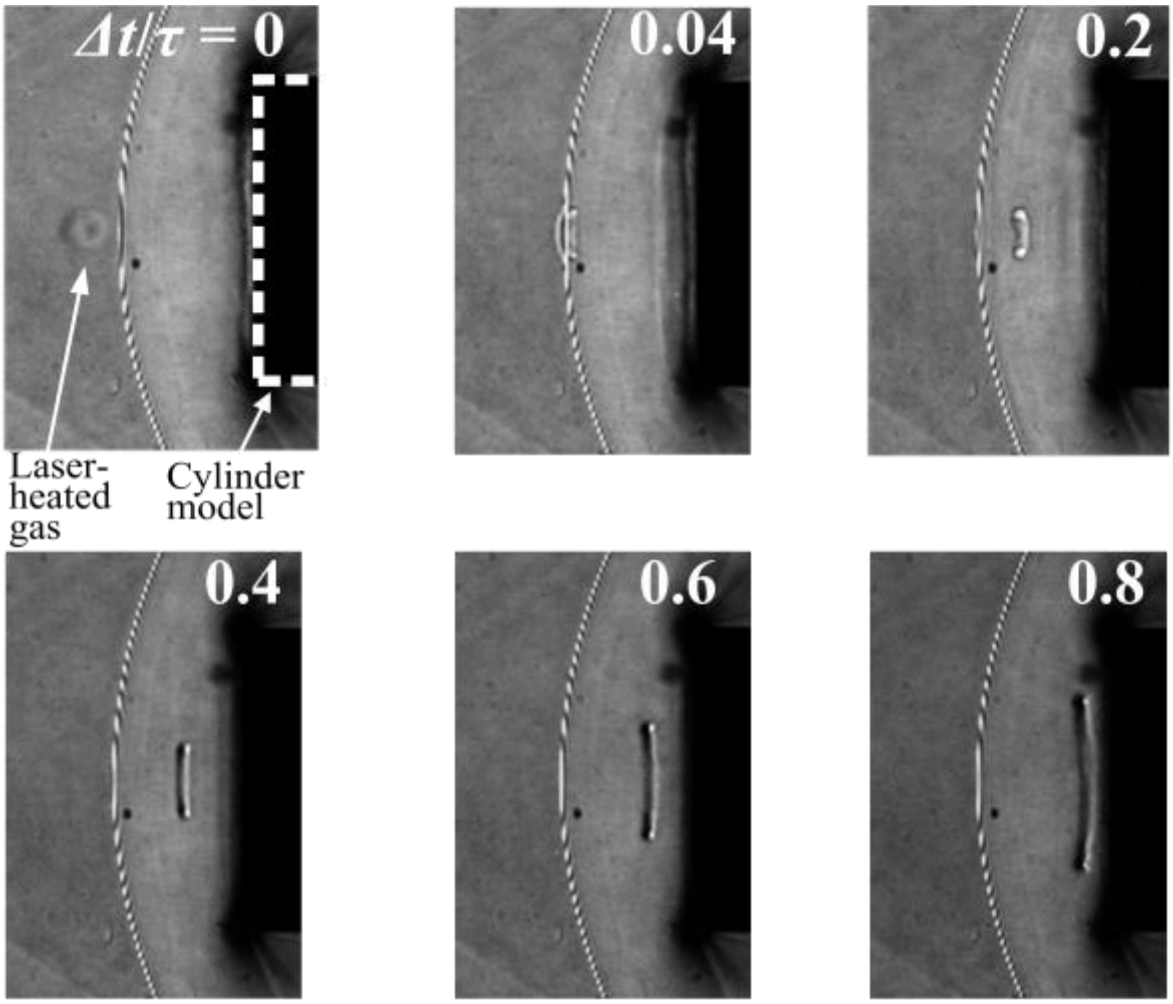

Figure 4 - 3 Sequential schlieren images with f_0 = 5kHz

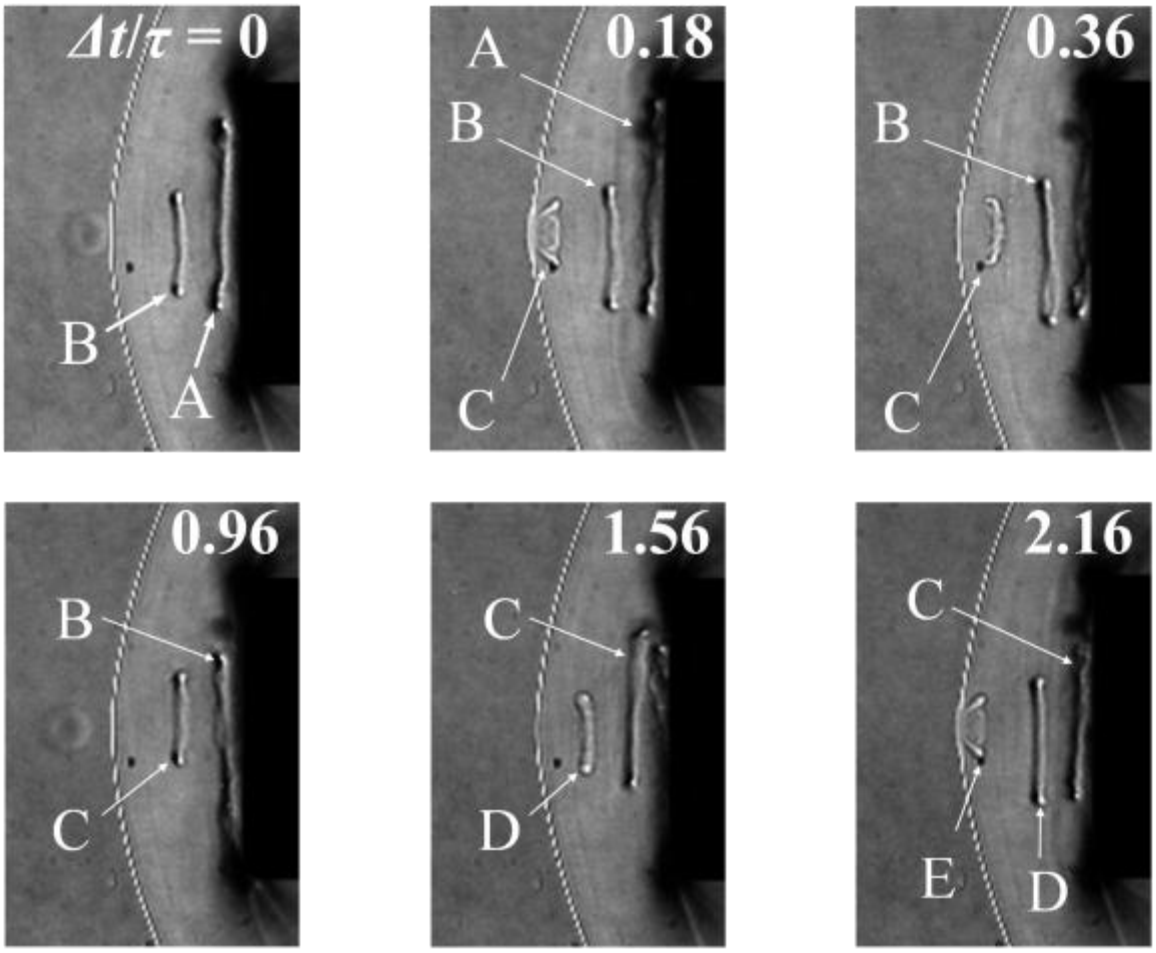

(a) Interaction with pitching motions

(continued)

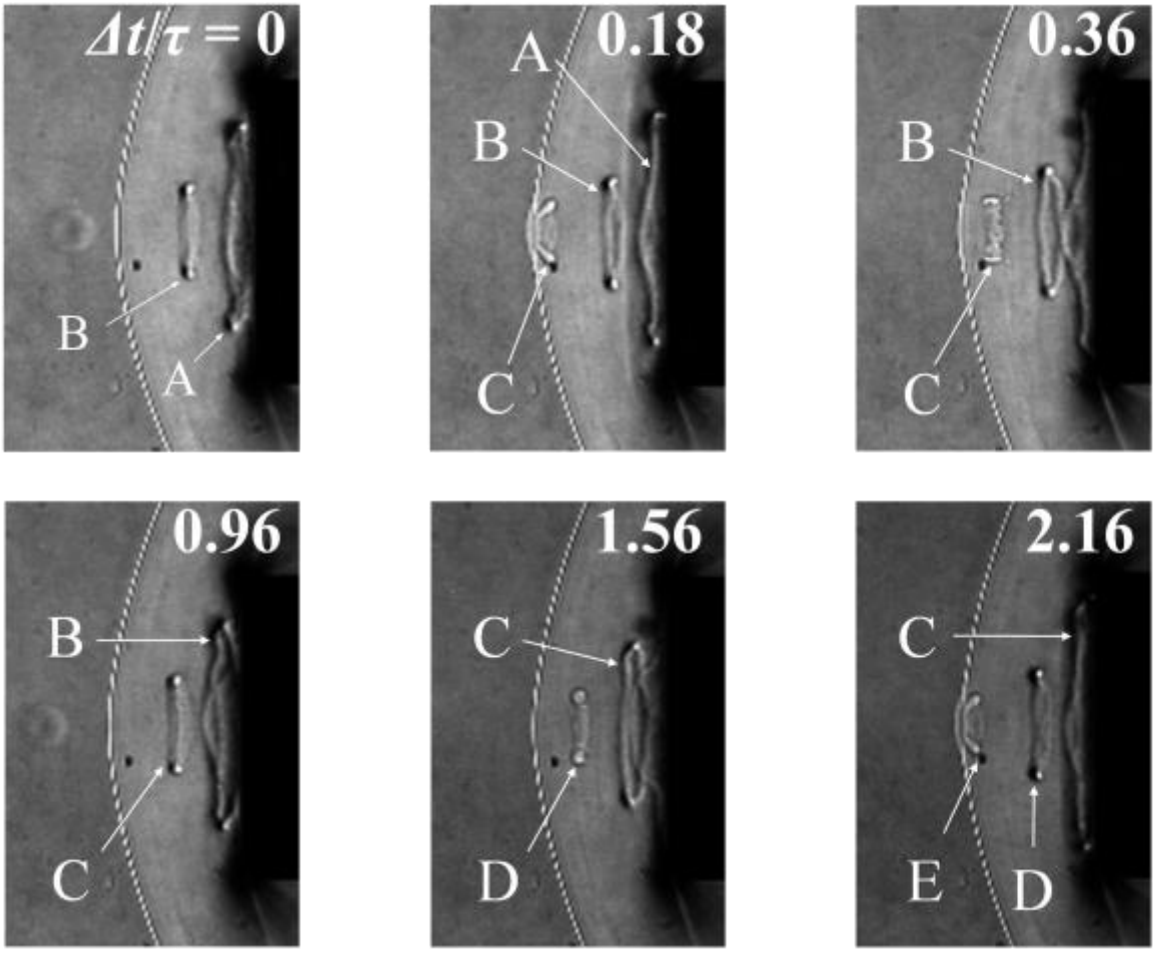

(b)Interaction with yawing motions

Figure 4 - 4 Sequential schlieren images of vortices interactions with f_0 = 15 kHz

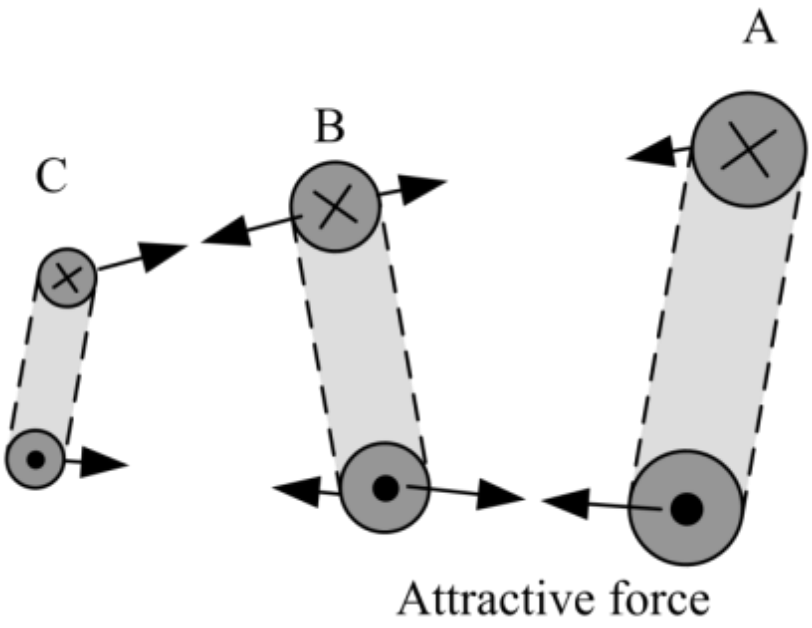

Figure 4 - 5 Fundamental processes of vortex-to-vortex interaction, cross-sectional view on a plane along the center axis; ⊗ clockwise vorticity, ⊙ counter-clockwise vorticity

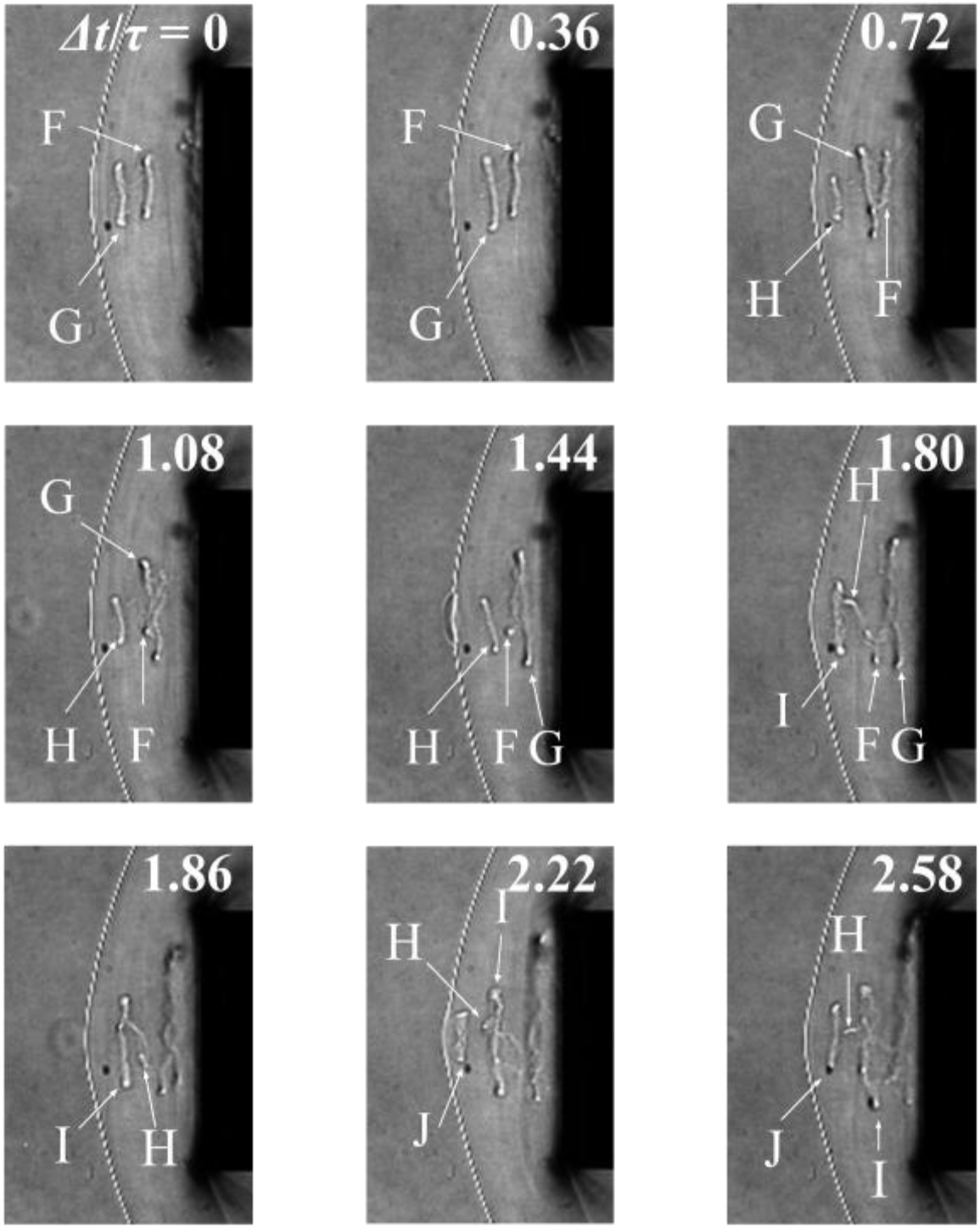

Figure 4 - 6 Sequential schlieren images with f_0 =30 kHz

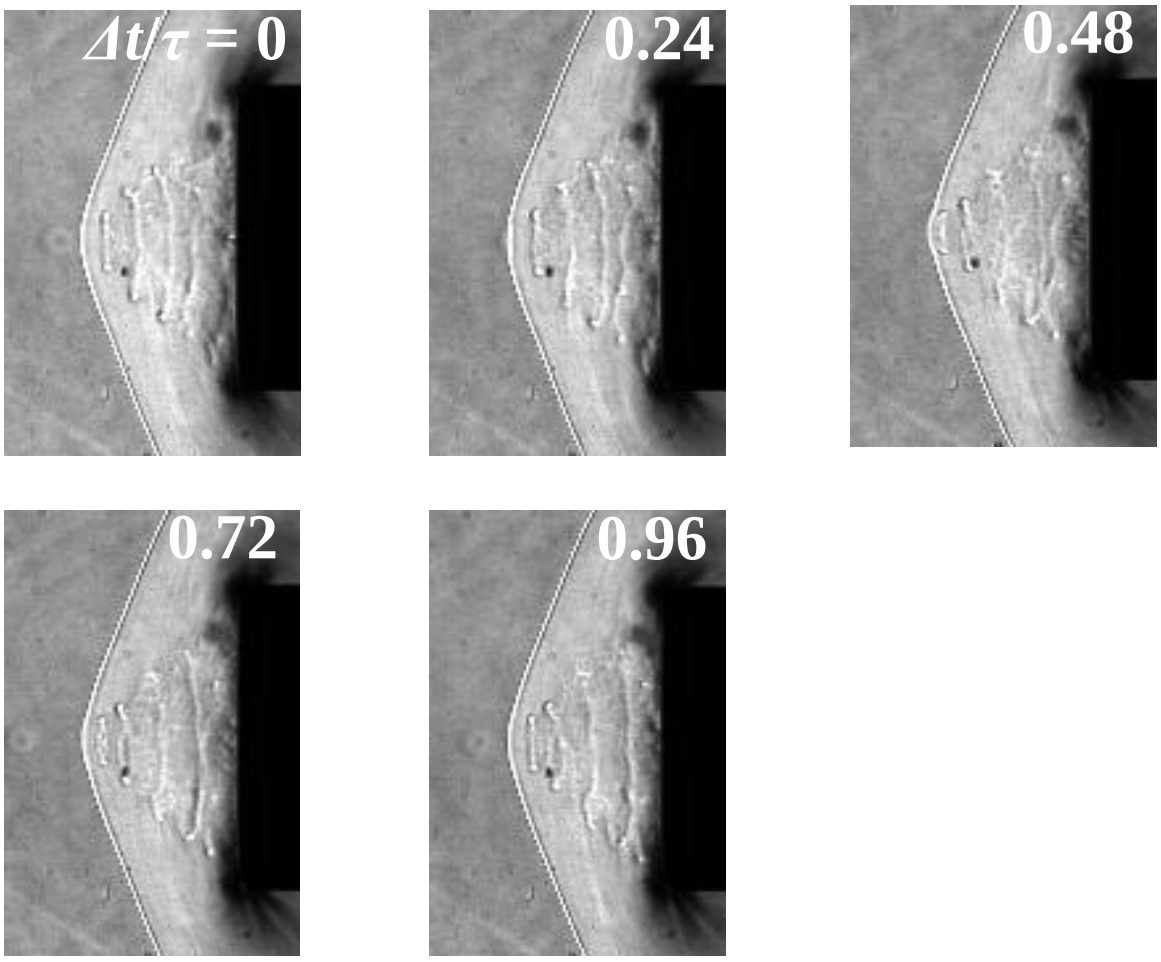

Figure 4 - 7Sequential schlieren images with f_0 = 60 kHz

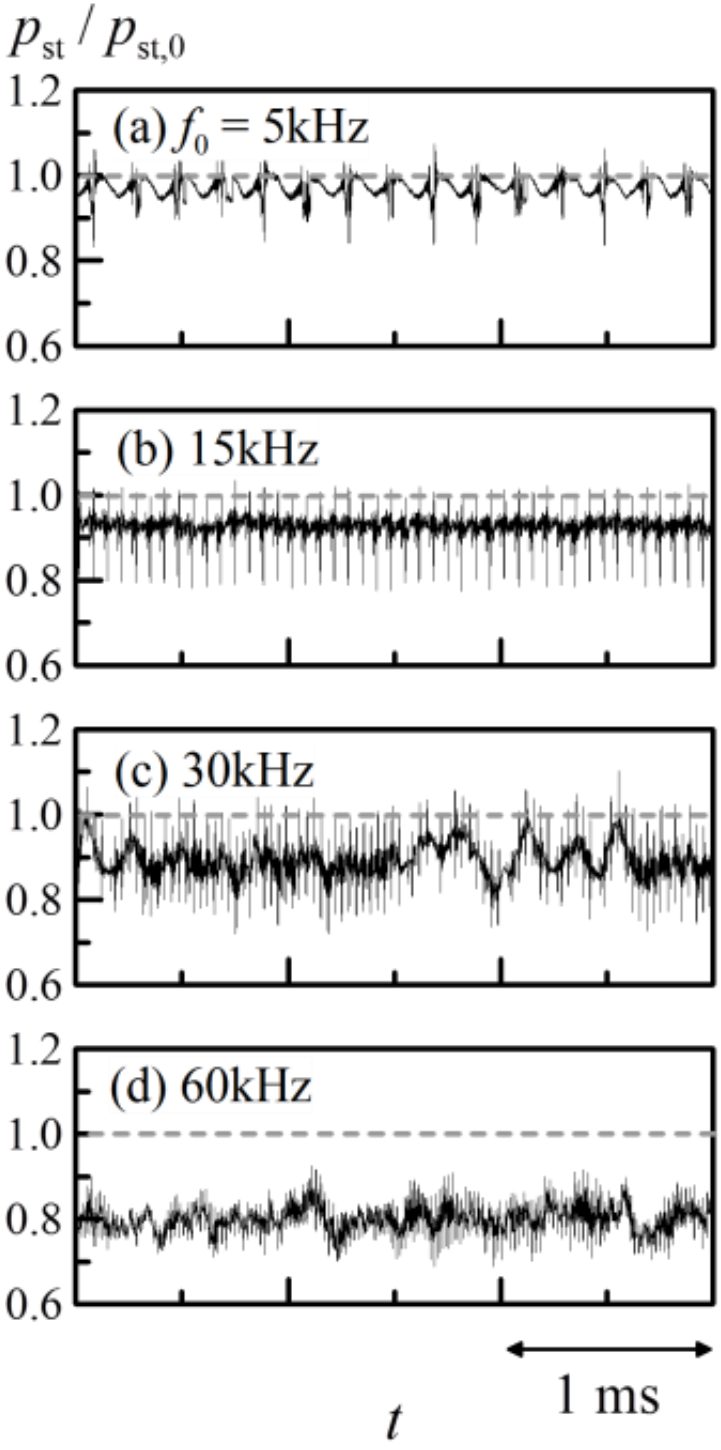

Figure 4 - 8 Histories of stagnation pressure, p_{st}, normalized by its time-averaged value without laser pulse energy depositions, $p_{st,0}$.

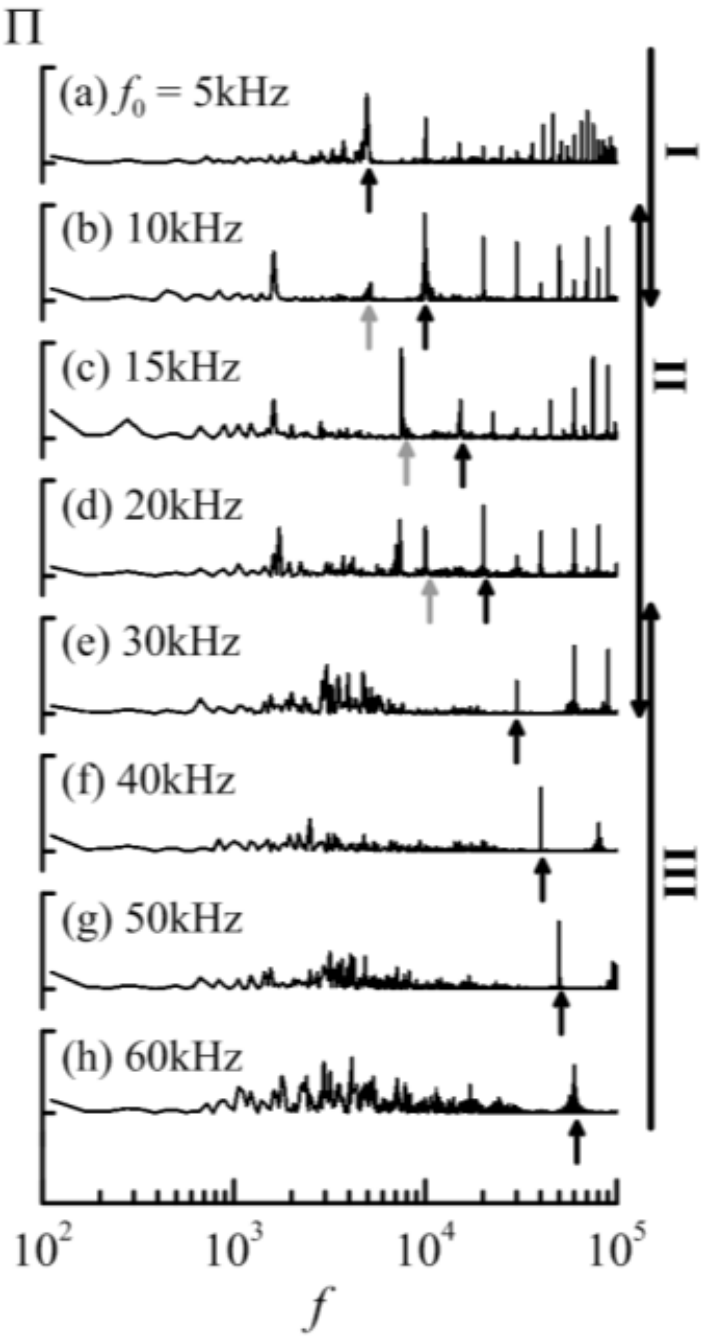

Figure 4 - 9 Distributions of power spectral density of p_s, Π (= PSD × f),

I; weak interaction regime,

II; transitional regime,

III; quasi-steady-state regime.

Chapter 5. Wave Drag Reduction Performance over Truncated Cone

In this chapter, drag reduction performance over truncated cone model is estimated. Truncated cone model is proposed to trade-off between the magnitude of drag force reduced and power gain due to energy deposition scheme as a combination of flat-faced blunt body and sharp cone body. In the experiments, diameter ratio (d_f/d) is varied from 1.0 to 0.0 with flat-faced truncated cone model. From the visualization results and stagnation pressure histories, it is concluded that effective residence time of vortices resulted by laser-heated gases interaction with shock wave plays an important role in drag reduction performance of truncated cone model. In order to improve the drag reduction performance of truncated cone, concave-faced truncated cone model is also suggested and its performance is estimated. As a result of validation with flat-faced truncated cone, it is concluded that concave-faced truncated cone has more effective drag reduction performance.

5-1. Introduction

In the previous chapter, an experimental study was conducted on the effect of repetitive energy depositions over the blunt body in supersonic flows. However, in actual application of energy deposition scheme to reduce the drag, it should be taken into account the magnitude of drag force or drag coefficient as well as drag reduction performance.

Figure 5-1 indicates why truncated cone shape is important to apply energy deposition scheme. In order to realize the energy depositions for improvement of drag reduction, two conditions should be satisfied obviously. The first condition is that the magnitude drag force or drag coefficient has lower value than the one of a conical body. Another condition is power gain. When the energy is deposited into the flowfield, the power gain which is defined by ratio of obtained saving power and depositing power should be more than unity. These necessary conditions suggest usefulness of energy depositions scheme for the improvement of aerodynamic performance in supersonic flight. As shown in Fig. 5-1, for a flat-faced blunt body, it is indicated the more effective the drag reduction performance; amount of drag reduction is significantly decreased and the power gain has higher value comparing with ones of other models. In spite of

high performance, considerable deposition power is required to achieve the drag force below the one for the conical model. On the other hand, the drag force of cone shape model has small value because of oblique shock wave generated in front of the body. However, it may not be expected the high drag reduction and power gain over unity using the energy depositions. Hence, even though the drag reduction with energy deposition is more effective for a blunt body with larger bluntness, the drag without energy deposition is relatively higher as bluntness is larger. This tradeoff problem to obtain the suitable drag reduction performance leads to propose the truncated con model. Although the drag reduction performance with truncated cone model is weaker, it is easily accomplished the target drag force because its base drag force has smaller value compared to blunt body. In this case, the effective time, for which the effect of the energy deposition on a blunt body lasts, is a key parameter to know what shape of a body is better to obtain a lower drag.

Sakai (2008) reported that the effective time is evaluated during the interaction of the low density core created by a single laser pulse using an Nd:YAG laser with the bow shock wave over a blunt body. The evaluated effective time on a flat-faced cylinder is longer than on a hemisphere under the same energy deposition condition. The longer effective time for the flat-faced cylinder is due to the fact that the recirculation zone with vortices, which are produced due to baroclinic interaction, keeps for longer time in the forebody region. This behavior results in the reduction of the drag for a longer period. He also presented that the modulated drag for the flat-faced cylinder is nearly the same with that for the hemisphere and that the drag value is higher than that for a sharp cone with the same base diameter. It should be noted that the efficiencies for the flat-faced cylinder are typically higher than for the hemisphere under the same energy deposition condition. Thus, it is believed that a flat-faced geometry has a potential advantage to be used in the drag reduction with energy deposition.

Sakai (2009) proposed the truncated cone and estimated its drag reduction performance using computational fluid dynamics method with Euler equations. In accordance with his results, while the magnitude of drag force is reduced with front face area of truncated cone model decreasing, the power gain is higher as the front face area increases. A quasi-steady state flowfield over truncated conical geometry is established with the higher repetitive frequency of pulse energy, typically higher than 50 kHz. In the quasi-steady state flowfield, recirculation zone composed of several vortices makes a virtual spike in front of the truncated cone body.

5-2. Experimental Conditions

Overall experimental apparatus is same with those used in Chapter 3. In this chapter, Nd:YVO_4 is used only to deposit the repetitive pulse energy. Comparing with laser optic system in chapter 3, pulse energy loss is enhanced up to about 10% as a result of concave lens replacing; about 24% before lens replacing.

Figures 5-2 and 5-3 show the schematic diagram of a truncated cone model used in experiments. First, the drag reduction performance with flat-faced truncated conical body is investigated, see Fig. 5-2. Base diameter of body, d, is 20 mm. The front face diameter is defined as d_f. The diameter ratio, d_f/d, is varied from 1.0 (cylinder model) to 0(cone model) with half angle of 15 degree. In order to improve the drag reduction performance, experimental studies are conducted on concave-faced truncated cone models with $d_f / d = 0.5$ as seen in Fig. 5-3. The radius curvatures of front face are R/d= 0.5 and 1.0, respectively. All of truncated cone models have same length, and location of depositing pulse energy is 2d ahead of the model.

The drag force is measured by using force balance system introduced in Chapter 3. The flowfiled over the model is visualized via schlieren system including two 300-mm-dia. concave mirrors and a circular knife edge. In a single run of the wind tunnel one hundred frames of schlieren images are captured into a high-speed framing camera (Shimadzu HPV-1) with a framing interval of 4 μs, 1/4 of which is an exposure period. To measure the time-dependent stagnation pressure, a piezoelectric pressure transducer (H112A21, PCB Inc., rise time of 1 μs, sensitivity of 7.015mV/Pa) is flush-mounted at head of the model. However, stagnation pressure is only estimated on 3-types (d_f / d=1.0, 0.75 and 0.5) flat-faced truncated con model, because diameter of pressure transduce is 5.56 mm.

Experimental conditions are shown in Table 5-1. Drag reduction performance with constant pulse energy is estimated as a function of laser frequency. In our laser optic system, laser frequency can be applied up to 50 kHz under allowable pulse energy, E, is 7.2 mJ. On the other hand, laser pulses up to 80 kHz is deposited with E=5.0 mJ.

5-3. Estimation of the Residence Time of Vortex Ring

For the absence of laser pulses, the shock layer over the truncated cone model is compared with a different d_f / d value in Fig. 5-4. Although all of shock layer have bow shock shape except for the case of the conical model($d_f / d = 0.0$), those shock stand-off distances are decreased with decreasing front face area; shock stand-off distance is 0.45 d for $d_f / d = 1.0$, 0.31d for $d_f / d = 0.75$ and 0.25d for $d_f / d = 0.5$. For the conical model in Fig. 5-4(d), it is found the attached oblique shock wave at M=1.94.

Sequential schlieren images related with $d_f/d = 0.75$ are shown at f=10 kHz and E=7.2mJ in Fig. 5-5. $\Delta t = 0$ μs indicates the laser pulse irradiation time. At $\Delta t = 48$ μs, laser-heated gas induced by laser irradiation at $\Delta t = 0$ μs is found. This heated gas with spherical shape is encountered with the shock layer at $\Delta t = 68$ μs. At this time, lens effect is occurred. Due to the interaction of laser-heated gas and shock layer, shock layer is temporally distorted and vortex ring is generated. Baroclinically generated vortex ring move downstream with expansion of ring diameter. The vortex ring arrive at front face of body after 176 μs. At this very moment, next laser-heated gas interacts with shock wave. At $\Delta t = 240$ μs, generated earlier vortex ring perfectly disappears and stagnation pressure returns to normal. From Fig. 5-5, the residence time of vortex ring can be roughly estimated 164 μs for truncated cone with $d_f / d = 0.75$.

For $d_f / d = 0.5$, the residence time of vortex ring becomes shorter as shown in Fig. 5-6. The lens effect is observed at $\Delta t = 72$ μs because the shock stand-off distance is shorter than $d_f / d = 0.75$. Therefore, the vortex ring nearly reaches into front face of body at $\Delta t = 128$ μs. Furthermore, it is found that the vortex ring disappears at $\Delta t = 176$ μs. In this case, effective residence time of vortex ring is approximately 100 μs. Only one vortex ring is observed for the truncated cone with $d_f / d = 0.5$, although two vortex rings can be observed between shock wave and model with $d_f/d = 0.75$ at f=10 kHz in Fig. 5-5. Consequently, the residence time of vortex ring becomes shorter with decreasing of d_f / d.

The effective residence time of vortex ring can be also found from stagnation pressure histories in Fig. 5-7. With $d_f / d = 1.0$, pulse-to-pulse interaction is significant at f=10 kHz. Hence,

stagnation pressure history shows the almost quasi-steady state behavior. However, stagnation pressure decrement caused by vortex ring can be found for $d_f / d = 0.75$. In the case of $d_f / d = 0.5$, stagnation pressure is almost recovered into the former state, and then affected by blast wave. Even if pulse-to-pulse interaction is somewhat occurred, the effect on stagnation pressure is very weak.

5-4. Drag Reduction Performance of Flat-Faced Truncated Cone Model

Figure 5-8 presents schlieren images with f=80 kHz and E=5.0 mJ. The apex angle of distorted shock layer becomes smaller with d_f/d increasing. In particular, shock layer shape of d_f / d=1.0 is similar to oblique shock. As the residence time of vortex rings is longer, the virtual spike composed of several vortices becomes more sharp. For the d_f / d=0.0, the baroclincal vortex ring is not observed because laser-heated gas interacts with attached oblique shock wave.

Figure 5-9 and 5-10 show the drag reduction performance of flat-faced truncated cone model as a function of f. When the pulse energy of 5.0 mJ is deposited, drag force almost linearly reduces with f, see Fig. 5-9(a). For d_f / d=1.0, $\Delta D/D_0$ is obtained up to 21%, and power gain is nearly constant value of about 6. Under the same condition, amount of drag reduction and power gain are decreased with decreasing of d_f / d. With E=5.0mJ, propulsion energy saving is not realized if d_f / d is smaller than 0.5. Same tendency can be found in Fig. 5-9(b) and 5-10(b). This result can be understood from the residence time variation of vortices as mentioned in previous section.

The drag coefficient, C_D, is plotted against f in Fig. 5-11. As repetitive laser frequency is increased, the drag coefficient is decreased. Corresponding to the results in Fig. 5-9 and 5-10, the drag coefficient is more effectively decreased with d_f / d increasing. Without energy depositions, drag coefficient of d_f / d=1.0 is 1.8. Although the drag coefficient of d_f / d=1.0 is decreased up to 1.46 with f=80 kHz and E=5. 0mJ, that is still higher than the base drag(=0.55) of conical model(d_f / d=0.0).

5-5. Drag Reduction Performance of Concave-Faced Truncated Cone Model

From the above results, it was concluded that drag reduction performance of truncated cone become poor since the effective residence time of vortices become shorter with d_f / d decreasing. Therefore, concave-faced truncated cone shape is considered to improve the drag reduction performance of truncated cone in this section. Truncated cone model with d_f / d=0.5 is used, and radius curvature (R/d) of concave face is varied from 0.5 to 1.0.

Figure 5-13 presents the effect of concave radius curvature on the drag reduction performance. It is interesting that $\Delta D/D_0$ with concave-faced truncated cone becomes higher comparing with flat-faced truncated cone. $\Delta D/D_0$ is increased by about 134% with R/d=1.0 for E=5.0mJ and f=80 kHz. As shown in Fig. 5-14, power gain is also slightly enhanced with concave-faced truncated cone. This is implies that concave-faced truncated cone is useful to improve the drag reduction performance. From these results, it is confirmed that drag coefficient of concave-faced truncated cone is slightly decreased. In the case of R/d=0.5, drag reduction performance is almost same with one of R/d=1.0. However, drag coefficient of R/d=0.5 becomes higher than that of R/d=1.0 because small radius curvature leads to increase of base drag force.

5-6. Summary

Although a blunt body shape brings the better drag reduction performance due to energy depositions, a truncated cone shape has considerable advantage to satisfy the mandatory conditions in actual application of energy deposition scheme; the magnitude of drag force should be lower than the base drag force of a sharp conical body and power gain of energy depositions should be higher than unity. From these demands, Drag reduction performance over truncated cone model was experimentally estimated.

In the experiments, a truncated cone model with half angle of 15 degree is used. The diameter ratio of flat-faced truncated cone is varied from 1.0 to 0.0. From the present results on flat-faced truncated cone, the effective residence time of vortices resulted by laser-heated gases interaction with shock wave plays an important role in drag reduction performance of truncated cone model. In order to improve the drag reduction performance of the truncated cones, the drag reduction performance of a concave-faced truncated cone model is evaluated. In the concave-faced truncated cone experiments, the radius curvature of concave face is varied from 0.5 to 1.0 with diameter ratio of 0.5. From the comparison with flat-faced truncated cone, the concave-faced truncated cone has more effective drag reduction performance.

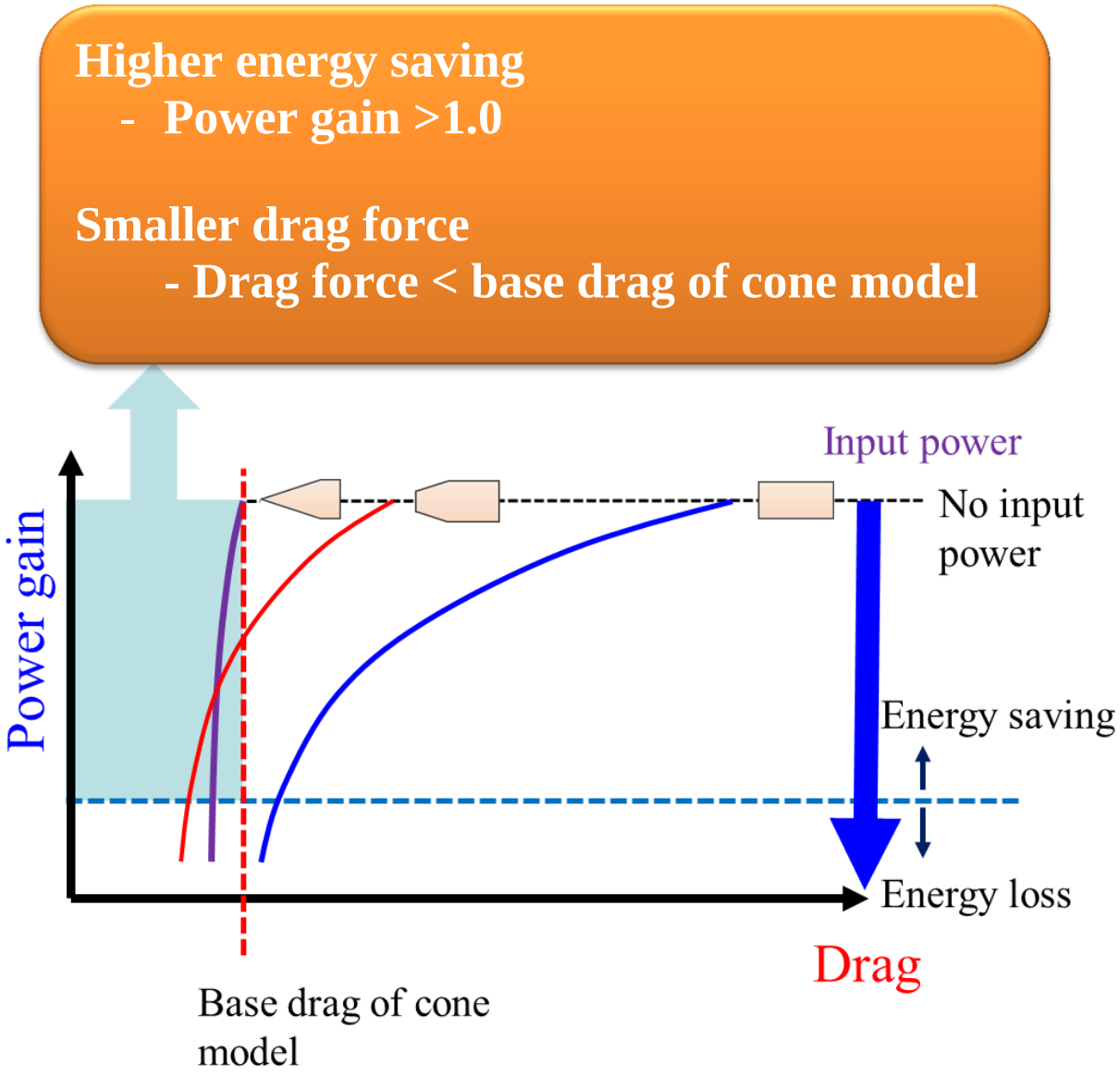

Figure 5 - 1 Concepts of truncated cone model for improving the drag reduction performance

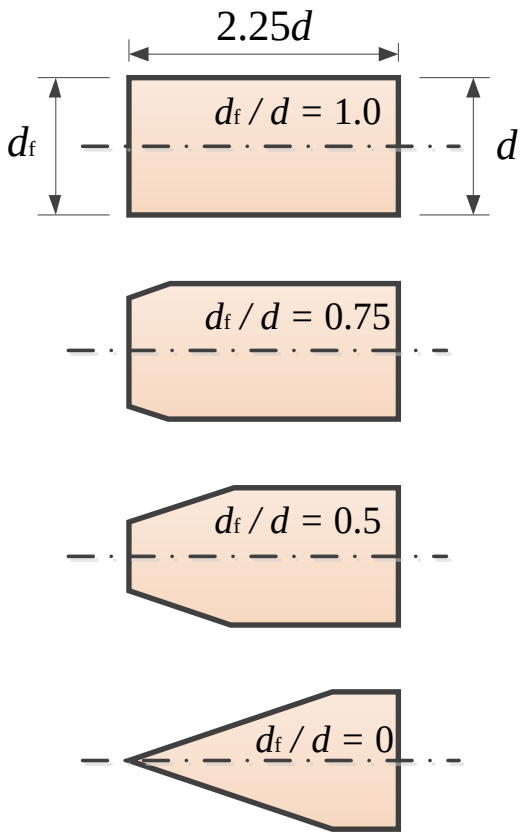

Figure 5 - 2 Schematic diagram of flat-faced truncated cone model

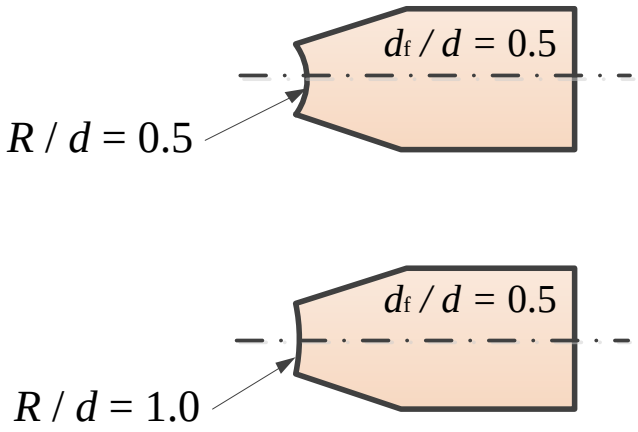

Figure 5 - 3 Schematic diagram of concave-faced truncated cone model with d_f/d = 0.5

Table 5 - 1 Experimental conditions for truncated cone

d_f/d	E [mJ]	f [kHz]	Shape of front face
1.0	5.0	10 ~ 80	Flat face
0.75	5.0	10 ~ 80	
0.75	7.2	10 ~ 50	
0.5	5.0	10 ~ 80	
0.5	7.2	10 ~ 50	
0	5.0	10 ~ 80	
0	7.2	10 ~ 50	
0.5	5.0	10 ~ 80	Concave face
0.5	7.2	10 ~ 50	
0.5	5.0	10 ~ 80	
0.5	7.2	10 ~ 50	

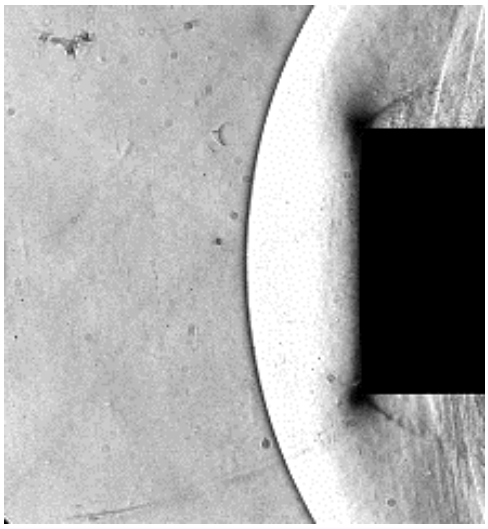

(a) d_f/d =1.0

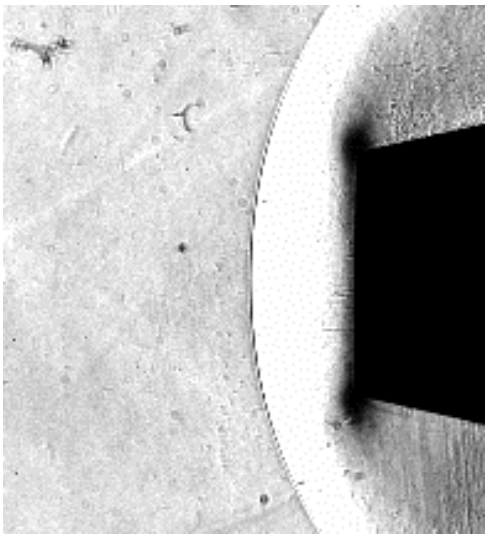

(b) d_f/d =0.75

(c) d_f/d =0.5

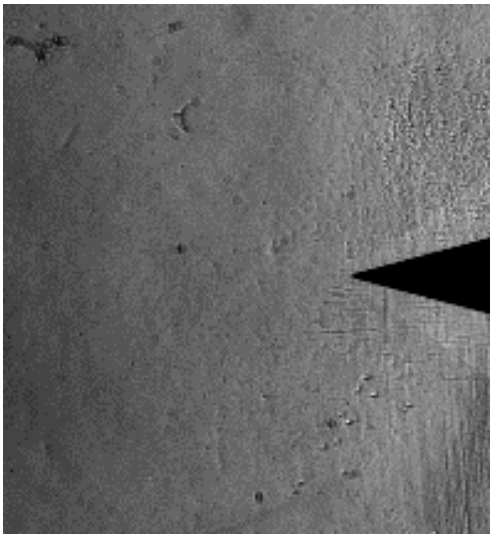

(d) d_f/d =0

Figure 5 - 4 Shock layer without laser pulses

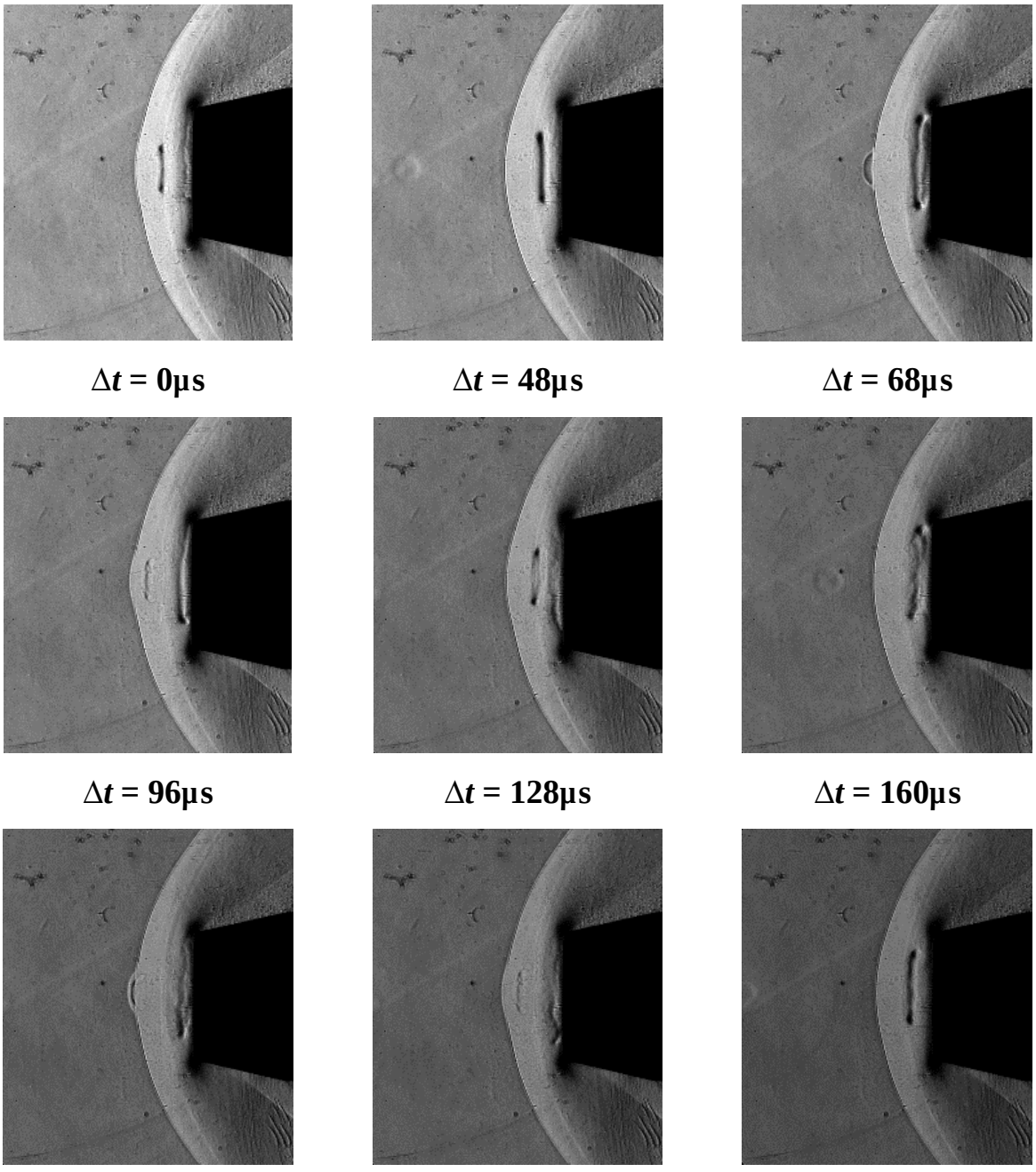

Figure 5 - 5 Sequential Schlieren images for d_f/d=0.75, E=7.2mJ/pulse, f=10kHz, framing interval=4μs, exposure=1.0μs

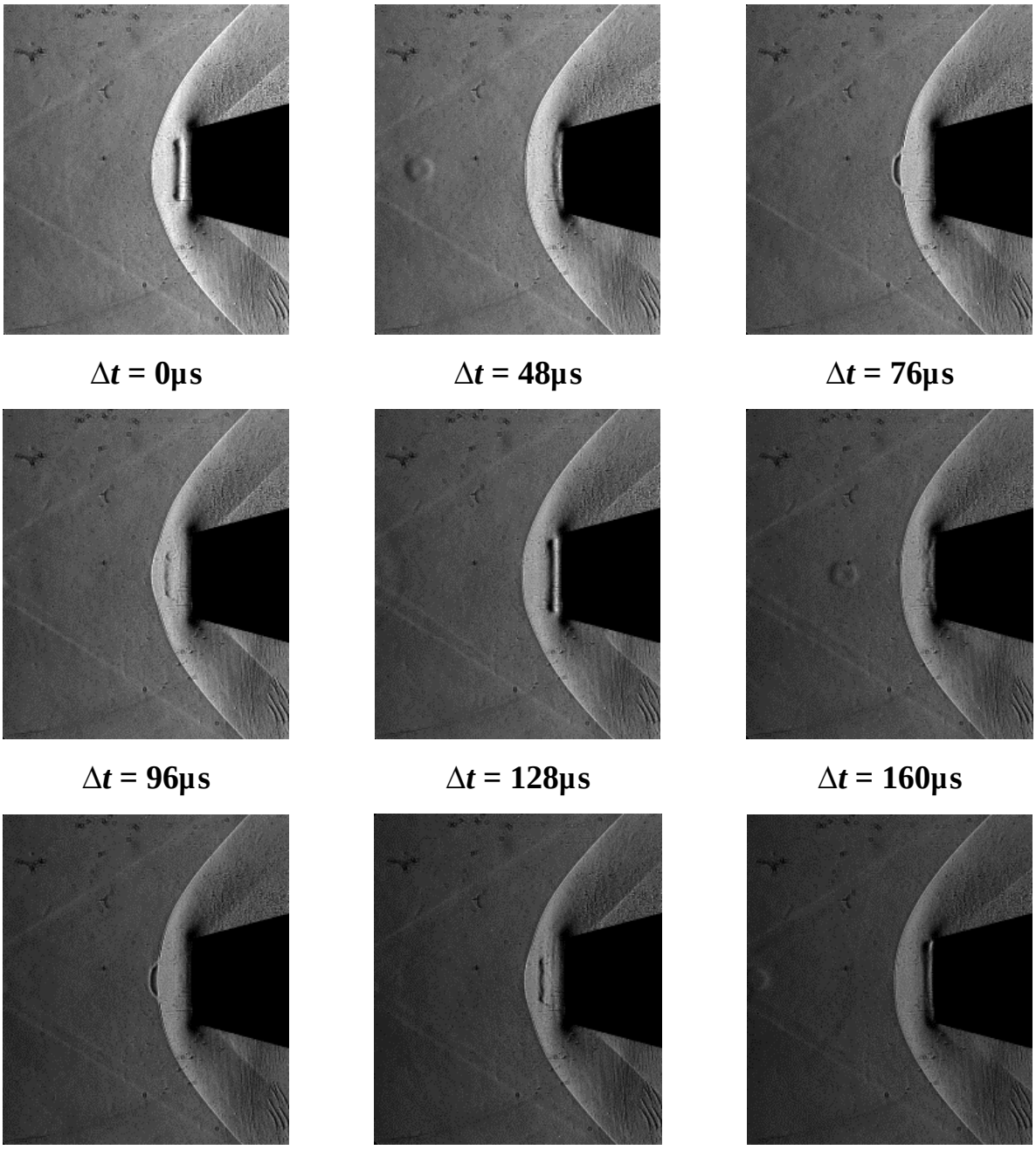

Figure 5 - 6 Sequential Schlieren images for d_f/d=0.50, E=7.2mJ/pulse, f=10kHz, framing interval=4μs, exposure=1.0μs

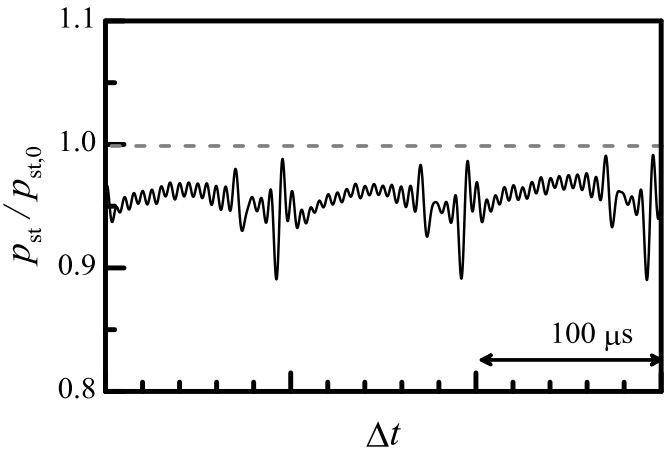

(a) d_f / d =1.0

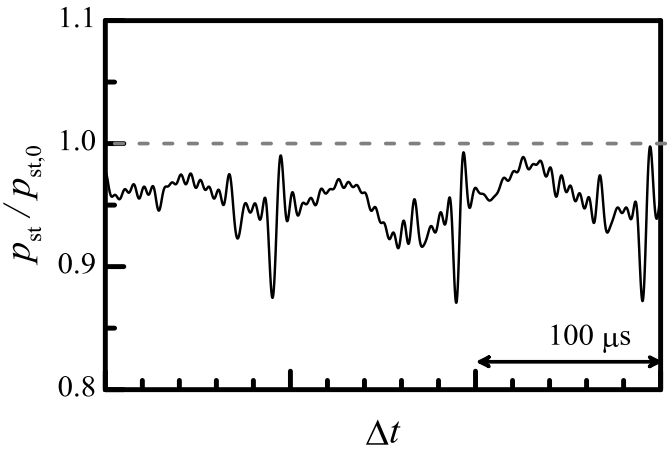

(b) d_f / d =0.75

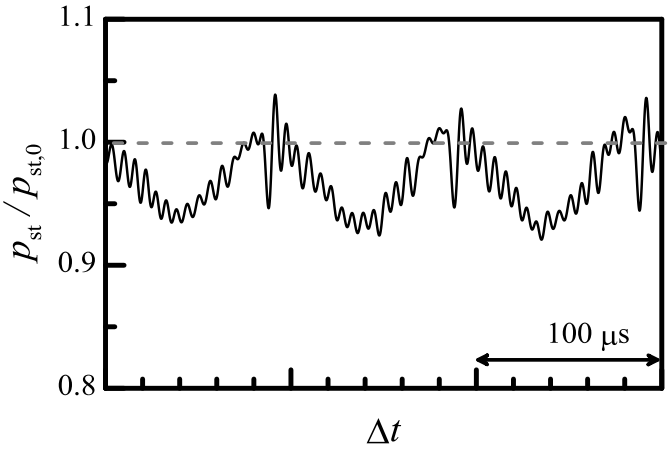

(c) d_f / d =0.5

Figure 5 - 7 Stagnation pressure histories, *f*=10kHz, *E*=5.0mJ

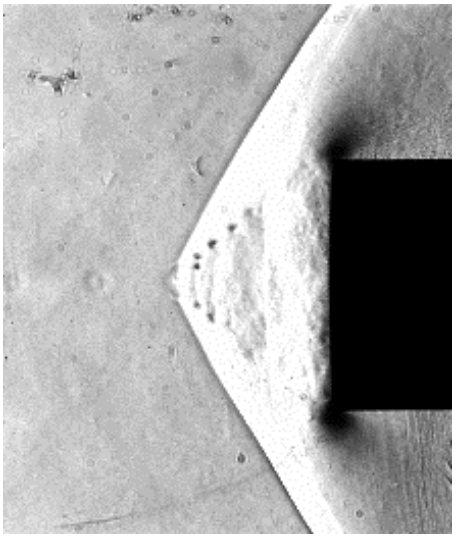

(a) d_f / d = 1.0

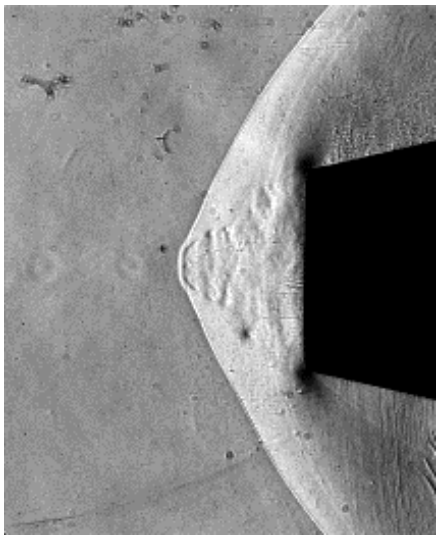

(b) d_f / d = 0.75

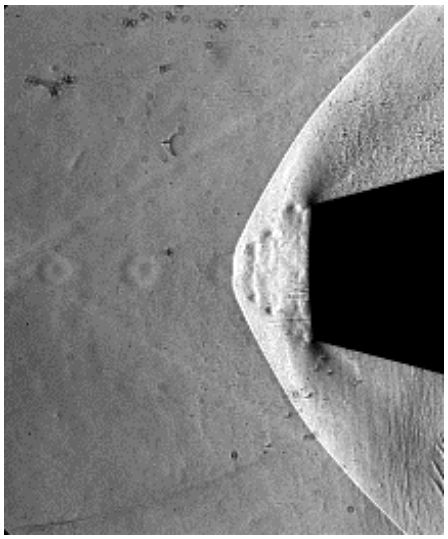

(c) d_f / d = 0.5

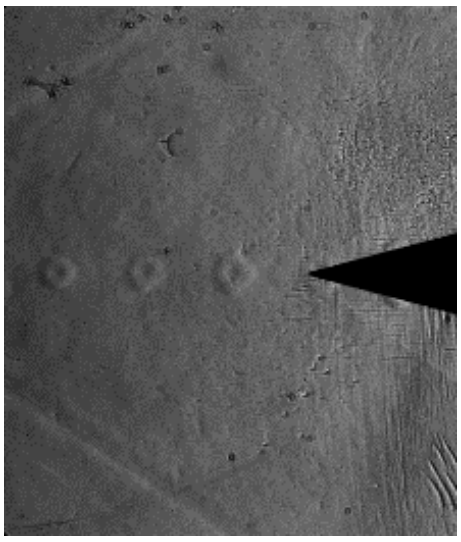

(d) d_f / d = 0.0

Figure 5 - 8 Instantaneous schlieren images at f= 80kHz, E=5.0mJ

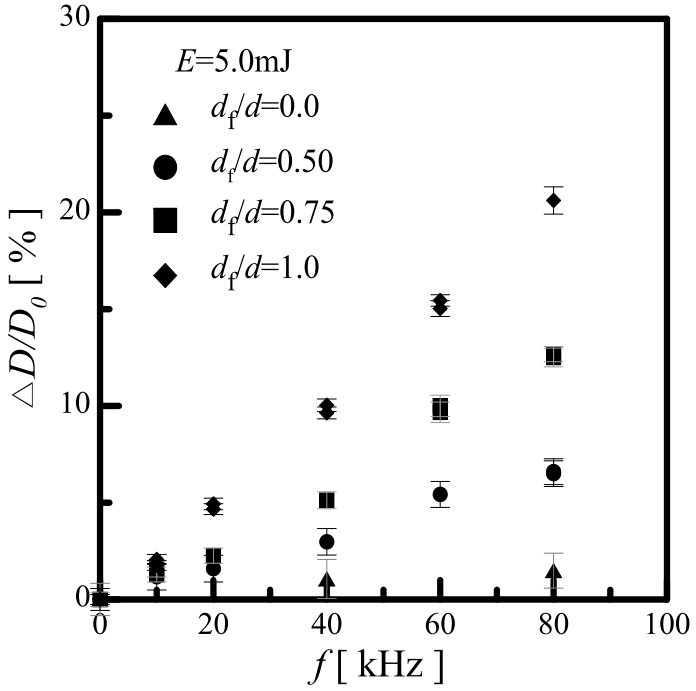

(a) *E*=5.0mJ/pulse

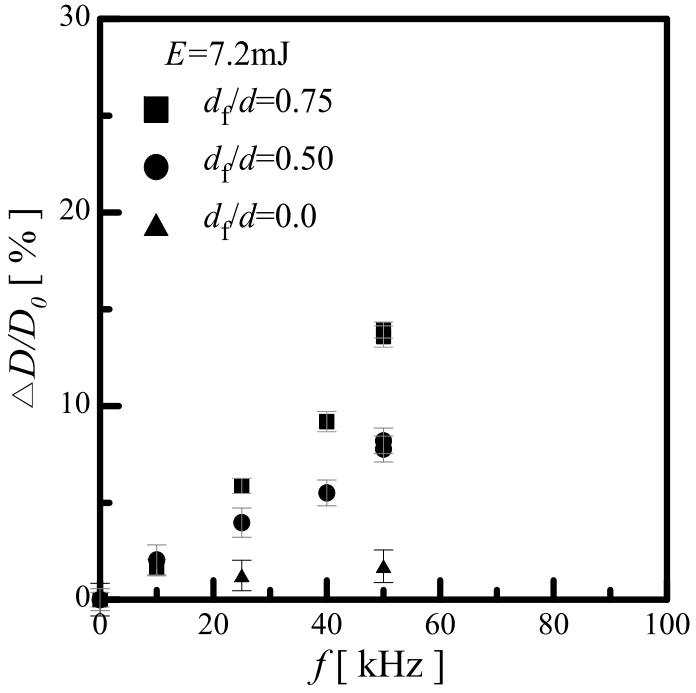

(b) *E*=7.2mJ/pulse

Figure 5 - 9 Drag reduction performance of flat-faced truncated cone model as a function of laser pulse frequency

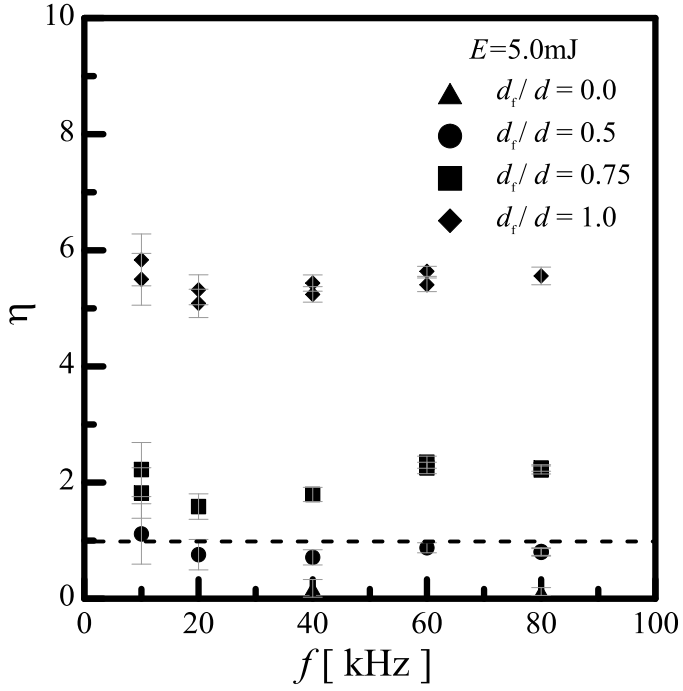

(a) *E*=5.0mJ/pulse

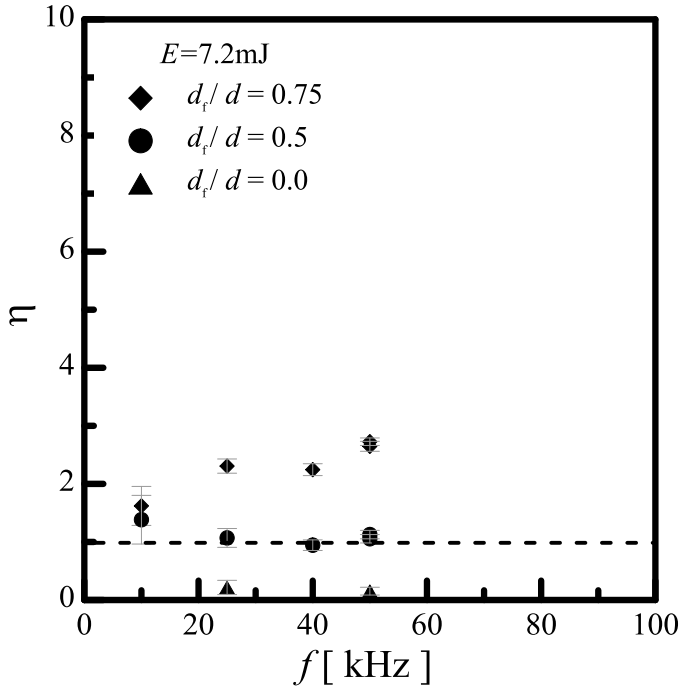

(b) *E*=7.2mJ/pulse

Figure 5 - 10 Power gain of flat-faced truncated cone model

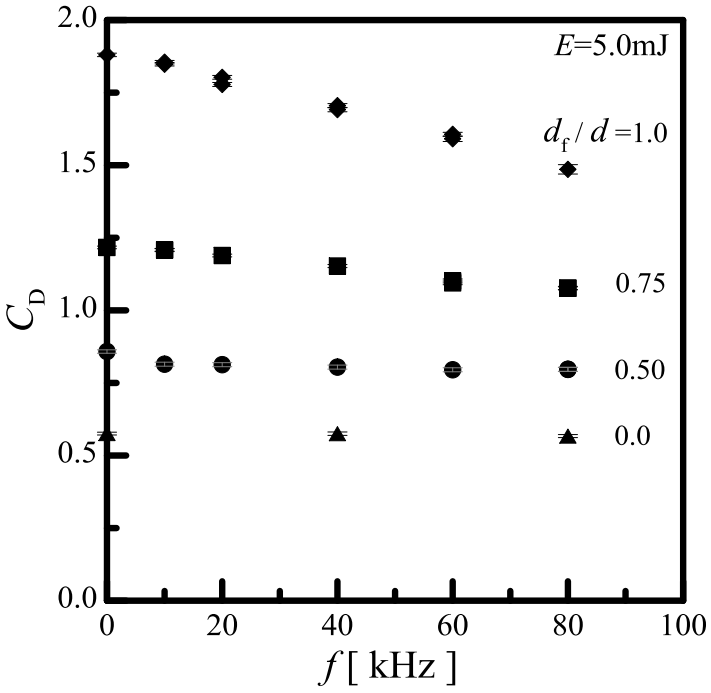

(a) *E*=5.0mJ/pulse

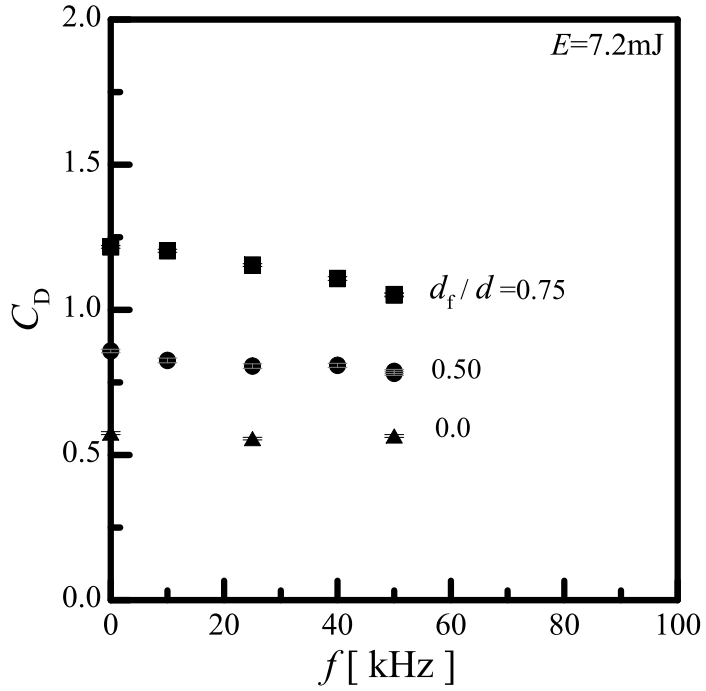

(b) *E*=7.2mJ/pulse

Figure 5 - 11 Variation of drag coefficient with d_f/d

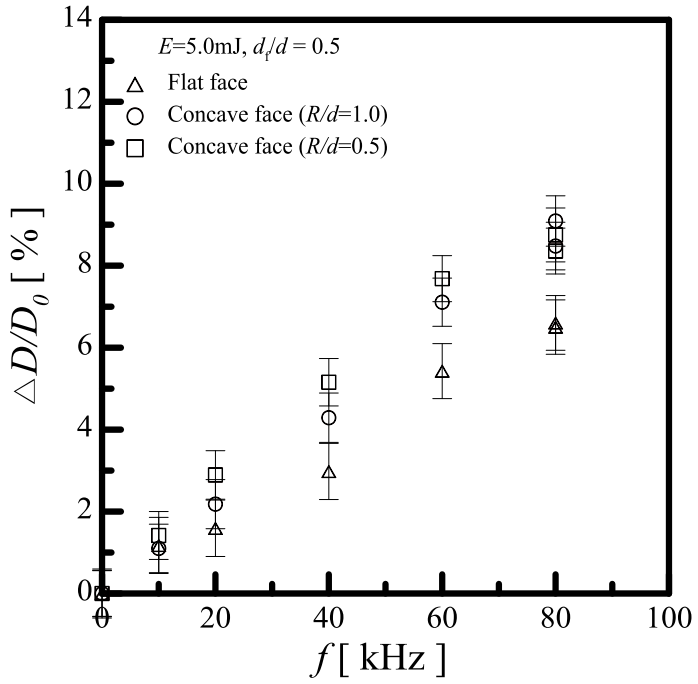

(a) *E*=5.0mJ/pulse

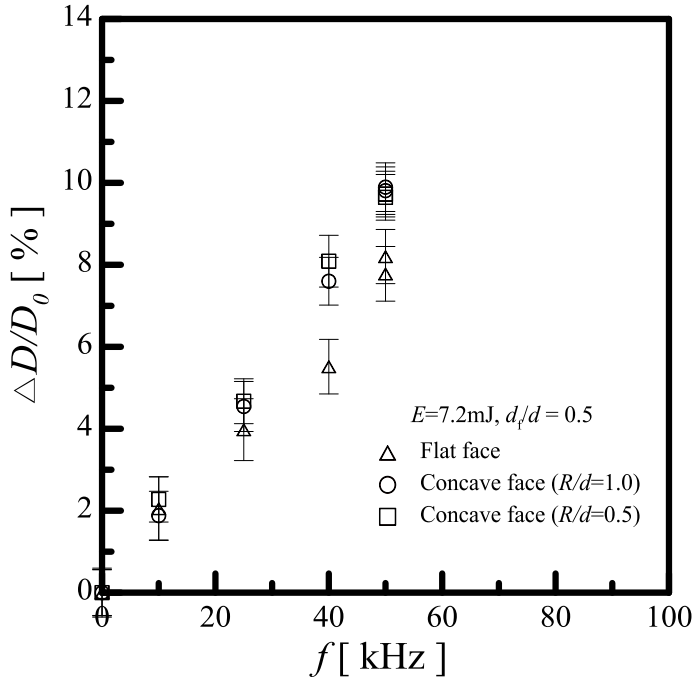

(b) *E*=7.2mJ/pulse

Figure 5 - 12 Drag reduction performance of concave-faced truncated cone model, d_f/d=0.50 with R/d=0.5

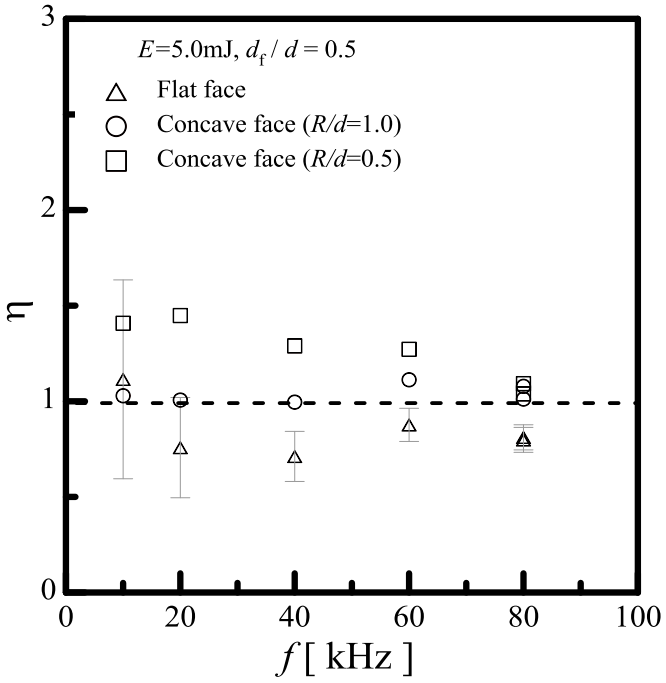

(a) *E*=5.0mJ/pulse

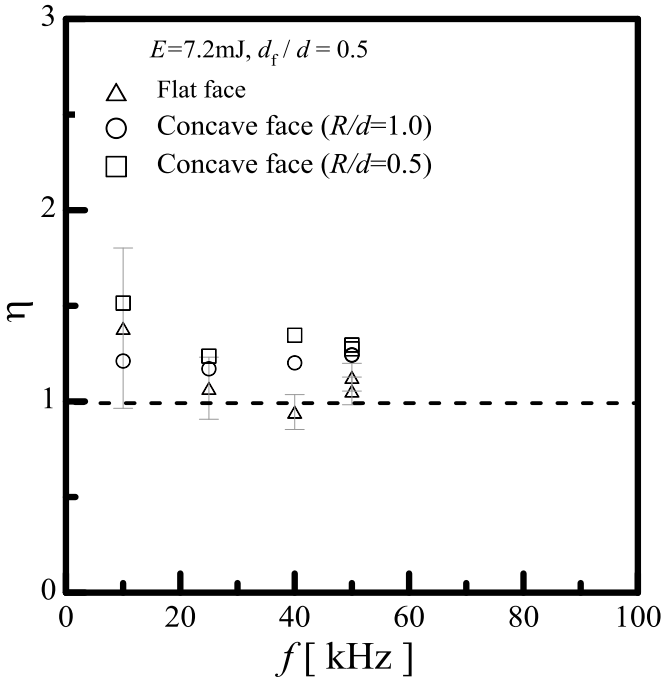

(b) *E*=7.2mJ/pulse

Figure 5 - 13 Power gain of concave-faced truncated cone model, d_f/d=0.50 with *R*/*d*=0.5

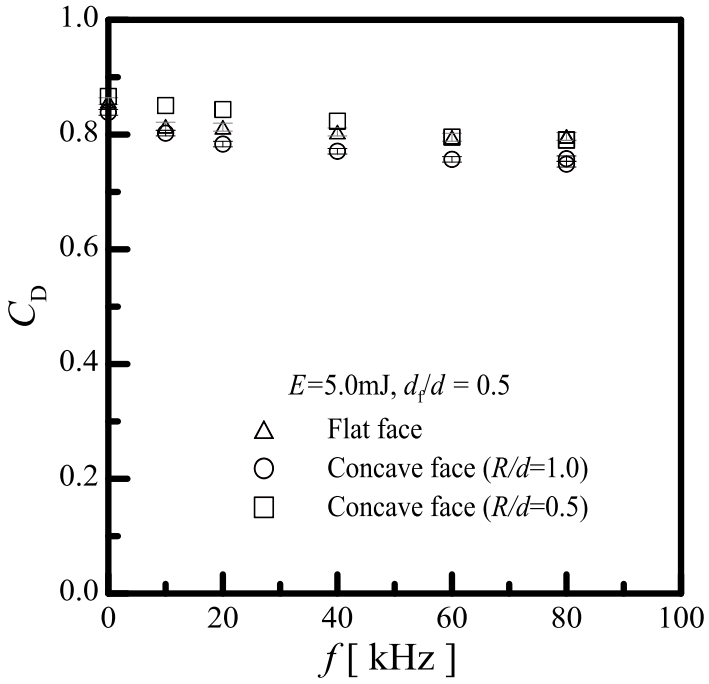

(a) *E*=5.0mJ/pulse

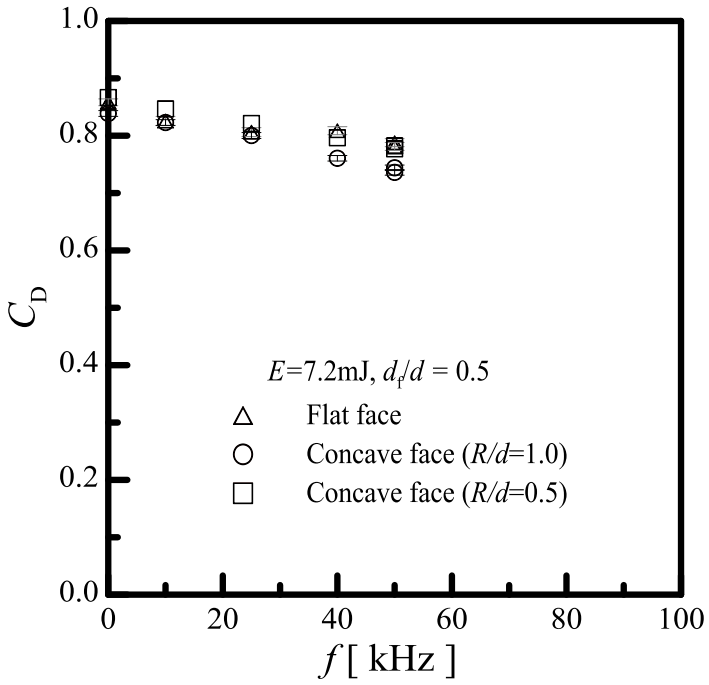

(b) *E*=7.2mJ/pulse

Figure 5 - 14 Drag coefficient of concave-faced truncated cone with d_f/d=0.5

Chapter 6. Concluding Remarks

6-1. Conclusions

In the present thesis, two issues, sonic boom and wave drag force, caused by shock wave which is generated at supersonic aircraft are discussed to improve the aerodynamic performance.

In chapter 2, the interaction phenomenon between weak shock wave and turbulent slit jet is investigated to sonic boom modulation related to turbulent atmosphere. When the sonic boom propagates through the atmosphere with turbulence, sonic boom signatures certainly modulates due to the turbulence. In order to demonstrate the sonic boom interaction with turbulent flowfield, it was investigated the interaction phenomenon between the laser –induced blast wave and slit jet flow. Remarkable conclusions are as follows,

- When the shock wave passes through the slit jet, several distortion types of the shock wave were observed.
- On average, the shock wave passing through the slit jet became slightly weaker. However, the standard deviation in peak overpressure is much larger.
- When the peak overpressure is increased, the shock front becomes locally flat; the local curvature is decreased.
- When the peak overpressure is decreased, the shock front has a hump; the local curvature greatly oscillates.
- These shock wave modulations through a region of non-uniform velocity should be better diagnosed with finer spatiotemporal resolutions, so that microscopic shock-vortex interactions can be related with the macroscopic shock wave behaviors which are observed in the present study.

As an advanced technology to reduce the wave drag, energy deposition scheme induced by high-repetitive laser pulses was mentioned in chapter 3. Steady-state drag reduction

performance was measured from a force balance over the back-pressure controlled piston using a load cell installed into in-draft supersonic wind tunnel of Mach number=1.94. Repetitive laser pulses of up to 50 kHz were used to deposit energy. Within the limited laser power capability, it has been experimentally demonstrated time-averaged drag reduction performance. Remarkable conclusions are as follows,

- With highly-repetitive laser pulses, significant bow shock moderation with baroclinic vortices is obtained.
- Baroclinically-generated vortices builds up the virtual spike ahead of the model, and the apex angle of distorted shock wave decreases with laser frequency increasing.
- Although pulse-to-pulse interaction becomes significant with laser frequency, drag reduction scales almost linearly with time-averaged stagnation pressure decreasing.
- Significant drag reduction performance has been obtained with high repetition frequencies of up to 60kHz.
- Amount of drag reduction is obtained up to 21%.
- Power gain of energy deposition can be given by a function of pulse energy.
- Power gain has a maximum value (=10) at optimum pulse energy of 8mJ, and threshold pulse energy for laser beam breakdown is around 4mJ.

Chapter 4 introduced the interaction motions among vortices by laser pulse energies. Series of vortex rings of a constant vorticity are experimentally generated due to baroclinic effects.

- At low f_0($\leq$5kHz,), interactions among the vortex rings are weak.
- In the intermediate repetition frequencies (10kHz$\leq f_0 \leq$30kHz), strong interactions among neighbor vortex rings are observed.
- The pitching interactions yield sub-modal line spectra in the stagnation pressure history.

- At f_0= 30 kHz, stronger interactions even lead to slip-through of vortex rings.
- Increasing f_0 over 40 kHz the flow field asymptotically approaches a steady-state structure to form a virtual spike composed of several vortex rings.

In chapter 5, experimental study on truncated cone model is conducted to realize the better wave drag reduction performance. Although a blunt body shape brings the better drag reduction performance, truncated cone shape has considerable advantage to satisfy the mandatory conditions in actual application of energy deposition scheme; the magnitude drag force should be smaller than base drag force of sharp cone body and the power gain of energy depositions should be higher than unity. From these demands, the drag reduction performance over a truncated cone model was experimentally estimated.

- Effective residence time of vortices resulted by laser-heated gases interaction with shock wave plays an important role in drag reduction performance of truncated cone model.
- In order to improve the drag reduction performance of truncated cone, a concave-faced truncated cone model is also suggested and its performance is estimated. In the concave-faced truncated cone experiments, the concave-faced truncated cone has more effective drag reduction performance compared to the flat-faced truncated cone.

6-2. Suggestion of Future Works

In this study, main efforts were focused on the wave drag reduction due to repetitive energy depositions to improve the supersonic aerodynamic performance. Based on the present experiment, with flat-faced blunt body, drag reduction is found to be linearly increased with laser frequency even if a pulse-to-pulse interaction is significant at higher frequency conditions. This linear characteristic should be explored through computational fluid dynamics(CFD).

Furthermore, it is suggested appreciable research for the ratio of lift and drag force. Although this study discussed only drag force issue to improve the aerodynamic performance, lift force enhancement is also an important subject. Therefore, the possibility of energy deposition scheme on lift improvement should be taken into account. It is considered that research on the ratio of lift and drag should be conducted to judge whether the energy deposition technique is a more powerful scheme to improve the aerodynamic performance

Bibliography

Adelgren, R. A., Yan, H., Elliott, G. S., Knight, D. D., Beutner ,T. J., and **Zheltovodov, A. A., 2005**, Control of Edney IV Interaction by Pulsed Laser Energy Deposition, *AIAA J.* Vol. 43(2), pp. 256-269.

Arnal, D., 1993, Boundary Layer Transition Prediction based on Linear Theory, AGARD Report 793.

Balla, V., Jagadeesh, G., and **Reddy, K. P. J., 2006**, Counterflow drag reduction by Supersonic Jet for a Blunt body in Hypersonic Flow, *Physics of Fluids*, Vol. 18, Paper No. 118104.

Bass, H. E., Layton, B. A., and **Bolen, L. N., 1987**, Propagation of medium strength shock waves through the atmosphere, *J. Acoustical Society of America*, Vol. 82(1), pp. 306-309.

Bass, H. E., Layton, B. A., Bolen, L. N., and **Raspet, R., 1987**, Propagation of Medium Strength Shock Waves through the Atmosphere, *J. Acoustical Society of America*, Vol. 82, pp. 306-310.

Bauer, A. B., and **Bagley, C. J**., 1970, Sonic Boom Modeling Investigation of Topographical and Atmospheric Effects, McDonnell-Douglas Corp., Report No. FAA-NO-70-10.

Beaulieu, W., Brovkin, V., Goldberg, I., Klimov, A., Kolesnichenko, Y., Krylov, A., Lashkov, V., Leonov, S., Mashek, I., Ryvkin, M., and **Serov, Y., 1998**, Microwave Plasma Influence on Aerodynamic Characteristics of Body in Airflow, Proc. of the 2nd Weakly Ionized Gases Workshop, pp. 24-25.

Ben-Dor, G., **2007**, Shock Wave Reflection Phenomena-second edition, Springer, chapter 3.

Biringen, S., Howard, J. E., and **Reichert, R. S., 2005**, Simulation of Sonic Boom Interaction with Shear Turbulence, *Mechanics Research Communications*, Vol. 32, pp. 604-609.

Bivolaru, D., and **Kuo, S. P., 2002**, Observation of Supersonic Shock Wave Mitigation by a Plasma Aero-Spike, *Physics of Plasma*, Vol. 9(3), pp. 721-723.

Bogdonoff, S. M., and **Vas, I. E., 1959,** Preliminary Investigation of Spiked Bodies at Hypersonic Speeds, *J. Aerospace Science*, Vol. 26(2), pp. 65-74.

Brieschenk, S., Hruschka, R., O'Byrne, S., and **Kleine, H., 2008**, High-Speed Time-Resolved Visualization of Laser-Induced Plasma Explosions, *Proc. of SPIE*, Vol. 7126, 71260N.

Brouillette, M., and **Hebert, C., 1997**, Propagation and Interaction of Shock-Generated Vortices, *Fluid Dyn. Res*., Vol. 21, pp. 159.

Bushnell, D. M., 1985, Turbulent Drag Reduction for External Flows, Aircraft Drag Prediction and Reduction, AGARD Report 723.

Castner, R., 2008, Analysis of Plume Effects on Sonic Boom Signature for Isolated Nozzle Configurations, 38th Fluid Dynamics Conference and Exhibit, Seattle, WT, AIAA Paper 2008-3729.

Chang, Y. K. and **Akili, A. D. V., 1995**, Dynamics of Vortex Rings in Crossflow, *Phys.Fluids*, Vol. 7, pp. 1583.

Chatterjee, A., 1999, Shock Wave Deformation in Shock-Vortex Interactions, *Shock Waves*, Vol. 9, pp. 95-105.

Chernyshev, S. L., Kiselev, A. P., and **Vorotnikov, P. P., 2008**, Sonic Boom Minimization and Atmospheric Effects, 46th AIAA Aerospace Sciences Meeting and Exhibit, Reno, Nv, AIAA Paper 2008-58.

Colella, p., and **Henderson, L. F., 1990**, The von Neumann Paradox for the Diffraction of Weak Shock Waves, *J. Fluid Mechanics*, Vol. 213, pp. 71-94.

Covert, E. E., James, C. R., Kimzey, W. F., Richey, G. K., and **Rooney, E. C., 1985**, Thrust and Drag : Its Prediction and Verification, *Progress in Astronautics and Aeronautics*, AIAA, New York, Chapter 4.

Crow. S. C., 1969, Distortion of sonic bangs by atmospheric turbulence, *J. Fluid Mechanics*, Vol. 37, pp. 529-563.

Ellzey, J. L., Henneke, M. R., Picone, J. M., and **Oran, E. S., 1995,** The Interaction of a Shock with a Vortex : Shock Distortion and the Production of Acoustic Waves, *Phys. Fluids*, Vol. 7(1), pp. 172-184.

Exton, R. J., Balla, R. J., Shirinzaded, B., Brauckmann, G. J., Herring, G. C., Kelliher, W. C., Fugitt, J., Lazard, C. J., and Khodataev, K. V., 2001, On-board Projection of a Microwave Plasma upstream of a Mach 6 Bow Shock, *Physics of Plasma*, Vol. 8, No. 11, pp. 5013-5017.

Glumac, N., Elliott, G., and **Boguszko, M., 2005**, Temporal and Spatial Evolution of Laser Spart in Air, *AIAA J*., Vol. 43, pp. 1984.

Guy, Y., McLaughlin T. E., and **Morrow, J. A., 2001**, Blunt Body Wave Reduction by means of a Standoff Spike, 39th AIAA Aerospace Science Meeting, Reno, NV.

Haglund, G. T., and **Kane, E. J., 1972**, Flight Test Measurements and Analysis of Sonic Boom Phenomena Near the Shock Wave Extremity, NASA CR-2167.

Hefner, J. N., Weinstein, L. M., and **Bushnell, D. M., 1980**, Large-Eddy Breakup Scheme for Turbulent Viscous Drag Reduction, Viscous Flow Drag Reduction, *Progress in Astronautics and Aeronautics*, Vol. 72, pp. 110-127.

Howe, D. C., and **Henne, P. A., 2006,** Improved Sonic Boom Scaling Algorithm, 44th AIAA Aerospace Sciences Meeting and Exhibit, Reno, NV, AIAA Paper 2006-27.

Hutt, C. R., and **Howe, A. J., 1989**, Forward Facing Spike Effects of Bodies of Different Cross Sections in Supersonic Flow, *Aeronautical Journal of the Royal Aeronautical Society*, Vol. 93(926), pp.229-234.

Imamura, O., Watanauki, T., Suzuki, K., and **Rathakrishnan, E., 2008**, Breathing Blunt Nose(BBN) for Drag Reduction at Hypersonic Speeds, *J. Visualization*, Vol. 11(4), pp. 280.

Ivanteeva, L. G., Kovalenko, V. V., Pavlyokov, E. V., Teperin, L. L., and **Racl, R. G., 2002**, Validation of Sonic Boom Propagation Codes using SR-71 Flight Test Data, *J. Acoustical Society of America*, Vol. 111(1), pp. 906-917.

Jones, E. P., Townsend, S. M., Guy, Y., and **McLaughlin, T. E., 2000**, Reduction of the Wave Drag of a Blunt Body by means of a Standoff Spike, AIAA Aerospace Science Meeting, Reno, NV.

Kandala, R., and **Candler, G. V., 2004**, Numerical studies of laser induced energy deposition for supersonic flow control, AIAA J. Vol. 42(11), pp. 2266–2275.

Knight, D., 2008, Survey of Aerodynamic Drag Reduction at High Speed by Energy Deposition, *J. Propulsion and Power*, Vol. 24(6), pp. 1153-1167.

Kolesnichenko, Y. F., Khmara, D. V., Brovkin, V. G., and **Afanas'ev, S. A., 2007**, Optimization of Laser-Pulse-Controlled MW Energy Deposition, 45th AIAA Aerospace Sciences Meeting and Exhibit, Reno. NV, AIAA Paper 2007-1228.

Lashkov, V. A., Mashek, I. C., Anisimov, Y. I., Ivanov, V. I., Kolesnichenko, Y, F., and **Azarova, O. A., 2007**, Gas-dynamic Effects around the Body under Energy Deposition in Supersonic Flow, 45th AIAA Aerospace Sciences Meeting and Exhibit, Reno. NV, AIAA Paper 2007-1231.

Leatherwood, J. D., and **Sullivan, B. M., 1994**, A laboratory study of subjective annoyance response to sonic booms, NASA TM 104150.

Lee, R. A., and **Downing, J. M., 1991**, Sonic Boom Produced by USAF and USN Aircraft: Measured Data, USAF AL-TR-1991-0099.

Lee, R. A., and **Downing. J. M., 1991**, Sonic boom produced by United States Air Force and United States Navy aircraft: measured data, AL-TR-1991-0099, Biodynamic Environment Branch, Biodynamics and Bioengineering Division, Armstrong Laboratory, Wright-Patterson Air Force Base, Ohio.

Lee, Y. S., and **Hamilton, M. F., 1995**, Time-domain Modeling of Pulsed Finite-Amplitude Sound Beams, *J. Acoustical Society of America*, Vol. 97(2), pp. 906-917.

Leweke, T., and **Williamson, C. H. K., 1998**, Cooperative Elliptic Instability of a Vortex Pair, *J. Fluid Mechanics*, Vol. 360, pp. 85.

Liang, S. M., Hsu, J. L., and **Wang, J. S., 2001**, Numerical Study of Cylindrical Blast-Wave Propagation and Reflection, **AIAA J**., Vol. 39(6), pp. 1152-1158.

Liow, Y. S. K., Thompson, M. C., and **Hourigan, K., 2005**, Sound Generated by a Pair of Axisymmetric Coaxial Vortex Rings, *AIAA J.*, Vol. 43(2), pp. 326.

Lipkens, B., 2002, Model Experiment to Study Sonic Boom Propagation through Turbulence. Part III: Validation of Sonic Boom Propagation Models, *J. Acoustical Society of America*, Vol. 111(1), pp. 509-519.

Lipkens, B., and **Blackstock, D. T., 1998**, Model Experiments to Study Sonic Boom Propagation through Turbulence, Part 1 : General Results, *J. Acoustical Society of America*, Vol. 103(1), pp. 148-158.

Loftin, L. K. Jr., 2006, Quest for Performance : The Evolution of Modern Aircraft, NASA SP-468.

Maglieri, D. J., 1967, Sonic boom flight research-some effects of airplane operations and the atmosphere on sonic boom signatures, Sonic Boom Research, NASA SP-147.

Maglieri, D. J., Huckel, V., Henderson, H. R., and **McLeod, N. J., 1969**, Variability in sonic-boom signatures measured along an 8000-foot linear array, NASA TN D-5040.

Maglieri, D. J., Sothcott, V. E., and **Keefer, T. N. Jr., 1992**, A Summary of XB-70 Sonic Boom Signature Data, NASA CR-189630.

Maull, D. J., 1960, Hypersonic Flow over Axially Symmetric Spiked Bodies, *J. Fluid Mechanics*, Vol. 8(4), pp. 584-592.

May, D. N., 1971, Startle due to sonic booms heard outdoors as functions of overpressure and rise time, *J. Sound vibration*, Vol. 18, pp. 114-145.

McCurdy, D. A., 1994, Subjective responses to sonic booms having different shapes, rise times and duration, NASA TM 109090.

Meyer, R., Nelson, H. F., and **Riggins, D. W., 2001**, Hypersonic Drag and Heat-Transfer Reduction using a Forward Facing Jet, *Journal of Aircraft*, Vol. 38(4), pp. 680-686.

Minota, T., 1993, Interaction of a Shock Wave with a High-Speed Vortex Ring, *Fluid Dynamics Research*, Vol. 12, pp. 335-342.

Minota, T., Kambe, T., and **Murakami, T., 1988**, Acoustic Emission from Interaction of a Vortex Ring with a Sphere, *Fluid Dynamics Research*, Vol. 3, pp. 357-362.

Mitchell, B. E, Lele, S. K., and **Moin, P., 1995**, Direct Computation of the Sound from a Compressible Co-Rotating Vortex Pair, *J. Fluid Mechanics*, Vol. 285, pp. 181.

Niedzwiecki, A., and **Ribner, H. S., 1978**, Subjective Loudness of Minimized Sonic Boom Waveforms, *J. Acoustical Society of America*, Vol. 64, pp. 1617-1621.

Ogino, Y., 2009, Numerical Study of Laser-Generated Unsteady Plasma in Propulsion and Flow Control Technique, Ph. D thesis, Tohoku Univ.

Ogino, Y., Ohishi, N., Taguchi, S., and **Sawada, K., 2009,** Baroclinic Vortex Influence on Wave Drag Reduction induced by Pulse Energy Deposition, *Physics of Fluids*, Vol. 21, Paper No. 066102.

Onyeonwu, R. O., 1975, Sonic Boom Signatures and Ray Focusing in General Manoeuvres:I. Analytical Foundations and Computer Formulation, *J. Sound Vibration*, Vol. 42(1), pp. 85-102.

Pierce, A. D., 1968, Spikes on Sonic Boom Pressure Waveforms, *J. Acoustical Society of America*, Vol. 44, pp. 1052-1061.

Pierce, A. D., and **Maglieri, D. J., 1972**, Effects of Atmospheric Irregularities on Sonic-Boom Propagation, *J. Acoustical Society of America*, Vol. 51(2), pp. 702-721.

Plotkin, K. J., and **George, A. R., 1972**, Propagation of weak shock waves through turbulence, *J. Fluid Mechanics*, Vol. 54, pp. 449-467.

Plotkin, K. J., and **Sizov, N. V., 2008,** Examination of Sonic Boom Minimization Experienced Indoors, 46th AIAA Aerospace Sciences Meeting and Exhibit, Reno, NV, AIAA Paper 2008-57.

Ramanah, D., Raghunath, S., Mee, D. J., Rosgen, T., and **Jacobs, P. A., 2007**, Background Oriented Schlieren for Flow Visualization in Hypersonic Impulse Facilities, *Shock Waves*, Vol. 17, pp. 65-70.

Reynolds, W. C., Parekh, D. E., Juvet, P. J. D., and **Lee, M. J. D., 2003**, Bifurcating and Blooming Jets, *Annu. Rev. Fluid Mech.*, Vol. 35, pp. 295.

Ribner, H. S., 1985, Cylindrical Sound Wave Generated by Shock-Vortex Interaction, *AIAA J.*, Vol. 23(11), pp. 1708-1715.

Ribner, H. S., Morris, P. J., and **Chu, W. H., 1973**, Laboratory Simulation of Development of Superbooms by Atmospheric Turbulence, *J. Acoustical Society of America*, Vol. 53, pp. 926-928.

Ribner, H. S., Morris, P. J., and **Chu, W. H., 1973**, Laboratory Simulation of Development of Superbooms by Atmospheric Turbulence, *J. Acoustical Society of America*, Vol. 53, pp. 926-928.

Rice, C. G., 1996, Human Response Effects of Impulse Noise, *J. Sound Vibration*, Vol. 190(3), pp. 525-543.

Rice, C. G., and **Coles, R. R. A., 1968**, Auditory hazard from sonic booms, *International Audiology*, Vol. 7(2), pp. 211-217.

Rice, C. G., and **May D. N., 1996**, Startle due to sonic boom-statement of the problem, *Institute of Sound and Vibration*, Research Technical Report 25.

Richard, H., and **Raffel, M., 2001**, Principle and Applications of the Background Oriented Schlieren(BOS) Method, *Measurement Science and Technology*, Vol. 12, pp. 1576-1585.

Riggins, D., Nelson, H. F., and **Johnson, E., 1999**, Blunt-Body Wave Drag Reduction Using Focused Energy Deposition, *AIAA J.*, Vol. 37(4), pp.460-467.

Rylander, R., 1972, Sonic boom exposure effects, *J. Sound Vibration*, Vol. 5, pp. 285-289.

Sakai, T., 2009, Supersonic Drag Performance of Truncated Cones with Repetitive Energy Depositions, *Intl. J. Aerospace Innovations*, Vol. 1(1), pp. 31-43.

Sakai, T., Sekiya Y., Mori, K., and **Sasoh, A., 2008**, Interaction Between Laser-Induced Plasma and Shock Wave Over a Blunt Body in a supersonic flow, *Proc. IMechE J. Aerospace Engineering*, Vol. 222, *Part G*, pp. 605-617.

Sakai, Y., Watanabe, T., Kamohara, S., Kushida, T., and **Nakamura, I., 2001**, Simultaneous Measurements of Concentration and Velocity in a CO2 Jet Issuing into a Grid Turbulence by Two-Sensor Hot-Wire Probe, *Intl. J. Heat and Fluid Flow*, Vol. 22, pp. 227-236.

Salikuddin, M., Tam, C. K. W., and **Burrin, R. H., 1988**, An Experimental and Theoretical Investigation of the Propagation of Sound Waves through a Turbulent Boundary Layer, *J. Sound Vibration*, Vol. 127(1), pp. 91-121.

Salikuddin, M., Tam, C. K., and **Burrin, R. H., 1988**, An Experimental and Theoretical Investigation of the Propagation of Sound Waves through a Turbulent Boundary Layer, *J. Sound Vibration*, Vol. 127(1), pp. 91-121.

Sang, J., Hayers, J., and **Menart, J., 2001**, Hypersonic Flow over a Blunt Body with Plasma Injection, AIAA Paper 2001-0344.

Sasoh, A., Ohtani, T., and **Mori, K., 2006,** Pressure Effect in a Shock-Wave-Plasma Interaction Induced by a Focused Laser Pulse, *Phys. Review Letters*, Vol. 97, 205004.

Sasoh, A., Sekiya, Y., Sakai, T., Kim, J.-H., and **Matsuda, A., 2010**, Wave Drag Reduction over a Blunt Nose with Repetitive Laser Energy Depositions, *AIAA J.* Vol. 48(12) , pp. 2811-2817.

Schulein, E., Zheltovodov, A. A., Pimonov, E. A., and **Loginov, M. S., 2009**, Study of the Bow Shock Interaction with Laser-Pulse-Heated Air Bubbles, 39th AIAA Fluid Dynamics Conference, San Antonio, TX, AIAA Paper 2009-3568.

Taguchi, S., Ohnishi N., Furudate, M., and **Sawada, K., 2007**, Numerical Analysis of Drag Reduction for Supersonic Blunt Body by Pulse Energy Deposition, AIAA Paper 2007-1235.

Takayama, K., Sasoh, A., Onodera, O., Kanako, R., and **Matsui, Y., 1995,** Experimental Investigation on Tunnel Sonic Boom, *Shock Waves*, Vol. 5, pp. 127-138.

Tang, S. K., and **Ko, N. W. M., 1995**, On Sound Generated from the Interaction of Two Inviscid Coaxial Vortex Rings Moving in the Same Direction, *J. Sound Vibration*, Vol. 187(2), pp. 287.

Tanner, M., 1975, Reduction of Base Drag," *Progress of Aerospace Science*, Vol. 16(4), pp. 369-384.

Tret'yakov, P. K., Garanin, A. F., Grachev, G. N., Krainev, V. L., Ponomarenko, A. G., Tishchenko, V. N., and Yakovlev, V. I., 1996, Control of Supersonic Flow around Bodies by Means of High-Power Recurrent Optical Breakdown, *Physics-Doklady*, Vol. 41(1), pp. 566-567.

Tubb, P. E., 1975, Measured Effects of Turbulence on the Rise Time of a Weak Shock," AIAA paper 75-543.

Vashishtha, A. and **Rathakrishnan, E., 2009**, Breathing Blunt-Nose Concept for Drag Reduction in Supersonic Flow, *Proc. IMechE J. Aerospace Engineering*, Vol. 223, Part G, pp. 31-38.

Walsh, M. J., 1980, Drag Characteristics of V-Groove and Transverse Curvature Riblets, Viscous Flow Drag Reduction, *Progress in Astronautics and Aeronautics*, Vol. 72, pp. 168-184.

Yamada, H., and **Matsui, T., 1979**, Mutual Slip-Through of a Pair of Vortex Rings, *Physics of Fluids*, Vol. 22, pp. 1245.

Yamauchi, M., Fujii, K., Tamura, Y., and **Higashino, F., 1993**, Numerical Investigation of Supersonic Flows around a Spiked Blunt-Body, 31th AIAA Aerospace Science Meeting, Reno, NV.

Zaidi, S. H., Shneider, M. N., and Miles, **R. B., 2004**, Shock-Wave Mitigation through Off-Body Pulsed Energy Deposition, *AIAA J.*, Vol. 42(2), pp. 326-331.

Zepler, E. E., and **Harel, J. R. P., 1965**, The loudness of sonic booms and other impulse sounds, *J. Sound Vibration*, Vol. 2, pp. 249-256.

Zheltovodov, A. A., Pimonov, E. A., and **Knight, D. D., 2007**, Energy Deposition Influence on Supersonic Flow Over Axisymmetric Bodies, AIAA Paper 2007-1230.

Acknowledgement

I would like to my hearty thanks to my supervisor, Professor Akihiro Sasoh for guidance, advice and encouragement to accomplish the present work over the years. He originated this research project and shared his insight and experience on this work. I also sincerely thank the committee members of this manuscript, Professor Yoshiaki Nakamura, Professor Yasuhiko Sakai, and Professor Takeharu Sakai for taking valuable time out their busy schedules to provide advice and suggestions to this work.

I want to express my special thanks to Associate Professor Atsushi Matsuda for encouragement and many technical advices. I am also would like to thank A. Saito, N. Shiraki and K. Kumazawa**,** Technical Division, Nagoya University for their valuable technical assistances.

I also wish to deeply express my gratitude to Professor Heuy-Dong Kim for recommending to study in Prof. Sasoh's laboratory and his guidance and encouragement. His rigor and standard towards studying science provides the perspectives and inspirations which I needed much as a student.

I am very grateful to all members of Ionized Gas Dynamics Laboratory for many helpful discussions and advices regarding the life in Japan. In addition, special thanks to Mr. D. Takagi, Mr. N. Ogita, and Mr. M. Yonemoto for their assistance, cooperation and kindness over the course of my graduate study. I would like to thank my friends, Dr. Yong-Hun. Kwon, Dr. Young-Jun Jang, Dr. Sang-Ho Kim, Mr. Chae-Min Lim, Mr. Young-Kun Lee, Mr. Jin-Kyung Kim, Mr. Jong-Hun Kim and Mr. Suk-Hwan Park for their encouragement.

Finally, I cannot express enough appreciation to my family for their endless affections and supports. Most of all, I have to express my deepest gratitude to my wife, Sung-Mi Kwon. Without the support and willingness to assume more than her share of responsibilities in the family, the work would not have been possible. I dedicate this work to the memory of my late father who has always been my reliable supporter and will be in my heart forever.

This study was partially supported by Research Fellowships program of the Japan Society for the Promotion of Science(JSPS) for Young Scientist.

Jae-Hyung KIM